FABRICATION OF CLOG-FREE MICROFLUIDIC CELL ISOLATION AND SOLID-STATE LIGHT EMITTING DEVICES FOR BIOMEDICAL APPLICATIONS

A Dissertation

presented to

the Faculty of the Graduate School

at the University of Missouri-Columbia

In Partial Fulfillment

of the Requirements for the Degree

Doctor of Philosophy

---

by

DILIP VENUGOPAL

Dr. Peifen Zhu, Dissertation Supervisor

MAY 2023

The undersigned, appointed by the dean of the Graduate School, have examined the Dissertation entitled

Fabrication of Clog-free Microfluidic Cell Isolation and
Solid-State Light-Emitting Devices for Biomedical Applications

presented by Dilip Venugopal,

a candidate for the degree of PhD,

and hereby certify that, in their opinion, it is worthy of acceptance.

Professor Peifen Zhu

Professor Syed Islam

Professor Ekincan Ufuktepe

Professor Walter Gassmann

ACKNOWLEDGEMENTS

I would like to express my gratitude to dissertation advisor, Assistant Professor Peifen Zhu for her patience and faith in me. Thank you, Dr. Zhu, for your excellent guidance and motivation to support me during my graduate studies and making it possible for the completion of this study. Because of her, I had the opportunity to learn and gain the skills essential for me to be a good researcher during my time as a graduate student and I am honored to carry these with me to my future career.

Equally, I am thankful to all my dissertation committee members, Professor Syed Islam, Assistant Teaching Professor Ekincan Ufuktepe and Professor Walter Gassmann, for their brilliant comments and suggestions to make my dissertation work more organized and impactful while also making my defense to be an enjoyable and treasured moment for me.

I am extremely thankful to my beloved parents and my sister for their constant love and support. I would like to thank my friends, lab mates, and colleagues for a cherished time spent together in the lab, and in social settings.

TABLE OF CONTENTS

LIST OF ILLUSTRATIONS

LIST OF TABLES

FABRICATION OF CLOG-FREE MICROFLUIDIC CELL ISOLATION AND SOLID-STATE LIGHT EMITTING DEVICES FOR BIOMEDICAL APPLICATIONS

Dilip Venugopal

Dr. Peifen Zhu, Dissertation Supervisor

ABSTRACT

Over the past few decades, research and development on microfluidic devices, also referred to as lab-on-a-chip systems or microfluidic total analysis systems (TAS), have advanced quickly. There aren't many commercial success stories for microfluidic devices, despite the many advantages they offer, including improved analytical performance, decreased sample and reagent usage in the biomedical disciplines. From liquid biopsies, microfluidics has been used to filter out rare tumor cells from blood. Low flow rates and device clogs brought on by a single fluidic path function severely restrict processing. A novel technique was created employing multifunctional hybrid microposts with various features has effectively ensured high effective separation of rare cells from biological fluids.

Furthermore, Solid-State perovskite material is synthesized, fabricated in 3D printed layers, and characterized for the need to be incorporated into fluorescence imaging of biological cells. Since effective imaging techniques are required to image the cells in a PDMS-based microfluidic device, the emission of the perovskite material shows positive signs as a fluorescent light source for identification of cells based on their emission of light.

Fabrication of Clog-free Microfluidic Cell Isolation and Solid-State Light emitting devices for Biomedical Applications

Chapter 1 Introduction

1.1 Microfluidics

1.1.1 Introduction to Microfluidics

During the past few decades, much time, money, publications [1], and effort have been put into the field of miniaturizing instruments for biological and chemical analysis Figure 1-1. These efforts have made it possible to miniaturize a variety of systems, including mechanical, fluidic, electromechanical, and thermal ones, sometimes to submicron dimensions. Micro-electro-mechanical systems are referred to as MEMS. Other names associated with it include microsystems technology (MST) and micromachines.

A broad range of microfabrication designs, techniques, and mechanisms that involve the tiny realization of moving mechanical parts are together referred to as MEMS. Microfluidic technology (part of MEMS) has been developed from a molecular analysis project intended to improve separation performance through reduced dimensions into a broad sector influencing an ever-growing spectrum of disciplines. In fields where its intrinsic benefits outweigh conventional approaches, including chemistry, biology,

genomics, proteomics, pharmaceuticals, and biodefense, microfluidic techniques are used.

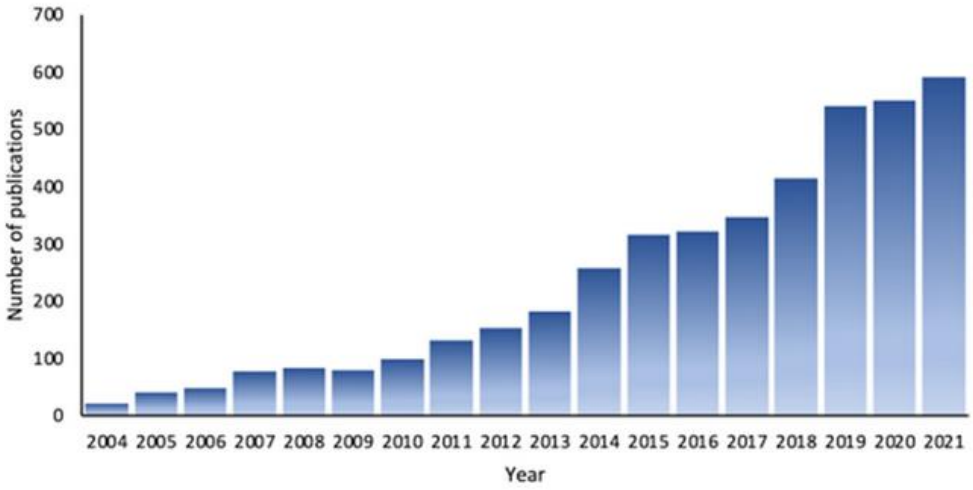

Figure 1-1. Microfluidic Publications by year rapidly increasing in over the last two decades.

From a biological perspective, microfluidics seems particularly pertinent given that most biological activities at some point involve small-scale fluidic movement. Examples include the movement of molecules across cellular membranes, the diffusion of oxygen through the lungs, and the flow of blood via minute artery networks. Moreover, microfluidics can offer more naturalistic in vitro settings for selected small-scale biological species. To give a visualization of the scale microfluidics deals in, the Figure 1-2 shows the scales [2] of many biological structures, and MEMS technology used in the field of microfluidics.

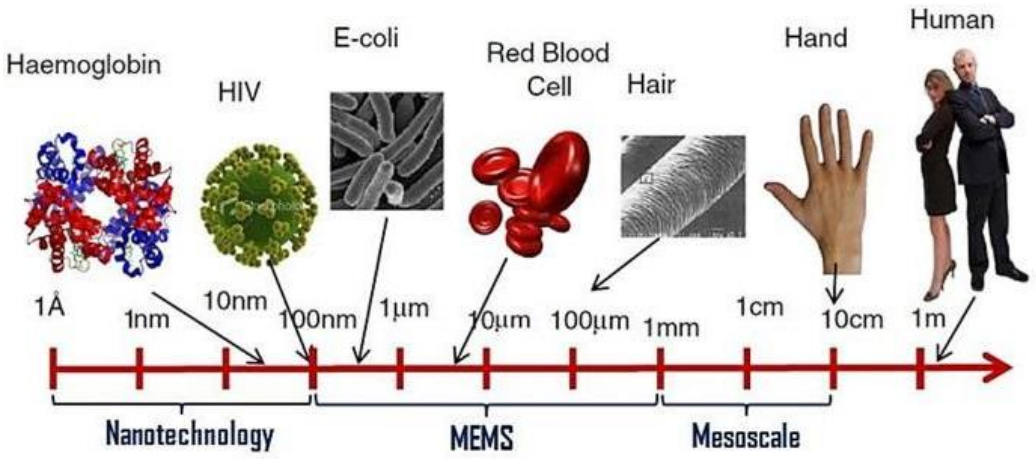

Figure 1-2. MEMS microscopic scale of things

1.1.2 Materials for Microfluidics

Microfluidics channels or dimensions ranges from 1µm to 1000µm [2] in width or height, so the materials need to be chosen accordingly since not all materials are compatible to be fabricated intricately at this micro scale dimensions. The other reasons for selecting the right materials are its effects towards flow, biocompatibility, and absorptivity. Here, all these parameters are discussed in detail with regard to the device.

Common materials used in microfluidic device fabrication (Figure 1-3) include but not limited to are Rigid polymers, polydimethylsiloxane (PDMS) [3]–[6], paper [7], Silicon [8], glass and newly emerged 3d printing (3DP) [9], [10]. Because of their low cost and extensive study, thermoplastics [11], [12], paper and PDMS materials are frequently used in microfluidic device fabrication.

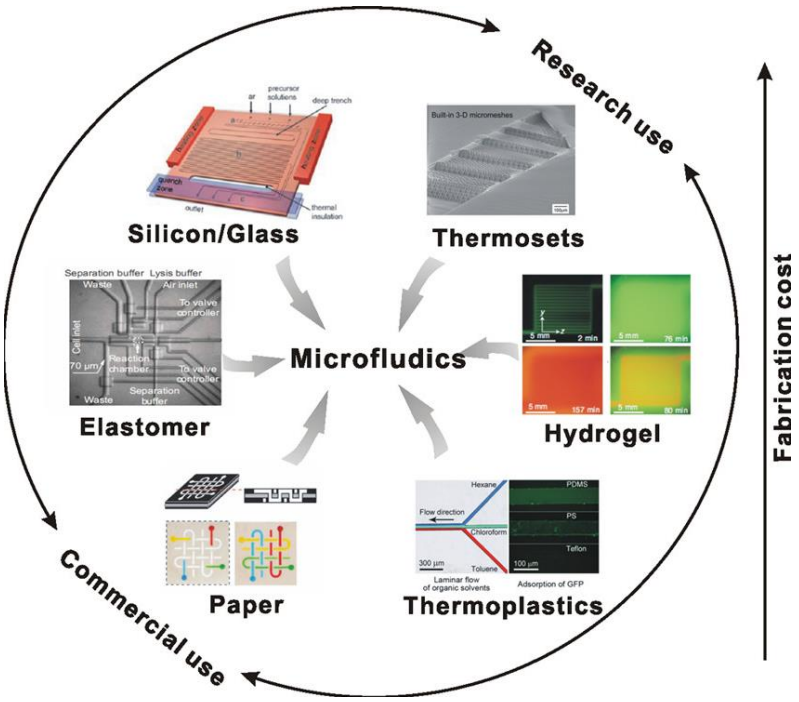

Figure 1-3. Different materials used in microfluidic devices fabrication and their purposes. [13]

Table 1-1. Comparison of common materials used in microfluidic devices.

	Inorganic Materials		**Polymeric Materials**			
Property	Silicon	Glass	Thermoplastics (PMMA,PC, PEEK)	Thermoset Polymers	Elastomers PDMS	Paper
Microfabrication techniques	Photolithography	Photolithography	Thermomolding	Casting, photopolymerization	Casting	Photolithography, printing
Microfabrication	Easy – Medium	Easy – Medium	Easy	Medium	Easy	Easy
Structuring Process	Wet and dry etching	Wet etching, photo structuring	Injection molding, hot embossing, thermoforming, laser ablation	Casting, lithography, etching	Casting	Varies
Possible Geometries	Limited, 2D	Limited, 2D	Many, 2D, 3D	Mostly 2D, 3D possible	Mostly 2D, 3D possible	2D and 3D
Assembly	Easy	Medium	Easy	Medium	Easy	Medium
Interconnections	Difficult	Difficult	Easy	Easy	Easy -Medium	Medium
Young's Modulus (GPa)	High 130 - 180	High 50 - 90	Low – Medium 1.4 - 4.1	Low - Medium 2.0 - 2.7	Very low ~0.0005	Low 0.0003 – 0.0025
Temperature Stability	High	High	Low – Medium	Medium	Low	Low
Acid Stability	High	High	High	High	High	Medium
Organic Solvent Stability	High	High	Low – Medium	Medium – High	Low	Low
Optical Transparency	No	High	Medium to High	High	High	Low
Gas Permeability	No	No	No	No	Yes	Yes
Material cost	Medium	Medium – High	Low – Medium	Medium	Low	Very low

1.1.2.1 PDMS

Elastomeric polymers are solids that resemble rubber and are made of polymer chains that are kept together by the smallest possible intermolecular pressures [3], [14]. These polymers can be stretched due to the weak binding forces, and the few crosslinks between the chains enable the polymer to revert to its original shape after the strain has been released. Polydimethylsiloxane (PDMS) is the most widely used elastomeric polymer in the microfluidics industry. With the advent of soft lithography [7], [15]–[17] in the late 1990s, PDMS was first widely utilized as a substrate. Casting processes can be used to quickly create PDMS devices. Before PDMS is cast and cured on device molds, they are first prepared using conventional photolithography or micromachining methods. PDMS's capacity to adhere to itself and its incredibly low Young's modulus [4], [18] (a property of the material that describes how easily the material can stretch or deform) makes it possible to design micro channels, valves, pumps, and multiple layer devices with intricate fluidic channel designs. PDMS is praised for having practical qualities like optical clarity, non-porosity, biocompatibility, and gas permeability that allow for a range of uses and detecting methods.

Although PDMS is extensively utilized for quick prototyping and in academic microfluidic applications, it is rarely used in commercial applications which is the gap we are building to bridge.

1.1.2.2 Paper

Paper is a particularly valuable substrate for applications that have low cost, flexibility, disposability, porosity, and scalability for large-scale manufacturing. Paper is readily available in a wide range of materials and qualities. Cellulosic fibers found in paper are very porous and have good wicking (hydrophilic) qualities. Paper substrates [7], [19]–[21] can be carefully altered to make some areas hydrophobic while leaving others hydrophilic, directing fluid flow by capillary action. Paper-based devices, in contrast to conventional microfluidic devices, are easy to build without the use of cleanroom facilities, are made of affordable, easily accessible materials, and do not require computer-controlled pumps to function. Due to these features, paper-based microfluidics are more easily accessible to researchers from various academic fields and create a perfect foundation for the creation of point-of-care (POC) [22], [23] diagnostic testing. There are several porosities and thicknesses of paper available. Its surface has a high density of organic functional groups that can be chemically modified and employed to bind reagents or analytes either covalently or non-covalently [24]. Since paper has a high surface-to-volume ratio, it can be used to store dried chemicals and samples for later analysis. Few of the well-known paper microfluidic fabrication methods are Paper cutting, Wax printing [9], [10], Photolithography, Inkjet printing and many others. The current limitations of Paper based microfluidics are sample retention (evaporation problem during sample transport), surface tension limitations towards certain fluids and limit of detection.

1.1.2.3 Thermosetting Polymers

Thermosets, also known as network polymers, are solid, stiff materials with a high degree of crosslinking that limits the motion of their chains. They keep their strength and shape after heating, but they cannot be reshaped [18] once the first heat-forming has taken place. Polyimides, which exhibit great stability at high temperatures, resistance to various solvents, and optical transparency, are typical examples of thermosets utilized in microfluidics for the creation of microchannel architectures, paving the way for applications in 3D microfabrication. Prepolymers, which are the earliest forms of thermosetting polymers [18], are often viscous liquids that can be molded into the necessary shapes before the curing process. Heating or radiation under pressure to generate a firmly cross-linked polymer network is the conventional method of curing. Thermosets like SU-8 and polyimide were employed as negative photoresists for photolithography before being used in microfluidic devices. Microchannel architectures were created using previously used techniques, and then full 2D and 3D microfabricated devices. Thermosets' use in microfluidics has been constrained by their relatively expensive cost, complicated manufacturing process, and structural rigidity (which makes them unsuitable for the manufacture of valves or pumps).

1.1.2.4 Thermoplastics Polymers

Thermoplastics are a type of polymers that, upon heating over the material's specific temperature, can be softened and reconfigured without undergoing any alteration to their chemical structure, making them an appropriate substrate for microfluidics applications.

The presence of weakly cross-linked linear and branched chain molecules [11], [12] allows the polymer backbone to move across extended distances when heated. While staying chemically and dimensionally stable across a broad range of temperatures and pressures, thermoplastics can be fully melted and reshaped, unlike elastomeric and thermosetting polymers, and can also be softened or softened and fully melted. Their study has drawn more interest because of its combination of low manufacturing costs, high strength, and light weight as a possible material that might outperform other polymers for disposable microfluidics. These substances are frequently optically clear, more rigid than elastomers, generally robust, and well-suited for micromachining and duplication operations. Thermoplastics are generally less solvent-incompatible than PDMS, but they are only compatible with alcohols and a small number of other organic solvents. Common thermoplastics [11], [12] including poly (methyl methacrylate) (PMMA), polycarbonate (PC), polystyrene (PS), polyethylene terephthalate (PET), and polyvinyl chloride (PVC) are commonly purchased as solid stock and processed via thermo-molding or micromachining, unlike elastomers and thermosets.

Table 1-2. Overview of properties of common polymers used in microfluidic device fabrication.

Name	Density (g/cm^3)	T_g (°C)	Heat Distortion Temperature (°C)	T_m (°C)	Resistivity (Ω/cm)	Water Absorption (%)	Refractive Index	Young's (Tensile) Modulus (MPa)	Expansion Coefficient (10^6/K)	Resistant Against	Not Resistant Against	Organic Solvent Stability
Polymethylmethacrylate (PMMA)	1.19	110	90	160	$1x10^{15}$	2	1.492	3,200	80	Acids, bases (medium conc.) oil, petrol	Alcohols, acetone, benzole, UV radiation	Attacked by most solvents (e.g. acetone, benzene, dichloromethane)
Polycarbonate (PC)	1.19-1.24	148	125	265	$1x10^{14}$	0.3	1.58-1.6	2,200-2400	70	Alcohols, acids	Hydrocarbons, ketones, KOH	Attacked by most solvents (e.g. acetone, methlene chloride
Polypropylene (PP)	0.9	0-10	100-200	176	$>1x10^{14}$	0.01-0.1	1.49	1,450	100-200	Acids, bases, alcohol, organic solvents, fats	Petrol, benzole, hydrocarbons	Xylol, tetraline, decaline
Polystyrene (PS)	0.9-1.24	110	70	239	$>1x10^{16}$	<0.4	1.59	2,300-4100	30-210	Bases, alcohols	Conc. Acids, ether, hydrocarbons	Attacked by most solvents (e.g. acetone, benzene, dichloromethane)
Polyetheretherketone (PEEK)	1.3	143	250	343	$>1x10^{16}$	0.5		3,700	17	Most organic and inorganic substances	Conc. Nitric acid, sulfuric acid, UV light	
Polydimethoxysilane (PDMS)	1.03	210	200	N/A	$1.2x10^{14}$	0.1	1.43		960	Weak acids and bases	Strong acids, hydrocarbons	
SU-8	1.19	210		N/A	$2.8x10^{16}$		1.58	2,000	52	Acids, bases, most solvents		
Polyimide (PI)	1.42	360-410	400	>700	$>1x10^{12}$	2.9-4	1.7	2,500	20	Acids, bases, solvents		No known solvents

1.1.3 Microfabrication Method or microfluidic Method

The fabrication process varies depending on the substrate selection, as was already mentioned in the previous sections. Photolithography is commonly used in microfluidic manufacture for inorganic substrates like silicon and glass to both define the microfluidic structure and safeguard the underlying substrate. The microfluidic structure is then built using subtractive methods like chemical etching or additive methods like thin-film deposition, and then the channels are sealed using bonding methods.

Replication methods and direct manufacturing methods are the two broad categories into which polymeric microfluidic fabrication techniques can be categorized. Making a master mold is necessary for replication processes like hot and cold embossing, thermoforming, injection molding, and casting before the final product can be produced from it. Laser ablation [25], micromachining, stereolithography , and most recently 3D printing [9], [26] are direct fabrication techniques. Figure 1-4 depicts the main procedure for microfabrication. With a master mold, the most common reproduction techniques, such as hot and cold embossing [20], injection molding, thermoforming, and casting, are all carried out (the geometrical inverse of the desired structure). The master is often created using micromachining on a polymeric substrate or through conventional photolithography on silicon substrates. Accuracy and precision during mold manufacturing are crucial since the quality of the finished device is directly tied to the quality of the master mold. In the process of hot embossing, a thermoplastic substrate is heated above its T_g and the master mold, which is also heated, is pressed into the polymer substrate. Next, the thermoplastic substrate and master mold are both cooled to below their T_g so that the mold may be removed for demolding. Similar steps are taken in

thermoforming, where the substrate, a thin polymer film, is compressed into the master mold using pneumatic pressure. Thermoforming is better suited for rounder shapes where geometric accuracy is less crucial because it has lower replication accuracy than hot embossing and is unable to make high aspect ratio structures with sharp angles. Granules of pre-dried polymer are injected into a heated barrel during injection molding using a screw. The polymer melts on the way to the mold, where it is injected as liquid polymer under high pressure. The simplest replication technique is elastomer casting, which calls for pouring the ready elastomer (a mixture of monomer and curing agent) over the master mold piece. Hot Injection Embossing Molding Using a Thermoforming Cast Generation of Photomasks Plasma Etching via Laser Ablation 3D printing with laser ablation Design for Precision Machining, Cutting, Drilling, and Fabrication of Electrodes Bonding for Surface Modification Sealing Design Quality Assurance Micro Structuring Back-End Operations Direct Manufacturing Methods Mold-replication methods include allowing the mold to cure.

Casting is the most straightforward way; however, it has a lesser throughput than other methods. Recently, acrylonitrile butadiene styrene was employed in 3D printing to create a positive mold of a 3D depiction of microfluidic channels (ABS). After that, the PDMS was allowed to cure while the mold was hanging in it. The ABS was then dissolved in acetone to remove the mold. Without the need to bind numerous layers, this method enabled the quick fabrication of genuinely 3D PDMS microfluidic devices. Because of its many advantageous qualities, including simplicity, material characteristics, cost, surface chemistries, and high replication precision, casting has become quite popular. The majority of commercially used techniques are hot embossing, injection molding, and

thermoforming, with elastomer casting [12], [27], [28] predominating in academic research. The advantage of having a very quick turnaround from computer-aided design (CAD) to a finished item makes direct manufacturing techniques like precision micromachining and laser ablation excellent for prototyping. There are, however, several drawbacks. Although the time from concept to finished device may be fast, the total fabrication time per device, which is often hours, is relatively high, making these approaches unsuitable for mass manufacturing. Another drawback is the intrinsic surface roughness these fabrication techniques leave behind, which may not be smooth enough for some applications, especially those needing optical clarity, although the roughness can be reduced by solvent polishing.

The final stage in device fabrication, regardless of the fabrication technique, is bonding. Except for a few straightforward paper-based devices, the majority of microfluidic devices need sealed channels to function. The channel plate must be attached to another material in order to seal the channels because very few fabrication techniques can produce completely enclosed channels. This poses a special set of difficulties since the channels must be shut without modifying their physical characteristics, their size, or clogging. Several bonding methods, including heat, solvent, and adhesive bonding, have been developed. PDMS is commonly bonded by oxygen plasma exposure or conformal contact, depending on whether the bond is temporary or permanent. The employment of adhesive and thermal bonding techniques for thermoplastic bonding is common. During thermal bonding, pressure is typically applied while the created structure and cover plate are heated to a temperature above the value T_g. It is important to take precautions to reduce temperature and pressure changes that could cause channel deformation. As

adhesive-based procedures are by nature straightforward, they are frequently used. The application of a thin coating of glue, such as an adhesive that sets by the evaporation of solvent or a UV curable substance between the polymer substrates, can be used to adhere layers. Additional bonding methods, which are variants on thermal bonding and provide localized heating as opposed to global heating to lessen the likelihood of channel deformation, include microwave adhesion, ultrasonic welding, and laser welding. Solvent welding is another typical way of layer bonding. The polymer chains can move around and diffuse into the solvated layer by adding a suitable solvent to the polymer surface. This mobility causes the chains between the touching surfaces to extensively intertwine, creating an extremely solid bind.

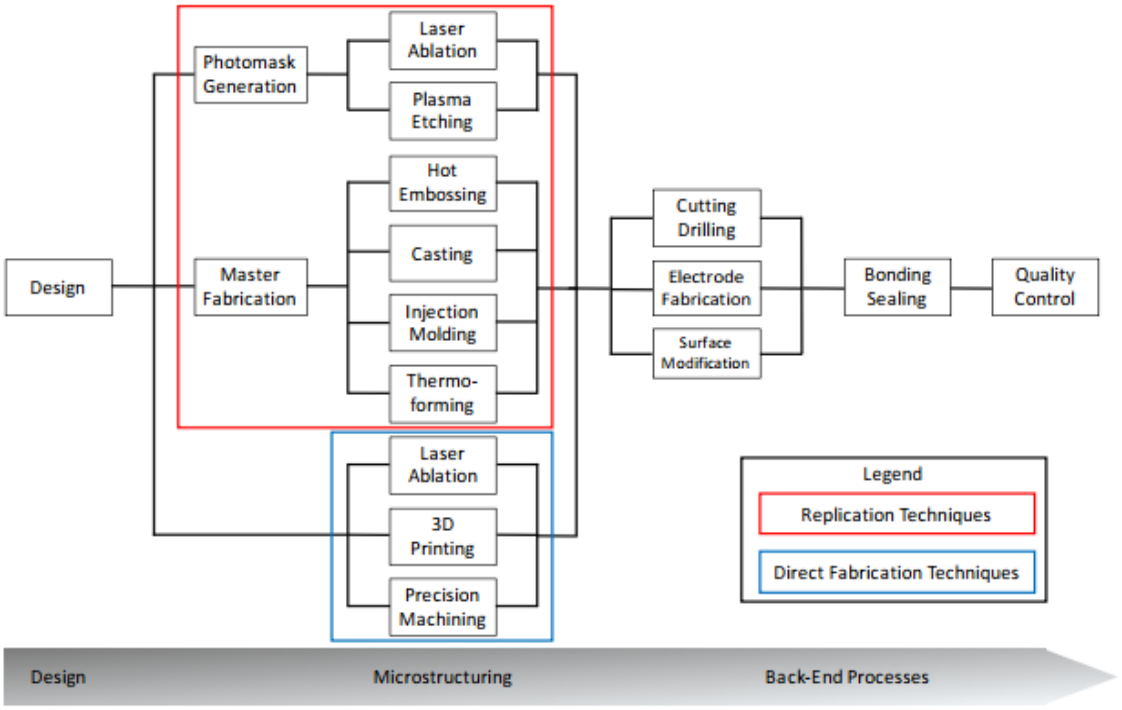

Figure 1-4. Fabrication process of polymer based microfluidic devices.

1.1.4 Function in microfluidic systems

The fundamental activities in a microchip system that, when coupled, result in the desired analysis is called microfluidic functions. Sample preparation, separation, detection, and liquid conveyance are important processes. The hardware requirements for each platform are determined by the functionalities of the devices and the analysis's ultimate goal.

1.1.4.1 Sample preparation

Clinical diagnosis of various diseases has a great deal of promise for the examination of biomarkers, which are biomolecular indicators of medical disorders. These biomarkers are usually present in intricate biological matrices or body fluids, and sample preparation is virtually always necessary before analysis. Large volumes (> mL) and knowledgeable individuals are frequently required for sample preparation stages, which further extends the time and cost of the analysis. Thus, quick, and efficient sample preparation methods are required to aid in early diagnosis. It can be difficult to prepare samples for microfluidic devices, but the benefits which include faster analysis times, automation, higher throughput, and less reagent consumption make the investment worthwhile. Recently, several microfluidic devices that can carry out sample preparation procedures like purification, preconcentration, and labeling on a chip prior to quantification have been disclosed. In a microfluidic setting, separation methods have also improved for the analysis of molecular biomarkers. Analysis is greatly streamlined by the capacity to isolate minute quantities of required analytes from a complicated sample matrix, like

blood. By replacing time-consuming benchtop procedures with on-chip sample preparation could shorten analysis times and even enable point-of-care applications.

1.1.4.2 Separation methods

Common separation methods include microfluidic filters for cell separation and sorting, Hydrodynamic separation and sorting, Deterministic lateral displacement separation and sorting, inertial separation, and sorting and many more. But in this article the device working principle is based on the combination of above-mentioned techniques.

1.1.4.2.1 Inertial separation and sorting

It is a reliable and simple method since inertial separation relies only on channel geometry and hydrodynamic forces [29], [30]and does not require cell manipulation by outside forces. Straight and spiral microchannels are the most typical inertial separation architectural designs. This method uses an asymmetrical sheath flow and correct channel geometry to provide a gentle inertial force on the sample fluid in the focused, curved sample flow segment [31]. This technique keeps tiny particles on or close to the original flow streamline while deflecting bigger ones. Shear gradient lift and wall effect lift, two inertial lift forces, have been characterized as balancing each other out in this concentrating phenomenon. Additionally, by adjusting channel shape, it is possible to change both the quantity and location of equilibrium points. In microfluidic devices, curved channels like arcs and spirals [32], [33] Figure 1-5.a produce a second inertial effect. As a fluid is propelled around a curve, lesser momentum fluid near the channel

sides is displaced by higher momentum fluid in the channel's center. The resulting counter-rotating vortices, which are perpendicular to the principal channel flow, may also affect the locations of the particles. In this secondary flow, cells may be entrained and dragged perpendicular to the primary flow.

1.1.4.2.2 Microfluidic filters for cell separation and sorting

Simple techniques for sorting cells based on size or deformability as biomarkers include microfluidic or microscale filters. Using these methods, you can precisely alter the filter's pore size to suit your demands. These filters, however, encounter a number of difficulties, such as the variety of cell sizes within a population, clogging, and fouling. The main filter designs for these methods are either Weir-type, Pillar-type and Crossflow as mentioned in Figure 1-5.b.

1.1.4.2.3 Deterministic lateral displacement separation and sorting

The size-based cell sorting method known as Deterministic Lateral Displacement (DLD) [34]–[36] uses an organized grid of barriers (micropost array). Particles or cells are forced into precise trajectories through the device by the laminar flow, in combination with interactions with the array Figure 1-5.c. The pattern of the array determines the movement of cells or particles perpendicular to primary flow. Below a specific size, cells or particles follow streamlines across the gaps in the array with no net deviance from the initial streamline. In order to cross successive streamlines, particles larger than the critical size are displaced laterally, with each row moving at an angle given by the post offset

distance. The spacing between posts and the offset of posts determine the required particle size for fractionation.

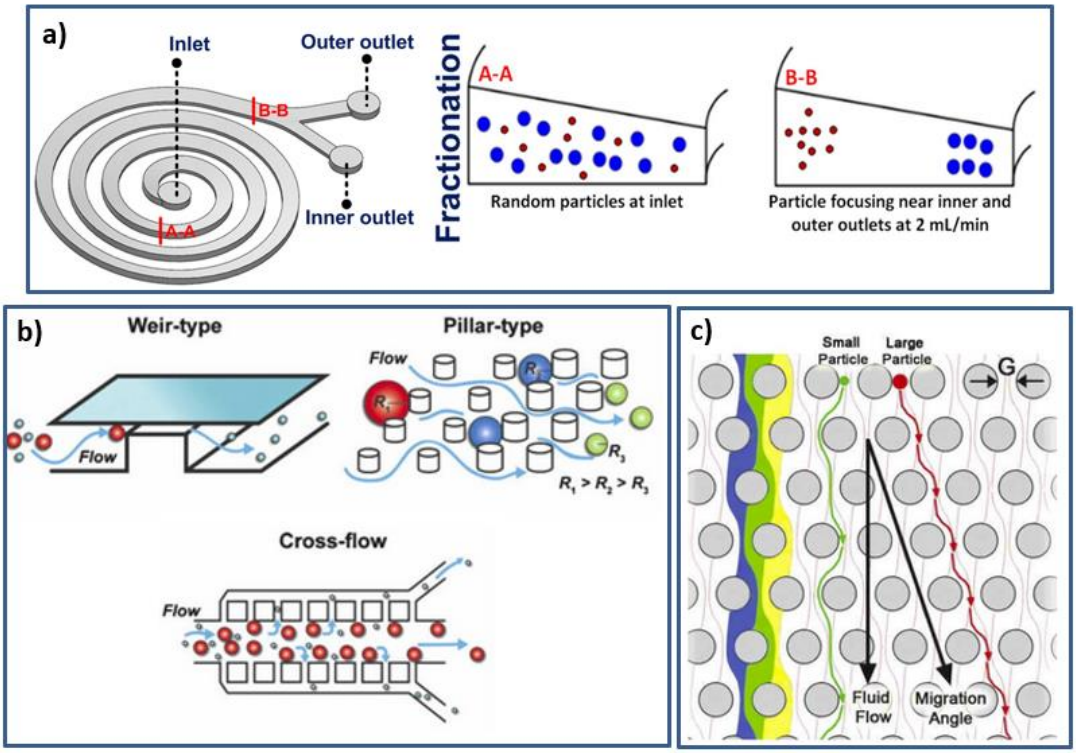

Figure 1-5. Some examples of inertial, filter and DLD based separation techniques

1.1.4.3 Detection methods

The most common detection method used in microfluidic systems is optical detection. While the other techniques such as Mass spectrometry (MS) [37], [38], next generation sequencing (NGS) and polymerase chain reaction (PCR) are popular, the main goal was simplicity in this article. Optical detection techniques have a number of benefits. They can be used to monitor a wide range of substances, are typically isolated from the fluid, and have good detection limits. Its non-contact non-destructive detection technique has a few significant applications and future potential in biological science and environmental

monitoring. The sample is enlarged by lenses, which create an image on a camera sensor. To isolate light in a certain wavelength range of interest, an optical filter is used. Finally, the light from the sample is captured by an optical detector, also known as a camera sensor. After that, data is extracted from the detector and saved for later study. Because of the accessibility of parts and simplicity of linking such systems to a microfluidic platform, such microscopy systems are fairly common. This kind of setup can be employed in a microfluidic system because it is straightforward and takes little time to construct. Yet, because of the lengths of the optical paths involved, such systems are challenging to miniaturize. The detection of light emitted by a sample (a fluorophore) that has been stimulated by absorbing light from an incident beam is the basis of fluorescence measurements [37], [39]. The cells or microparticles used to detect florescence are labeled with fluorophores, which absorb and emit light at specific wavelength ranges. In a microfluidic channel where the targeted analyte is flowing at a specific flowrate, a beam of light is utilized to stimulate the tagged analyte. Later on, the stimulated analyte emits light with a different wavelength. An optical filter, for example, can isolate the emitted light, which can then be utilized to measure or photograph the analyte. Measurements of fluorescence are highly sensitive and selective. In this article, we will mainly be using optical and fluorescence-based measurements for simplicity and compatibility with the device's material.

1.1.4.4 Fluid manipulation

1.1.4.4.1 Pumps

Because it makes it easier for sample solution to flow, fluid pumping is a crucial task in microfluidic devices. The incorporation of micropumps inside microfluidic systems lowers the demand for external equipment and the dead volumes caused by pump interface. External pumping systems can make the systems big, pricey, and difficult to utilize. Several types of streamlined pumping systems have been created using capillary forces, degassing pumps, syringes, pipettes, screws, and finger actuation to overcome these problems. Electrostatic forces and ions interact in nonconducting fluids to produce EHD pumping. It was discovered that the electrode geometry affected the performance of EHD micropump, with an asymmetric geometry producing more pressure with less power than a symmetric design. Acoustic pumping uses the force created when longitudinal waves contact with the surrounding fluid to move liquid.

1.1.4.4.2 Valves

By regulating both movement and flow direction, valves play a crucial part in fluid manipulation. Check and burst valves are examples of passive valves. Check valves permit unidirectional flow, while burst valves control flow by irreversibly expanding the channel size under high pressure. The two types of valves based on their principle of working are active and passive microvalves. Active mechanical microvalves are made up of a boss or membrane that is mechanically movable and connected to an actuation mechanism that can seal an orifice and obstruct the flow path between the inlet and exit

ports. An integrated magnetic, electrostatic, piezoelectric [40]–[42], or thermal micro actuator can be used as the actuator. The fluid that the valves control determines whether they are open or closed, making them passive microvalves. The most popular passive microvalves are ball, membrane, and flap valves.

1.1.4.4.3 Mixing

Since turbulent mixing does not happen in low Reynolds number microfluidic devices, diffusive species mixing, while still significant, is a naturally slow process. So, the purpose of microfluidic mixing schemes is to improve mixing efficiency so that a comprehensive mixing performance can be obtained within shorter mixing channels, which can lower the typical size of microfluidic devices. Similar to valves, mixing is of two types, passive and active mixing [43]–[45]. Active mixing is achieved with the help of external forces on the sample, some of the external forces are Acoustic, Dielectrophoretic [46]–[48], Thermal, Magneto-hydrodynamic flow [49]–[53] and others which help improve the mixing performance. Passive mixing usually requires a longer mixing channel to achieve satisfactory mixing results. Some of the passive micromixers are lamination based, zigzag channels, twisted channels, and others.

Table 1-3. Summary of fluidic manipulation in microfluidic devices.

Function	Category	Actuation Mechanism	Approach	Advantages	Disadvantages
Pumping	Passive	Capillary (nonmechanical)	Spontaneous fluid motion by capillary action	Simple and straightforward; no additional fabrication steps	Flow is not continuous over a long period of time; flow cannot be controlled easily
	Active	Electroosmotic (nonmechanical)	Electroosmotic force through interaction of applied electric field with electrical double layer	Ease of manufacture; constant flow rate can be manipulated by the applied voltage	Adsorption can affect flow; only works with conductive solutions
	Active	Electrochemical (nonmechanical)	Generation of gas bubbles, such as by electrolysis	Ease of manufacture; small size; low power	Gas bubbles and electrochemical by- products can block conduction between the electrodes and hinder actuation
	Active	Pneumatic peristaltic (mechanical)	Sequential actuation of a series of pneumatic microvalves with pressurized air	Easily integrated; fast response time	Requires external equipment to supply compressed air; pulsed fluid flow
	Active	Electrohydrodynamic (nonmechanical)	Interaction between electrostatic forces and ions in nonconducting fluids	Easily integrated; can pump a variety of liquids; requires low voltages	Flow rate depends on material surface properties; typically low flow rates and pressures
	Active	Acoustic (mechanical)	Force produced by the interaction of longitudinal waves with the surrounding fluid	Does not generate byproducts that can contaminate sample	Applied frequencies can denature biomolecules and lyse cells
	Active	Magnetohydrodynamic (nonmechanical)	Lorentz force produced when orthogonal electric and magnetic fields are applied to a conducting solution in a microchannel	Ease of integration; continuous flow	Possible electrolysis of water at the electrodes; bubble formation
Valves	Passive	Check valve (mechanical)	Unidirectional flow; valve is opened by employs fixed membranes, flaps, etc. increase in pressure;	Simple; can withstand high backpressures	Can have a large dead volume
	Passive	Capillary burst valve (nonmechanical)	Sudden changes in geometry or surface chemistry of microchannel	Simple design and fabrication	Efficiency is lower with low surface tension liquids
	Active	Pneumatic (mechanical)	Deflection of an elastomeric membrane by application of external pressure	Easily integrated; large actuation force	Requires a control layer; needs external pneumatic inputs
	Active	Phase-change (nonmechanical)	Employs materials with a volume difference in a phase change, such as a hydrogel, paraffin wax, or water/ice	Ease of fabrication and operation	Materials can contaminate samples if in direct contact
	Active	Magnetic (mechanical)	External or integrated magnets for moving magnetic materials	Generates high force	Complex fabrication
Mixing	Passive	T- or Y-mixers	Fluid streams from separate inlets combine at a channel intersection and mix by diffusion	Simple design; easy fabrication	Slow mixing; requires long channels
	Passive	Lamination	Designs that split the main flow stream into multiple streams and then recombine them	Reduces diffusion distance; uniform mixing across entire channels	Fabrication is complex
	Passive	Chaotic advection	Secondary flows generated when fluid passes through twisted 2D or 3D structures, zigzag microchannels, or channels with ridges and grooves	Increases contact surface; mixing achieved at almost all flow rates	Mixing is not uniform over the entire channel cross section
	Active	Electrokinetic	Unstable flow caused by a force in the bulk liquid generated by coupling of electric fields and conductivity gradients	Ease of fabrication and integration	Requires high electric fields
	Active	Acoustic	Acoustic waves that cause secondary flow and mixing	Does not generate byproducts that applied voltages can	Temperature increase may damage biological samples
	Active	Magnetohydrodynamic	Fluid is mixed through changing flow caused by nonsynchronous magnetic and electric fields	Simple fabrication; fast and effective	Only works with conductive solutions

1.2 PDMS Microfluidics

1.2.1 Background

Due to its inherent non-toxic, transparent, stretchable, biocompatible, hydrophobic, insulating, and negative triboelectric properties, polydimethylsiloxane (PDMS) is widely used in a variety of fields, including microfluidics, microneedles, biology, medicine [3], [6], [54], chemistry, optics, electronics, architecture, and emerging sustainable energy. For instance, PDMS is a good choice for the material selection of microfluidics, microneedles, biomedical, and chemistry microchips as well as for optical inspection and wearable electronics due to its flexibility (tunable young's modulus), biocompatibility, non-toxicity, strong stability, and high transparency. Among the commercially available forms of PDMS, the Sylgard-184 (Dow corning) is widely used due to its popularity and intense published results. From a fabrication perspective, PDMS's capacity to recreate structures at the nanoscale and be quick and simple to connect with glass systems are its most impressive qualities. Transparency, which permits direct optical access into microchannels for real-time process monitoring and precise quantification of the phenomenon under study, is another important and promising component of microfluidics. The superior biocompatibility, permeability, and low autofluorescence properties of PDMS are also discovered, opening up a wide range of opportunities in the fields of biotechnology and biomedical engineering. All of these elements merely improved its eligibility for Lab on a chip (LOC) [54], [55] application that are affordable

in both academics and industry. Figure shows the number of publications of microfluidics per year shows the rapidly increasing works being performed in this field.

1.2.2 Fabrication Methods

The well-known methods of fabricating microfluidic devices using PDMS are by the use of Photolithography and 3D printing.

1.2.2.1 Photolithography

Throughout the past thirty years, photolithography has been one of the primary techniques for patterning polymers. It involves transferring the geometric patterns on a mask to a silicon wafer's surface [8]. An optical technique for imprinting a pattern on a substrate is photolithography [26]–[28]. According to the type of light used like ultraviolet, deep ultraviolet, extreme ultraviolet, or X-ray photolithography methods can be categorized. The smallest feature size that can be created in the photoresist depends on the wavelength of light being employed. The Figure 1-6 underlies every photolithography process step by step. The substrate is first covered with the photoresist, which is a light sensitive polymer material. The substrate is then subjected to electromagnetic radiation, which alters the molecular structure and causes a change in the material's solubility, all while the pattern mask is being applied. The developer solution is then applied to this substrate. Aqueous developer solutions often dissolve away portions of the photoresist that have been exposed to light or have not, depending on the type of photoresist. The two types of photoresist (PR) are positive and negative photoresist. The process usually

remains the same, but the end result is a mirror image of the pattern when using positive or negative PR. In a positive PR, the areas exposed to light will be removed in the developing process while the areas not exposed will remain, but the opposite happens if a negative PR is used instead. The Figure 1-6 shows the whole process of photolithography. The photoresist is equally spread using a spin coater instrument which spins at a specific speed (related to the photoresist) and forms a uniform layer of known thickness. The baking of sample is usually conducted on a hot plate at the specified temperature. The UV light is shined upon the sample using a mask aligner containing a UV lamp emitting certain wavelength of light (chosen specifically to affect the photoresist). The developer process is done using a wet solution in a beaker for a calculated amount of time and agitation of the solution. A detailed description of the parameters used in photolithography experiments is listed in Table 1-4

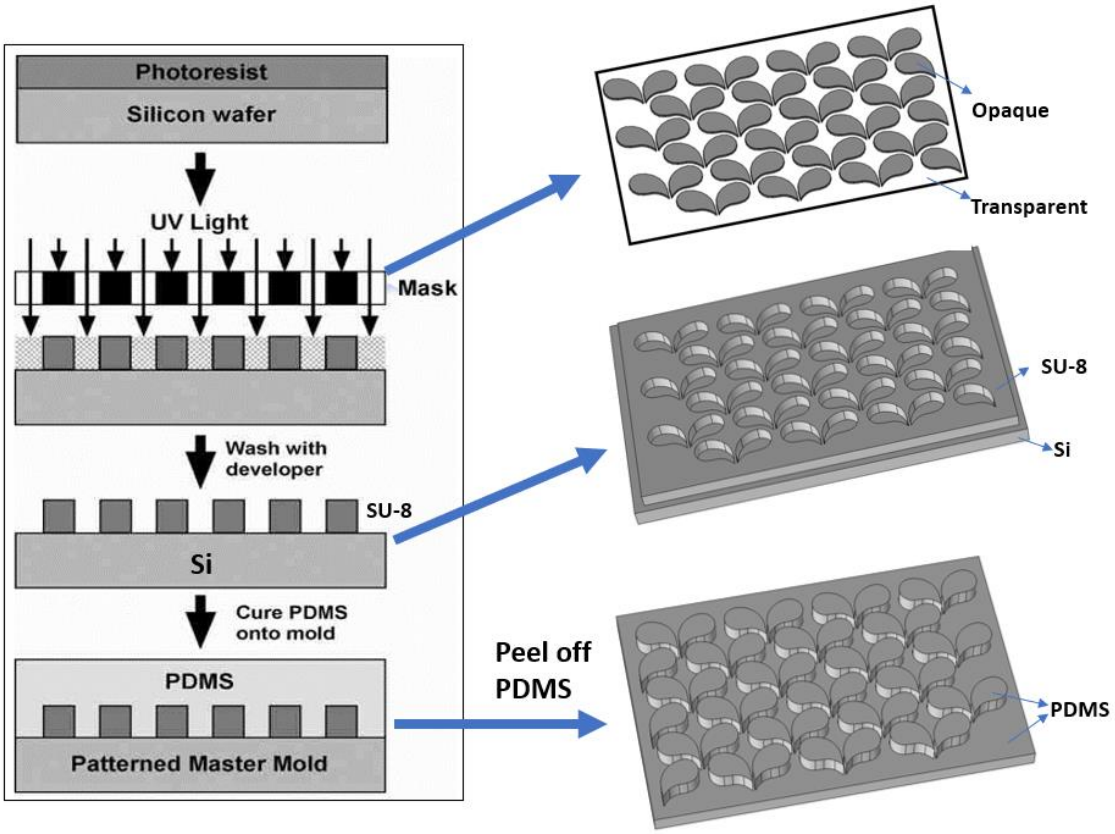

Figure 1-6. Photolithography process step by step for PDMS based microfluidic devices.

Table 1-4. Detailed Photolithography parameters

PR type	**SU-8 3025** for master mold fabrication	**AZ5214E** for hard mask fabrication
Cleaning	Acetone, Methanol, DI Water and Nitrogen dry	Acetone, Methanol, DI Water and Nitrogen dry
Spin Coating	500rpm for 10sec 500-2000rpm for 5sec	500rpm for 10sec 500-2000rpm for 5sec

	2000rpm for 30sec	2000rpm for 30sec
Pre-baking	70°C for 3min 95°C for 15min	95°C for 2min
Exposure	Expose time for 2.5-3min using 900W bulb outputting ~2mJ/cm^2 energy per sec with the use of a PL-360-LP filter	Expose time for 20sec using 900W bulb outputting ~2mJ/cm^2 energy per sec
Post-baking	70°C for 1min 95°C for 8min	95°C for 2min (optional)
Development	Wet developing using SU-8 Developer for ~1min with agitation	Wet developing using AZ400K (1:4 prediluted) Developer for ~1min with agitation
Development additional steps	Alternate wash steps required with SU-8 developer and IPA	NA
Hard Bake	80°C for 60min	95°C for 5min
Post Development	PDMS casting on master mold	Etching to remove exposed iron oxide features to fabricate mask

1.2.2.2 3D Printing

The phrase "3D printing" refers to a number of manufacturing processes that construct parts layer by layer. Each has a unique manner of shaping plastic and metal components, as well as variations in material choice, surface quality, durability, manufacturing efficiency, and price. Some of the predominantly used 3D printing are Stereolithography (SLA) [9], [56], Selective laser sintering (SLS), Digital light process (DLP) [57], [58] and Electron beam melting (EBM). Usually, a liquid resin of certain viscosity is squeezed to a certain thickness and a UV light source (or equivalent curing wavelength light source) is shined upon it in a certain pattern. The part exposed to the light will harden and the design structure is created, and so on the printing takes place layer by layer with each layer cured every time with the design layout. The following table shows the parameters each type of 3D printing mechanism uses and their advantages and disadvantages.

Table 1-5. Comparison of 3D printing Methods

Printing method	Materials	Advantages	Disadvantages
FDM	Thermoplastic polymers	Simple and Cheap	Low resolution, Roughness issue, Limitation in complexity
PolyJet (material jetting)	Photocurable polymer	Multi-material, Smooth surface and high quality	High cost
DIW	Polymers, ceramics	Diverse material versatility	Low resolution, Fragile, Post curing
SLA/DLP	Photocurable resin	Smooth surface and Recyclable raw material	Single material, Limited material, Resin absorbs moisture
DLW	Photoresist, Photocurable polymer	High resolution, No need for support	High cost, Limited material, Time consuming
SLS	Metal powder, ceramic powder, polymer powder	No need for support, Recyclable raw material and High quality	Roughness issue, High cost, Post processing

1.2.2.3 Other Methods

PDMS fabrication can be achieved using other not so popular methods namely Micro-cutting, ultrasonic manufacturing, laser ablation [25], electron beam machining, focused ion beam machining and others. Each of these methods is currently being researched to improve them to replace traditional photolithography and 3D printing. The following table shows the comparison between each method and their minimum feature size and other parameters listing out their advantages over the other.

Table 1-6. Comparison of other technologies for master mold fabrication

Technology	Achievable Roughness Ra	Minimum Feature Size	Resolution Tolerance	Accuracy Tolerance	Typical Aspect Ratio	Typical Structural Dimension
Micro-cutting	65 nm	6.7 µm	2 µm	3 µm	<50	<1 mm
Ultrasonic machining	NA	5 µm	5 µm	NA	<7	NA
EDM	100 nm	5 µm	3 µm	1 µm	<20	<1 mm
ECM	28 nm	150 nm	5 µm	2 µm	<10	NA
Laser Ablation	100 nm	<1 µm	~1 µm	3 µm	<10	<500 µm
FIB	0.58 nm	40 nm	5 nm	100 nm	10	500 nm
E-beam	NA	10 nm	20 nm	NA	<2	<500 nm
X-ray LIGA	10 nm	50 nm	20 nm	300 nm	<100	<1 mm
MEMS process	10 nm	Few µm	NA	Few µm	<40	<1 mm
µ-SL	NA	<1 µm	120 nm	NA	NA	<1 mm

1.2.3 Future Prospects

The material PDMS is adaptable and has great qualities for microfluidics. It is readily available to laboratories around the world, is inexpensive, and is simple to shape. Its

innate hydrophobicity restricts its utility. Although gas-phase processing enables the introduction of many surface chemistries, the PDMS surface is easily harmed. When organic solutions are used in a wet chemical modification process, however, chemical compatibility becomes a problem. Due to the ease of the process, dynamic coatings comprising surfactants and ionic liquids are becoming more and more common for PDMS surface modification [59], [60]. However, the surface modifiers employed here may interact with elements of the sample solution, potentially obstructing the analytical work. Surface modification of PDMS to improve or change certain aspects of the PDMS behavior could give a boost that is necessary for further development of PDMS towards a clinical application setting.

1.3 Applications

Table 1-7. Microfluidic applications overview with the use of different materials.

	Inorganic Materials		Polymeric Materials			Paper
Application	**Silicon**	**Glass**	**Thermoplastics**	**Thermoset**	**Elastomers**	**Paper**
Capillary Electrophoresis	Excellent	Excellent	Good	Good	Moderate	N/A
Electrochemical Detection	Good	Good	Moderate	Moderate	Limited	Moderate
Organic Synthesis	Excellent	Excellent	Moderate to Good	Good	Poor	N/A
Droplet Formation	Excellent	Excellent	Good	Good	Moderate	Moderate
PCR	Excellent	Excellent	Good	Good	Good	N/A
Protein Crystallization	Poor	Poor	Moderate	Poor	Good	N/A
Bioculture	Moderate	Moderate	Moderate	Moderate	Good	Good
Cost of Production	High	High	Low	High	Medium	Low
Reusability	Yes	Yes	Yes	Yes	No	No
Disposable Device Use	Expensive	Expensive	Good	Expensive	Good	Good

1.3.1 Point of care diagnostics

The healthcare industry is evolving despite the ever-increasing degrees of automation used to cut costs while enabling the examination of numerous samples. Economic pressures and the widespread belief that healthcare has to be more individualized and less fragmented are two reasons for this development. This has resulted in the development of wellness centers inside of neighborhood pharmacies and new startup businesses that specialize in point-of-care Figure 1-7.a testing (PoCT) [1], [22], [23], [61], [62] also known as bed side testing. Microfluidics devices, particularly in particular those made of polymer or paper, provide qualities like disposability and affordability that are necessary in this industry. Even though there isn't yet a wide distribution of these kinds of devices, microfluidic applications in POC are already utilized for drug misuse screening, glucose biosensors [63], [64], HIV detection, pregnancy testing, and HIV testing. Yet, using microfluidics enables the acquisition of a number of benefits, including speed, throughput, and minimal sample consumption, all of which are essential in POC applications. Moreover, microfluidic-based POC devices are simple to use and produce, making their application especially attractive in underdeveloped nations where there is a tremendous need for reliable yet affordable medical equipment.

1.3.2 Drug administering

The injection of a specific chemical molecule to a biological system for therapeutic purposes is typically referred to as "drug delivery" [65].Examples of traditional medication delivery techniques include oral administration, inhalation, and injection via

the skin [66]. The fact that the drug's pathway, or the actual physical distance between the inoculation site and the area of interest, is frequently too long, potentially rendering the treatment useless, is one of the main disadvantages of these approaches. Using Microfluidics, Drug delivery can interact at organism level, tissue level [67] and also at cellular level. The organism level usually involves some type of microneedles which remove the pain from the equation by infusing without triggering the pain sensors in the human skin due to their sheer size being too low enough to trigger sensitivity to pain Figure 1-7.b. At the tissue level, bio capsules [68]–[70] are used to encapsulate transplanted and/or micro engineered tissue into a biodegradable and semi-permeable particle to prevent rejection of these tissues by the immune system of the recipient organism. Studying a drug's effects at the cellular level [71]–[73] in varied physicochemical microenvironments is one of the key opportunities provided by microfluidics. In fact, a microfluidic-based cell culture platform can produce various environmental profiles and replicate in vivo settings. Moreover, microfluidics enables accurate and controlled drug delivery to the culture chamber [3], [74], making it feasible to track, for example, how the cells react to high concentrations of drug or other biochemical stimuli.

1.3.3 Cell Analysis

Cell analysis is another area where microfluidics is receiving positive feedback. Since it is very tempting to have diverse modules for cell culture, sorting, and lysis [75] in the same tiny device, many researchers are moving in this direction [76]. Particularly in cell cytometry, which requires accurate and precise flow control, microfluidic-based devices

are frequently used. Also, the use of microfluidic devices enables the improvement of sensitivity because the size of the entire measuring system is significantly reduced and is now smaller than that of a single cell. Cellular biosensors [1], [63], or sensors that take advantage of cellular physiological reactions to various stimuli, such as toxic feedbacks, are a type of microfluidic device Figure 1-7.c. Finally, microfluidic technologies enable highly accurate reproduction of in vitro cell-cell, cell-substrate, and cell-medium interactions. Cells and their microenvironment can also be accurately monitored while being cultured inside the microfluidic device.

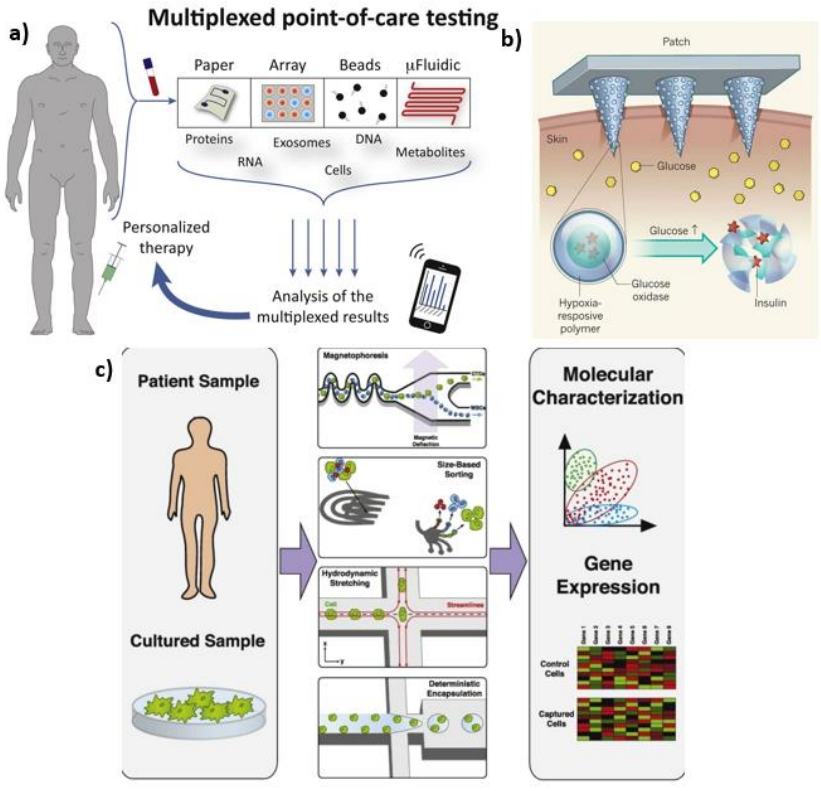

Figure 1-7. Overview of clinical applications of microfluidic devices

1.4 References

[1] E. A. Flores-Contreras, R. B. González-González, I. P. Rodríguez-Sánchez, J. F. Yee-De León, H. M. N. Iqbal, and E. González-González, "Microfluidics-Based Biosensing Platforms: Emerging Frontiers in Point-of-Care Testing SARS-CoV-2 and Seroprevalence," Biosensors, vol. 12, no. 3. MDPI, Mar. 01, 2022. doi: 10.3390/bios12030179.

[2] X. Xiong, L. Zhang, J. Hu, and L. Hmurcik, "Introducing the small world-developing MEMS/nanotechnology curriculum," in ASEE Annual Conference and Exposition, Conference Proceedings, American Society for Engineering Education, 2009. doi: 10.18260/1-2--4555.

[3] S. Torino, B. Corrado, M. Iodice, and G. Coppola, "Pdms-based microfluidic devices for cell culture," Inventions, vol. 3, no. 3. MDPI Multidisciplinary Digital Publishing Institute, Sep. 01, 2018. doi: 10.3390/inventions3030065.

[4] K. Raj M and S. Chakraborty, "PDMS microfluidics: A mini review," Journal of Applied Polymer Science, vol. 137, no. 27. John Wiley and Sons Inc., Jul. 15, 2020. doi: 10.1002/app.48958.

[5] L. Lin and C. K. Chung, "PDMS microfabrication and design for microfluidics and sustainable energy application: Review," Micromachines, vol. 12, no. 11. MDPI, Nov. 01, 2021. doi: 10.3390/mi12111350.

[6] M. I. Khot et al., "Characterising a PDMS based 3D cell culturing microfluidic platform for screening chemotherapeutic drug cytotoxic activity," Sci Rep, vol. 10, no. 1, Dec. 2020, doi: 10.1038/s41598-020-72952-1.

[7] S. Nishat, A. T. Jafry, A. W. Martinez, and F. R. Awan, “Paper-based microfluidics: Simplified fabrication and assay methods,” Sens Actuators B Chem, vol. 336, Jun. 2021, doi: 10.1016/j.snb.2021.129681.

[8] H. M. Ji, V. Samper, Y. Chen, C. K. Heng, T. M. Lim, and L. Yobas, “Silicon-based microfilters for whole blood cell separation,” Biomed Microdevices, vol. 10, no. 2, pp. 251–257, Apr. 2008, doi: 10.1007/s10544-007-9131-x.

[9] S. Razavi Bazaz et al., “3D Printing of Inertial Microfluidic Devices,” Sci Rep, vol. 10, no. 1, Dec. 2020, doi: 10.1038/s41598-020-62569-9.

[10] H. Y. Jeong, E. Lee, S. C. An, Y. Lim, and Y. C. Jun, “3D and 4D printing for optics and metaphotonics,” Nanophotonics, vol. 9, no. 5. De Gruyter, pp. 1139–1160, May 01, 2020. doi: 10.1515/nanoph-2019-0483.

[11] A. Shakeri, N. A. Jarad, S. Khan, and T. F Didar, “Bio-functionalization of microfluidic platforms made of thermoplastic materials: A review,” Analytica Chimica Acta, vol. 1209. Elsevier B.V., May 29, 2022. doi: 10.1016/j.aca.2021.339283.

[12] Y. Chen, “ii PATTERNING ELASTOMER, THERMOPLASTICS AND SHAPE MEMORY MATERIAL BY UVO LITHOGRAPHY AND SOFT LITHOGRAPHY.”

[13] K. Ren, J. Zhou, and H. Wu, “Materials for microfluidic chip fabrication,” Acc Chem Res, vol. 46, no. 11, pp. 2396–2406, Nov. 2013, doi: 10.1021/ar300314s.

[14] P. N. Nge, C. I. Rogers, and A. T. Woolley, “Advances in microfluidic materials, functions, integration, and applications,” Chemical Reviews, vol. 113, no. 4. pp. 2550–2583, Apr. 10, 2013. doi: 10.1021/cr300337x.

[15] S. M. Scott and Z. Ali, “Fabrication methods for microfluidic devices: An overview,” Micromachines, vol. 12, no. 3. MDPI AG, Mar. 01, 2021. doi: 10.3390/mi12030319.

[16] C. W. Tsao, “Polymer microfluidics: Simple, low-cost fabrication process bridging academic lab research to commercialized production,” Micromachines, vol. 7, no. 12. MDPI AG, 2016. doi: 10.3390/mi7120225.

[17] J. Friend and L. Yeo, “Fabrication of microfluidic devices using polydimethylsiloxane,” Biomicrofluidics, vol. 4, no. 2, 2010, doi: 10.1063/1.3259624.

[18] B. Wang, Y. Wang, S. Du, J. Zhu, and S. Ma, “Upcycling of thermosetting polymers into high-value materials,” Materials Horizons, vol. 10, no. 1. Royal Society of Chemistry, pp. 41–51, Oct. 26, 2022. doi: 10.1039/d2mh01128j.

[19] X. Li, D. R. Ballerini, and W. Shen, “A perspective on paper-based microfluidics: Current status and future trends,” Biomicrofluidics, vol. 6, no. 1. American Institute of Physics Inc., Mar. 02, 2012. doi: 10.1063/1.3687398.

[20] L. Yu and Z. Z. Shi, “Microfluidic paper-based analytical devices fabricated by low-cost photolithography and embossing of Parafilm®,” Lab Chip, vol. 15, no. 7, pp. 1642–1645, Apr. 2015, doi: 10.1039/c5lc00044k.

[21] H. Asano and Y. Shiraishi, “Development of paper-based microfluidic analytical device for iron assay using photomask printed with 3D printer for fabrication of hydrophilic and hydrophobic zones on paper by photolithography,” Anal Chim Acta, vol. 883, pp. 55–60, Jul. 2015, doi: 10.1016/j.aca.2015.04.014.

[22] C. M. Pandey et al., “Microfluidics Based Point-of-Care Diagnostics,” Biotechnology Journal, vol. 13, no. 1. Wiley-VCH Verlag, Jan. 01, 2018. doi: 10.1002/biot.201700047.

[23] J. H. Nichols, “Utilizing point-of-care testing to optimize patient care.”

[24] M. Sonker, V. Sahore, and A. T. Woolley, “Recent advances in microfluidic sample preparation and separation techniques for molecular biomarker analysis: A critical review,” Analytica Chimica Acta, vol. 986. Elsevier B.V., pp. 1–11, Sep. 15, 2017. doi: 10.1016/j.aca.2017.07.043.

[25] M. Hill and E. Wagenaars, “Modelling of Plasma Temperatures and Densities in Laser Ablation Plumes of Different Metals,” Photonics, vol. 9, no. 12, Dec. 2022, doi: 10.3390/photonics9120937.

[26] J. Shi, Z. Wang, T. Zheng, X. Liu, B. Guo, and J. Xu, “Thermal and UV light adaptive polyurethane elastomers for photolithography-transfer printing of flexible circuits,” Mater Horiz, vol. 9, no. 12, pp. 3070–3077, Oct. 2022, doi: 10.1039/d2mh01005d.

[27] S. Paik et al., “Near-field sub-diffraction photolithography with an elastomeric photomask,” Nat Commun, vol. 11, no. 1, Dec. 2020, doi: 10.1038/s41467-020-14439-1.

[28] J. Wu et al., “Parallel near-field photolithography with metal-coated elastomeric masks,” Langmuir, vol. 31, no. 3, pp. 1210–1217, Jan. 2015, doi: 10.1021/la504260x.

[29] A. Karimi, S. Yazdi, and A. M. Ardekani, “Hydrodynamic mechanisms of cell and particle trapping in microfluidics,” Biomicrofluidics, vol. 7, no. 2, Apr. 2013, doi: 10.1063/1.4799787.

[30] R. Ozawa, H. Iwadate, H. Toyoda, M. Yamada, and M. Seki, “A numbering-up strategy of hydrodynamic microfluidic filters for continuous-flow high-throughput cell sorting,” Lab Chip, vol. 19, no. 10, pp. 1828–1837, May 2019, doi: 10.1039/c9lc00053d.

[31] M. E. Warkiani, A. K. P. Tay, G. Guan, and J. Han, “Membrane-less microfiltration using inertial microfluidics,” Sci Rep, vol. 5, Jul. 2015, doi: 10.1038/srep11018.

[32] N. Herrmann, P. Neubauer, and M. Birkholz, “Spiral microfluidic devices for cell separation and sorting in bioprocesses,” Biomicrofluidics, vol. 13, no. 6. American Institute of Physics Inc., Nov. 01, 2019. doi: 10.1063/1.5125264.

[33] J. Sun et al., “Double spiral microchannel for label-free tumor cell separation and enrichment.,” Lab Chip, vol. 12, no. 20, pp. 3952–3960, 2012, doi: 10.1039/c2lc40679a.

[34] A. Hochstetter et al., “Deterministic Lateral Displacement: Challenges and Perspectives,” ACS Nano, vol. 14, no. 9. American Chemical Society, pp. 10784–10795, Sep. 22, 2020. doi: 10.1021/acsnano.0c05186.

[35] J. McGrath, M. Jimenez, and H. Bridle, “Deterministic lateral displacement for particle separation: A review,” Lab on a Chip, vol. 14, no. 21. Royal Society of Chemistry, pp. 4139–4158, Nov. 07, 2014. doi: 10.1039/c4lc00939h.

[36] T. Salafi, Y. Zhang, and Y. Zhang, “A Review on Deterministic Lateral Displacement for Particle Separation and Detection,” Nano-Micro Letters, vol. 11, no. 1. SpringerOpen, Dec. 01, 2019. doi: 10.1007/s40820-019-0308-7.

[37] K. T. Knizner, R. R. Kibbe, K. P. Garrard, J. R. Nuñez, C. R. Anderton, and D. C. Muddiman, “On the importance of color in mass spectrometry imaging,” Journal of Mass Spectrometry, vol. 57, no. 12, Dec. 2022, doi: 10.1002/jms.4898.

[38] M. F. Wang, A. N. Joignant, A. L. Sohn, K. P. Garrard, and D. C. Muddiman, "Time of acquisition and high spatial resolution mass spectrometry imaging," Journal of Mass Spectrometry, vol. 58, no. 3, Mar. 2023, doi: 10.1002/jms.4911.

[39] M. J. Moore, J. A. Sebastian, and M. C. Kolios, "Determination of cell nucleus-to-cytoplasmic ratio using imaging flow cytometry and a combined ultrasound and photoacoustic technique: a comparison study," J Biomed Opt, vol. 24, no. 10, p. 1, Oct. 2019, doi: 10.1117/1.jbo.24.10.106502.

[40] X. Gao et al., "Piezoelectric Actuators and Motors: Materials, Designs, and Applications," Advanced Materials Technologies, vol. 5, no. 1. Wiley-Blackwell, Jan. 01, 2020. doi: 10.1002/admt.201900716.

[41] A. Aabid, M. Hrairi, S. J. Mohamed Ali, and Y. E. Ibrahim, "Review of Piezoelectric Actuator Applications in Damaged Structures: Challenges and Opportunities," ACS Omega, 2022, doi: 10.1021/acsomega.2c06573.

[42] S. Mohith, A. R. Upadhya, K. P. Navin, S. M. Kulkarni, and M. Rao, "Recent trends in piezoelectric actuators for precision motion and their applications: a review," Smart Materials and Structures, vol. 30, no. 1. IOP Publishing Ltd, Jan. 01, 2021. doi: 10.1088/1361-665X/abc6b9.

[43] K. Chen, H. Lu, M. Sun, L. Zhu, and Y. Cui, "Mixing enhancement of a novel C-SAR microfluidic mixer," Chemical Engineering Research and Design, vol. 132, pp. 338–345, Apr. 2018, doi: 10.1016/j.cherd.2018.01.032.

[44] C. Y. Lee, C. L. Chang, Y. N. Wang, and L. M. Fu, "Microfluidic mixing: A review," International Journal of Molecular Sciences, vol. 12, no. 5. pp. 3263–3287, May 2011. doi: 10.3390/ijms12053263.

[45] F. Jiang, K. S. Drese, S. Hardt, M. Küpper, and F. Schönfeld, “Helical flows and chaotic mixing in curved micro channels,” AIChE Journal, vol. 50, no. 9, pp. 2297–2305, Sep. 2004, doi: 10.1002/aic.10188.

[46] W. S. Low, N. A. Kadri, and W. A. B. Bin Wan Abas, “Computational fluid dynamics modelling of microfluidic channel for dielectrophoretic biomems application,” Scientific World Journal, vol. 2014, 2014, doi: 10.1155/2014/961301.

[47] G. R. Pesch and F. Du, “A review of dielectrophoretic separation and classification of non-biological particles,” Electrophoresis, vol. 42, no. 1–2. Wiley-VCH Verlag, pp. 134–152, Jan. 01, 2021. doi: 10.1002/elps.202000137.

[48] P. E. Thiriet, J. Pezoldt, G. Gambardella, K. Keim, B. Depla, and C. Guiducci, “Selective retrieval of individual cells from microfluidic arrays combining dielectrophoretic force and directed hydrodynamic flow,” Micromachines (Basel), vol. 11, no. 3, Mar. 2020, doi: 10.3390/mi11030322.

[49] H. G. Kye et al., “Dual-neodymium magnet-based microfluidic separation device,” Sci Rep, vol. 9, no. 1, Dec. 2019, doi: 10.1038/s41598-019-45929-y.

[50] A. Munaz, M. J. A. Shiddiky, and N. T. Nguyen, “Recent advances and current challenges in magnetophoresis based micro magnetofluidics,” Biomicrofluidics, vol. 12, no. 3, May 2018, doi: 10.1063/1.5035388.

[51] J. Chung, D. Issadore, A. Ullal, K. Lee, R. Weissleder, and H. Lee, “Rare cell isolation and profiling on a hybrid magnetic/size-sorting chip,” Biomicrofluidics, vol. 7, no. 5, Sep. 2013, doi: 10.1063/1.4821923.

[52] J. Chung, D. Issadore, A. Ullal, K. Lee, R. Weissleder, and H. Lee, “Rare cell isolation and profiling on a hybrid magnetic/size-sorting chip,” Biomicrofluidics, vol. 7, no. 5, Sep. 2013, doi: 10.1063/1.4821923.

[53] M. M. Hoque and M. M. Alam, “Effects of Dean Number and curvature on fluid flow through a curved pipe with magnetic field,” in Procedia Engineering, Elsevier Ltd, 2013, pp. 245–253. doi: 10.1016/j.proeng.2013.03.114.

[54] J. Grant, A. Özkan, C. Oh, G. Mahajan, R. Prantil-Baun, and D. E. Ingber, “Simulating drug concentrations in PDMS microfluidic organ chips,” Lab Chip, vol. 21, no. 18, pp. 3509–3519, Sep. 2021, doi: 10.1039/d1lc00348h.

[55] T. C. Cameron et al., “PDMS Organ-On-Chip Design and Fabrication: Strategies for Improving Fluidic Integration and Chip Robustness of Rapidly Prototyped Microfluidic In Vitro Models,” Micromachines (Basel), vol. 13, no. 10, Oct. 2022, doi: 10.3390/mi13101573.

[56] D. Ahn, L. M. Stevens, K. Zhou, and Z. A. Page, “Rapid High-Resolution Visible Light 3D Printing,” ACS Cent Sci, vol. 6, no. 9, pp. 1555–1563, Sep. 2020, doi: 10.1021/acscentsci.0c00929.

[57] J. Huang, B. Zhang, J. Xiao, and Q. Zhang, “An Approach to Improve the Resolution of DLP 3D Printing by Parallel Mechanism,” Applied Sciences (Switzerland), vol. 12, no. 24, Dec. 2022, doi: 10.3390/app122412905.

[58] J. Zhang, Q. Hu, S. Wang, J. Tao, and M. Gou, “Digital light processing based three-dimensional printing for medical applications,” Int J Bioprint, vol. 6, no. 1, pp. 12–27, 2020, doi: 10.18063/ijb.v6i1.242.

[59] A. Gökaltun, Y. B. (Abraham) Kang, M. L. Yarmush, O. B. Usta, and A. Asatekin, “Simple Surface Modification of Poly(dimethylsiloxane) via Surface Segregating Smart Polymers for Biomicrofluidics,” Sci Rep, vol. 9, no. 1, Dec. 2019, doi: 10.1038/s41598-019-43625-5.

[60] Y. J. Chuah, Y. T. Koh, K. Lim, N. V. Menon, Y. Wu, and Y. Kang, “Simple surface engineering of polydimethylsiloxane with polydopamine for stabilized mesenchymal stem cell adhesion and multipotency,” Sci Rep, vol. 5, Dec. 2015, doi: 10.1038/srep18162.

[61] P. B. Luppa, “Point-of-care testing at the interface of emerging technologies and new clinical applications,” Journal of Laboratory Medicine, vol. 44, no. 2. Walter de Gruyter GmbH, pp. 59–61, Apr. 01, 2020. doi: 10.1515/labmed-2020-0020.

[62] E. Valera et al., “COVID-19 Point-of-Care Diagnostics: Present and Future,” ACS Nano, vol. 15, no. 5. American Chemical Society, pp. 7899–7906, May 25, 2021. doi: 10.1021/acsnano.1c02981.

[63] S. J. Kim et al., “Evaluation of the biocompatibility of a coating material for an implantable bladder volume sensor,” Kaohsiung Journal of Medical Sciences, vol. 28, no. 3, pp. 123–129, Mar. 2012, doi: 10.1016/j.kjms.2011.10.016.

[64] Y. Gou, Y. Jia, P. Wang, and C. Sun, “Progress of inertial microfluidics in principle and application,” Sensors (Switzerland), vol. 18, no. 6. MDPI AG, Jun. 01, 2018. doi: 10.3390/s18061762.

[65] J. Feng, J. Neuzil, A. Manz, C. Iliescu, and P. Neuzil, “Microfluidic trends in drug screening and drug delivery,” TrAC - Trends in Analytical Chemistry, vol. 158. Elsevier B.V., Jan. 01, 2023. doi: 10.1016/j.trac.2022.116821.

[66] M. I. Khot et al., “Characterising a PDMS based 3D cell culturing microfluidic platform for screening chemotherapeutic drug cytotoxic activity,” Sci Rep, vol. 10, no. 1, Dec. 2020, doi: 10.1038/s41598-020-72952-1.

[67] S. J. Streichan, C. R. Hoerner, T. Schneidt, D. Holzer, and L. Hufnagel, “Spatial constraints control cell proliferation in tissues,” Proc Natl Acad Sci U S A, vol. 111, no. 15, pp. 5586–5591, Apr. 2014, doi: 10.1073/pnas.1323016111.

[68] E. Amstad, “Capsules: Their past and opportunities for their future,” ACS Macro Lett, vol. 6, no. 8, pp. 841–847, Aug. 2017, doi: 10.1021/acsmacrolett.7b00472.

[69] A. Le Goff, B. Kaoui, G. Kurzawa, B. Haszon, and A. V. Salsac, “Squeezing bio-capsules into a constriction: Deformation till break-up,” Soft Matter, vol. 13, no. 41, pp. 7644–7648, 2017, doi: 10.1039/c7sm01417a.

[70] Z. Y. Luo and B. F. Bai, “Off-center motion of a trapped elastic capsule in a microfluidic channel with a narrow constriction,” Soft Matter, vol. 13, no. 44, pp. 8281–8292, 2017, doi: 10.1039/c7sm01425b.

[71] S. S. Deville and N. Cordes, “The Extracellular, Cellular, and Nuclear Stiffness, a Trinity in the Cancer Resistome—A Review,” Frontiers in Oncology, vol. 9. Frontiers Media S.A., Dec. 06, 2019. doi: 10.3389/fonc.2019.01376.

[72] G. Wang, K. Crawford, C. Turbyfield, W. Lam, A. Alexeev, and T. Sulchek, “Microfluidic cellular enrichment and separation through differences in viscoelastic deformation,” Lab Chip, vol. 15, no. 2, pp. 532–540, Jan. 2015, doi: 10.1039/c4lc01150c.

[73] K. G. Phillips et al., “Optical quantification of cellular mass, volume, and density of circulating tumor cells identified in an ovarian cancer patient,” Front Oncol, vol. 2 JUL, 2012, doi: 10.3389/fonc.2012.00072.

[74] K. J. Regehr et al., “Biological implications of polydimethylsiloxane-based microfluidic cell culture,” Lab on a Chip, vol. 9, no. 15. Royal Society of Chemistry, pp. 2132–2139, 2009. doi: 10.1039/b903043c.

[75] S. Chow, D. Hedley, P. Grom, R. Magari, J. W. Jacobberger, and T. V. Shankey, “Whole blood fixation and permeabilization protocol with red blood cell lysis for flow cytometry of intracellular phosphorylated epitopes in leukocyte subpopulations,” Cytometry Part A, vol. 67, no. 1, pp. 4–17, Sep. 2005, doi: 10.1002/cyto.a.20167.

[76] A. Reece, B. Xia, Z. Jiang, B. Noren, R. McBride, and J. Oakey, “Microfluidic techniques for high throughput single cell analysis,” Current Opinion in Biotechnology, vol. 40. Elsevier Ltd, pp. 90–96, Aug. 01, 2016. doi: 10.1016/j.copbio.2016.02.015.

Chapter 2 Microfluidic cell isolation device with unique design of clog-free and high throughput features for cancer cell trapping.

2.1 Abstract

From liquid biopsies, microfluidics has been used to filter out rare tumor cells from blood. Low flow rates and device clogs brought on by a single fluidic path function severely restrict processing. A novel technique was created employing multifunctional hybrid microposts. To avoid highly frequent congestion issues, a quick by-passing channel for non-tumor cells was included. Microbeads (10 μm) and human cancer cells spiked in human blood were used to measure performance. At a flow rate of 1 ml/min, Design-I demonstrated capture efficiencies of 96% for microbeads and 87% for cancer cells. With a greater capture effectiveness of 100% for microbeads and 96% for cancer cells, an enhanced Design-II was demonstrated. Our technique, which makes use of a variety of microfluidic separation, bypass, and capture capabilities, has effectively ensured the highly effective separation of rare cells from biological fluids.

2.2 Introduction

Microfluidics-based systems have recently been extensively incorporated into many different research fields. One might think of advanced cellular research for biomedical and healthcare applications, the use of microreactors for chemical synthesis, and the

application of microfluidic technology for proteomic analysis in samples with low protein concentration. Biomedical microfluidic platforms have moved to point-of-care diagnostic and prognostic levels thanks to significant research achievements3. Effectively capturing and retrieving viable cells for liquid biopsy investigations (such as testing the drug sensitivity of rare circulating tumor cells (CTCs) from cancer patients' blood) while maintaining a high flow rate and clog-free device features is a need in particle-based biomedical research that has not yet been fully satisfied. Rare CTCs [51], [52], [77]–[79] are frequently isolated from a large number of other blood cells via label-based capture that relies on biomarker expression. However, the inconsistent and varied cellular biomarker expression in tumor cells limits the specificity of current label-based enrichment techniques. There have been active efforts to create microfluidic platforms for label-free [33], [78], [80], [81] cell separation using inherent physical features in order to address these difficulties (e.g., size, mass, electrical charge). There are numerous microfluidic methods that use size-based enrichment in biomedicine, including membrane microfiltration [82], [83], pinched flow fractionation [79], [84], deterministic lateral displacement, and Hydrophoresis [85], [86]. The effective extraction of rare cells in a viable state from a variety of media, such as aerosols, blood, or other bodily fluids, is another significant problem. Fluidic sorting techniques have been suggested to improve these cell isolations' selectivity, specificity, sensitivity, reproducibility, and processing speed. Yet, a particular approach hasn't yet been able to meet all the above stated requirements. Separation techniques can be broadly categorized as active, or passive based on the actuation and control mechanism principles. External forces are frequently used in active methods to accomplish high-resolution particle separation, necessitating a

particle's special physical characteristic. Electrophoresis, magnetophoresis [50], negative magnetophoresis, optical manipulations, and thermal manipulations are the major active approaches in active separation techniques. In order to generate significant external forces for separation based on intrinsic features, they often require high-power energy consumption. The features of the flow in the microfluidic channel determine passive separations, in contrast. Significant benefits include the platform's simplicity in construction, independence from outside pressures, and minimal energy usage during processing. Hydrodynamic filtration, inertial lift [82], [83], [87], deterministic lateral displacement, Dean's flow [88], and pinched flow fractionalization [84] are some of the examples of passive separation techniques now in use. The majority of investigations using microfluidic devices have shown that extremely low flow rates (0.05 ml/min) are required to maintain an acceptable degree of capture efficiency, however these results are lengthy and impractical processing durations. Also, there is a dearth of systematic study aimed at imposing different configurations and shapes of the micropost structures that can creatively address issues. To improve particle collecting, equilateral triangular and cylindrical microposts were used. The first row of the array's microposts, however, become actively involved in particle collecting during the filtering process, which causes substantial clogging [89], [90] that ultimately stops the flow and destroys the sample. The Figure 2-1 shows commonly available microfluidic device design which suffers from clogging issues.

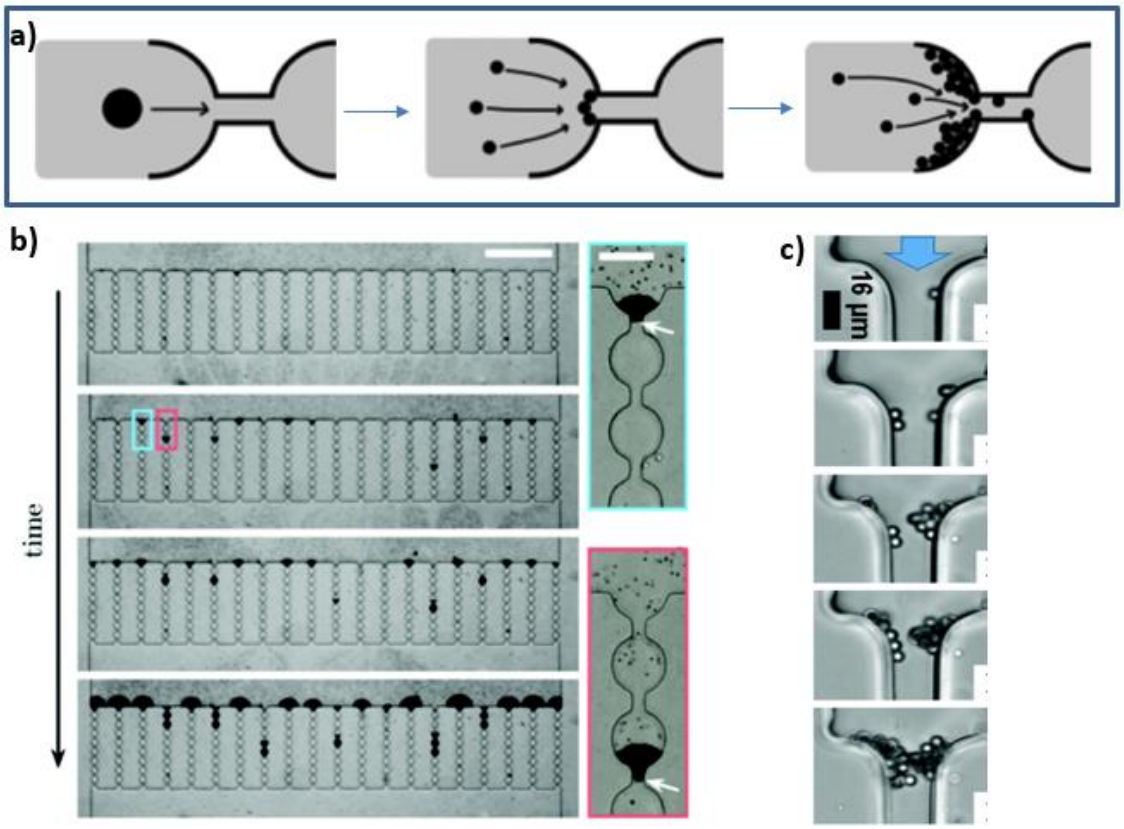

Figure 2-1. Clogging in commonly used Microfluidic devices.

In this article, we offer a cutting-edge microfluidic platform that combines a variety of specially created multiconceptive multifunctional microposts with a goal of achieving extremely high capture efficiencies and flow rates without the presence of harmful clogging issues. In particular, a different carry-forward approach is used, which enables particles to easily avoid a congested location. Such a bypassing zone Figure 2-2 appears to be particularly successful at relieving the unwanted effects of surge pressure buildup caused by blockage and preventing the production of shear stress, which has been shown to have a detrimental effect on cell viability [91], [92]. Preventative measures against blockage and effective cell capture were favorably obtained by altering geometric effects of the device's microposts. We were able to successfully demonstrate a novel high-

throughput microfluidic isolation method for rare blood cells by utilizing several strategies.

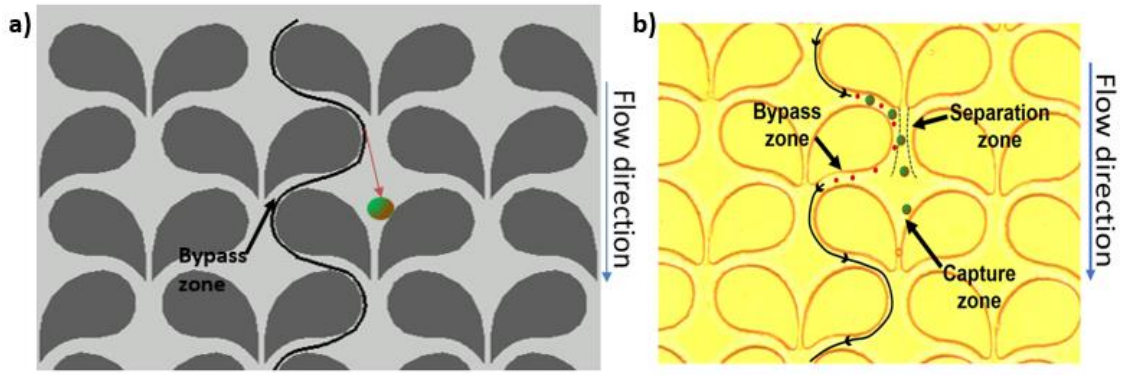

Figure 2-2. The concept of Bypass flow is to avoid clogging issues. a). Design overview. b). Microscopic image of the device.

2.3 Materials and Methods

2.3.1 Microfluidic device fabrication

Using a silicon substrate, the microfluidic device was fabricated using conventional soft-lithography methods and an SU8 master mold. The silicon wafer that will serve as the master mold for the polymeric filter device was prepared using the negative photoresist SU8-3025 from Micro Chem®, Bound Rock, Texas. The usual photolithography procedures were used. The ideal microfluidic channel height was found to be 30 µm ±2 µm after considering various criteria (such as operation flow rates and typical cell sizes). Dow Corning Inc. Midland, Michigan's Sylgard™ 184 elastomer polydimethylsiloxane (PDMS) and its curing agent were mixed in the specified proportions, degassed to remove air pockets, and then applied to the silicon master inside the Petri dish. Curing of PDMS layer took place at 75° C for about three hours. A clean microscopic glass slide

(1" x 3") and the surface of the PDMS containing the microposts were then oxygen plasma-treated in plasma Asher instrument Figure 2-3 at 70 W for 50 sec, and then they were fused while making sure there were no air pockets inside the bonding layers. The structural formula of PDMS and Glass slide before and after bonding are shown in Figure 2-4. To create greater adhesion, the bonded device was heated to 80 °C for 15 minutes. A 0.6 mm Tungsten Carbide Drill Bit was used to drill the intake and outflow ports on the PDMS, and then PTFE tubes were bonded to the ports.

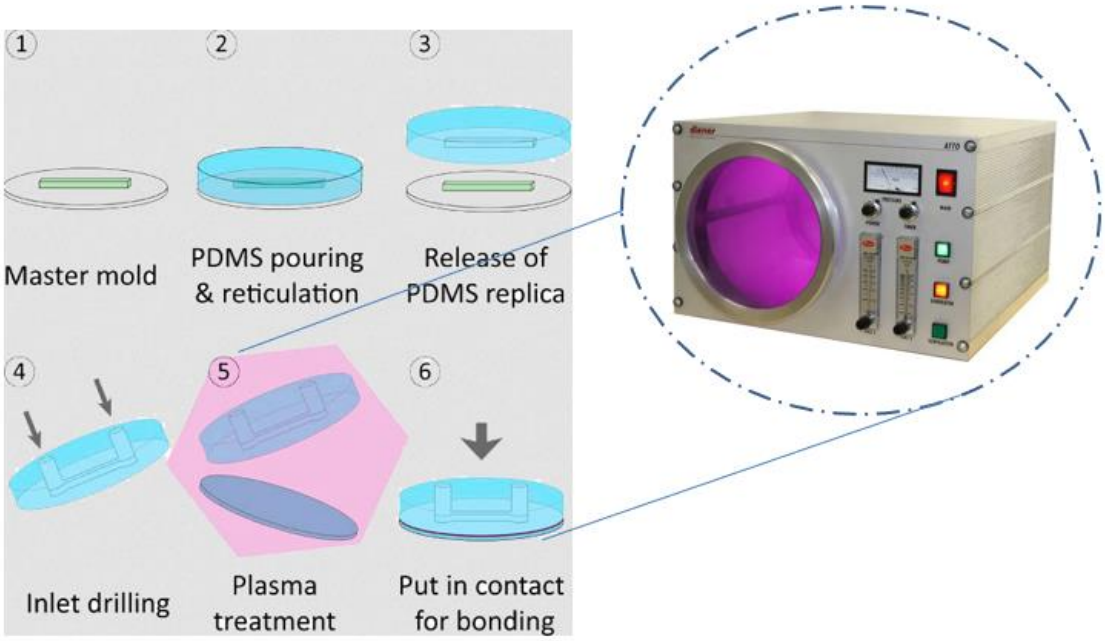

Figure 2-3. Steps involved in PDMS device fabrication using plasma Asher to activate the surface of PDMS.

2.3.2 Computational analysis of the flow profile in the microdevice

The velocity profiles inside the device were computationally simulated using COMSOL Multiphysics® version 5.3a finite element analysis software (COMSOL Inc., Burlington,

MA), as shown in Figure 2-12. By joining two partial circles with radius of curvatures of 70 mm and 38 mm, respectively, the asymmetrical geometry of Design-I was created. Using the COMSOL software, numerical analysis was done to determine the ideal operating circumstances and design for the microposts with wing-like geometry. The fluidic medium under the test was operated under conditions similar to that of water, including incompressible flow, an inlet linear velocity of 2 mm/sec, no-slip boundary conditions for all walls, and zero outlet pressure.

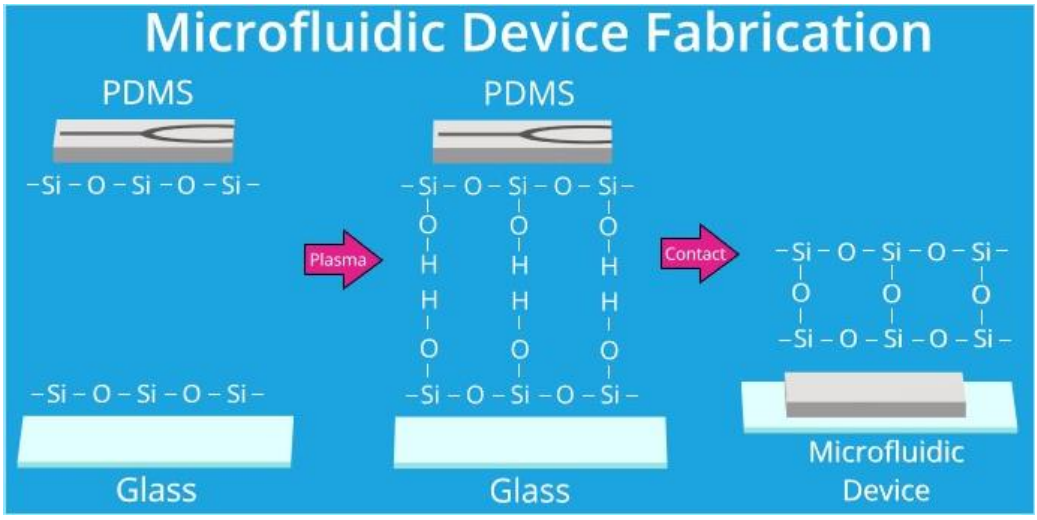

Figure 2-4. PDMS structural formula changes during plasma Asher bonding

2.3.3 Platform design

The platform was created using the AutoCAD® (Autodesk, Inc., San Rafael, CA) program and has 506 rows and 54 columns, a total of 27324 post pairs, and one trapping site for each pair of posts. The chip has a 45 mm by 15 mm filter area and a 30 m height, which is encapsulated inside a boundary of 1" x 3". The geometry for Design I Figure 2-5.a was created by joining two half circles, with respective radii of 37 m and 90 m. Subsequently, to construct Design II Figure 2-5.b, with higher capture effectiveness, the

smooth curve was lengthened and contoured downward to steer itself towards the subsequent trapping region.

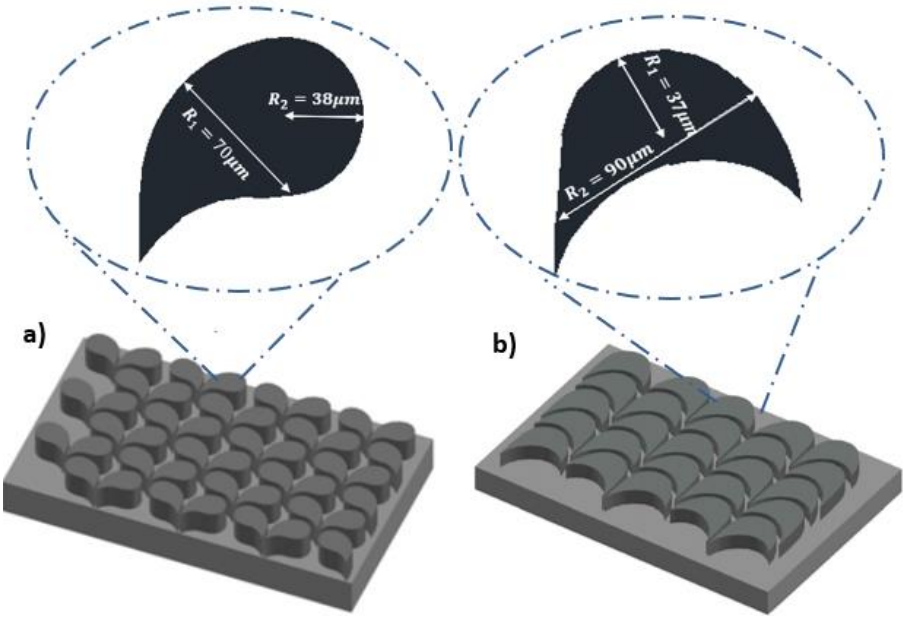

Figure 2-5. AutoCAD Drawing of a). Design I and b). Design II

2.3.4 Device characterization for flowrate optimization using microbeads and human cancer cells.

FluoSpheres™ Polystyrene Microbeads (10 µm) suspended in phosphate-buffered saline (PBS) (Cat#: 14190250; Thermo-Fisher Scientific) Figure 2-6.a were used to optimize the flowrate of the microfluidic platform. One hundred microbeads were picked up one at a time with a micropipette and injected into 4 ml of PBS buffer for each test. The device's inlet port was used to introduce the suspension of microbeads. Bright-field microscopy was used to count the microbeads that the apparatus had managed to catch Figure 2-6.b,c. The ratio of microbeads collected in the device to all microbeads in the input sample was used to compute capture efficiency (%). For each flow rate, spiking

experiments were run five times. Nine different flow rates, ranging from 0.25 ml/min to 3.0 ml/min, were tested.

Human lung cancer cell lines A549 (ATCC® CCL-185TM, ATCC, Manassas, VA) were employed for biological device testing. Cancer cell lines and CTCs have been shown to have diameters more than 10 μm. While CTCs are larger than the bulk of other cells (such as leukocytes and red blood cells (RBCs)), this size difference can be used to enrich them based on size. In DMEM media (Cat#: 11965118; Thermo-Fisher Scientific) with 10% fetal bovine serum and 1% penicillin-streptomycin (Cat#: 15140122; Thermo-Fisher Scientific), A549 human cancer cells were kept alive. Cancer cells were grown to a confluence level of about 80% for device testing. 0.05% Trypsin-EDTA (Cat#: 25300120; Thermo-Fisher Scientific) was used to collect the cells. One hundred cancer cells were individually selected for each test and spiked into 4 ml of PBS buffer using a micropipette. Then, the device's intake port was used to introduce the suspension of cancer cells. Using bright-field microscopy, the device's cancer cells were counted. The ratio of cancer cells trapped in the device to all cancer cells in the input sample was used to compute the capture efficiency (%). For each flow rate, spiking experiments were run five times. Nine different flow rates, ranging from 0.25 ml/min to 3.0 ml/min, were tested.

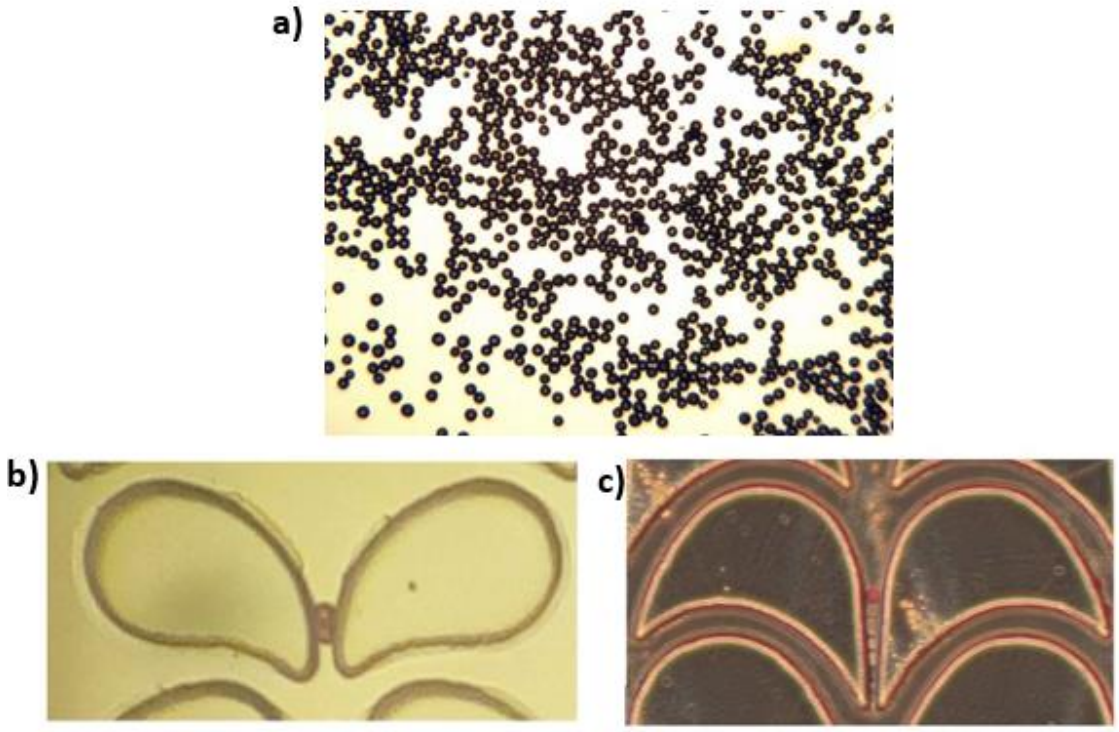

Figure 2-6. Microbeads as an initial testing particle a). Microbeads 10μm diameter particles under the microscope. Trapped Microbeads in b). Design I. c). Design II

2.3.5 Pre-clinical testing using human cancer cells spiked in human blood.

The University of Missouri Institutional Review Board approved the study methodology that included using human blood samples (MU IRB clearance number: 2010166). Prior to taking blood samples, written informed consent was obtained. Blood samples were then taken, transported, and stored for future investigations in compliance with the Helsinki Declaration. Healthy volunteers' whole blood was collected into K2EDTA vacutainer tubes. Cell line A549 Figure 2-7.a, a known quantity of human lung cancer cells, was spiked into the anti-coagulated whole blood. This blood mixture was injected through the device's inlet port. Using bright-field microscopy, the device's trapped cancer cells Figure 2-7.b,c were counted. Before being spiked, A549 cells were formalin-fixed,

permeabilized, and labeled with DAPI to ensure that the cells being trapped are in fact spiked cells. Blood samples spiked with A549 and PBMCs (mononuclear fraction of white blood cells) were processed separately using the device to assess the differential capture efficiencies of cancer cells and WBCs (White Blood Cells).

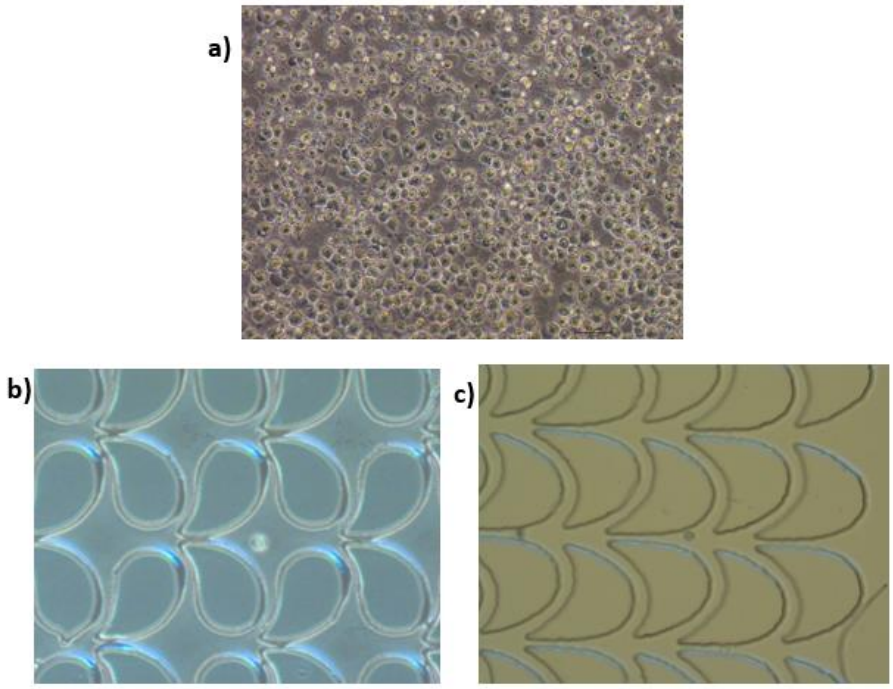

Figure 2-7. A549 cancer cell as a testing particle a). A549 cancer cell particles visualized under the microscope. Trapped A549 cancer cell in b). Design I. c). Design II

2.3.6 Isolation and labeling of PBMCs from healthy human blood.

In K2EDTA tubes, whole blood (10 ml) from a healthy donor was drawn. After carefully layering anticoagulated blood on top of the Ficoll-Paque® Plus reagent, anticoagulated blood was diluted (1:1) with PBS and subjected to density-gradient centrifugation at 2000 rpm for 20 min at room temperature without breaks. A final cell suspension of 1 X 10^6 cells/ml was made in serum-free DMEM media from PBMCs that were extracted and

counted during the interphase between the upper plasma phase and lower Ficoll phase. PBMCs were labeled by 30 min of incubation at 37 °C with 2 M CellTracker Green CMFDA dye (C2925; Thermo-Fisher). For device testing, labeled PBMCs (1 X 10^6) and DAPI-stained A549 cells (100 cells) were spiked into fresh whole blood.

2.4 Theory

2.4.1 Flow Patterns in Microfluidic channel

2.4.1.1 Laminar Flow

The movement of fluid particles along clearly defined routes, or streamlines (gas or liquid), where every streamline is straight and parallel, is known as laminar flow [84], [93]–[95]. As a result, the particles move in layers or laminar motion, easily sliding over one another. Adjacent layers tend to glide past one another like playing cards at low velocities since the fluid tends to move without lateral mixing. There are no eddies, swirls, or cross currents that run parallel to the flow direction. In laminar flow, fluid particles move in a very ordered manner, Figure 2-8.a travelling in straight lines parallel to a solid surface when they are close to it. Small diameter pipes with high viscosity fluid and slower flow rates exhibit laminar flow. Other names for this sort of flow are streamline flow and viscous flow. Laminar flow is typically illustrated by the flow of oil through a thin tube, the flow of blood through capillaries, and the straight up rise of smoke from an incense stick. Yet as it eddies off its usual course, the smoke rises to a modest height and then transforms into the turbulent flow.

2.4.1.2 Turbulent flow

The definition of turbulent flow is a flow in which the fluid particles travel in a zigzag pattern Figure 2-8.b. Turbulence, also known as turbulent flow [93], [96], is a fluid motion in fluid dynamics characterized by erratic fluctuations in flow velocity and pressure. Eddies arise as a result of the zigzag motion of fluid particles, which results in a significant loss of energy. The amplitude and direction of the fluid's speed at a given spot are continuously changing in turbulent flow. In large diameter pipes with rapid fluid flow, turbulent flow is more likely to develop. Laminar flow will have a parabolic shape to the velocity distribution at cross sections, with the maximum velocity in the center being around double the average velocity in the pipe [53], [95]. Due to the enhanced momentum transfer to the walls in turbulent flow, the velocity distribution across the pipe section is relatively flat.

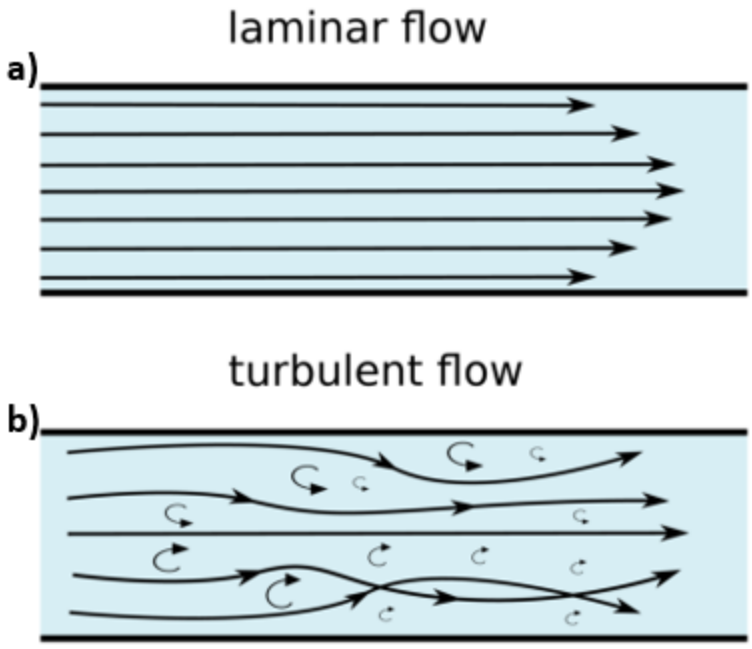

Figure 2-8. Velocity profile of the liquid when it is a). Laminar flow. b). Turbulent flow

2.4.2 Dean and Reynolds Number

Both Dean number and Reynolds number are standard mathematical basis for understanding laminar and turbulent flow in a microchannel. This helps predict the flow patterns and manipulate the geometry to obtain the required velocity profiles.

2.4.2.1 Dean Number

While studying flow in curved pipes and channels, fluid mechanics encounter the dimensionless group known as the Dean number (D_e) [53], [88], [97], [98]. It is so named in honor of the British scientist W. R. Dean, who was the first to offer a theoretical explanation of fluid motion via curved pipes for laminar flow using a perturbation process from a Poiseuille flow in a straight pipe to a flow in a pipe with a very slight curvature. The centripetal forces at a bend in a straight pipe that is carrying a fluid will

cause the fluid's particles to alter their primary direction of travel. An unfavorable pressure gradient caused by the pipe's curvature will result in an increase in pressure and a decrease in velocity near to the convex wall, while the opposite will happen on the pipe's outer side. This causes a secondary flow Figure 2-9 to be superimposed on the primary flow [99], [100], with the fluid near the pipe wall returning to the inside of the bend while the fluid in the middle of the pipe is swept towards the outside of the bend. The Dean number for a rectangular channel can be represented as follows.

$$D_e = R_e . \sqrt{\frac{D_h}{R}}$$

The Dean number (D_e) is a function of the Reynolds number (R_e), the hydraulic diameter (D_h) for a rectangular channel, and the radius of curvature (R). The Dean number (D_e) is directly proportional to the Reynolds number (R_e) and inversely proportional to the square root of the radius of the curvature (R). A change in these parameters alters the intensity of secondary flow in the microfluidic channel.

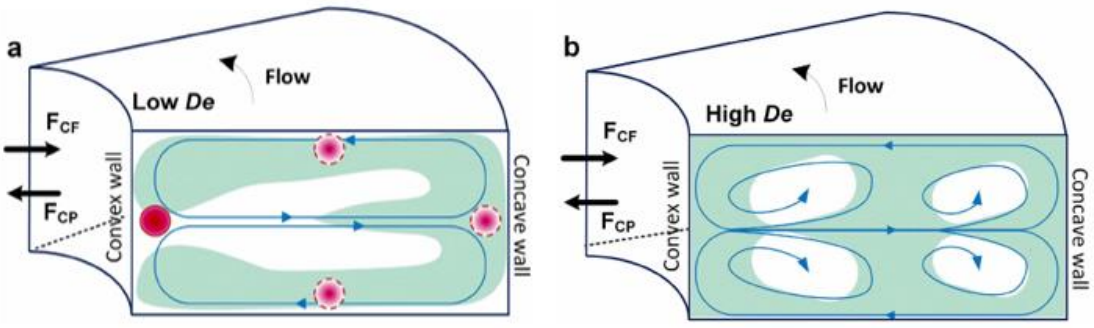

Figure 2-9. Flow pattern relation with Dean number and the fluid wall

2.4.2.2 Reynolds Number

By measuring the proportion of inertial and viscous forces, the Reynolds number (R_e), a dimensionless quantity in fluid mechanics, aids in the prediction of fluid flow patterns in many contexts [96], [101]. Laminar (sheet-like) flow typically predominates in flows with low Reynolds numbers, whereas turbulent flow typically predominates in flows with high Reynolds numbers. Differences in the fluid's speed and direction, which might occasionally intersect or even travel against the general direction of the flow, cause turbulence (eddy currents). The Reynolds number for a rectangular channel is given as follows:

$$R_e = \frac{\mathrm{L}.V_{avg}.\rho}{\mu}$$

The Reynolds number is proportional to characteristic length (L), fluid average velocity (V_{avg}), Fluid density (ρ) and inversely proportional to Viscosity of the fluid used (μ). Experimental findings for flow in a pipe with diameter D reveal that laminar flow occurs when R_e <2300 and turbulent flow occurs when R_e > 4000. Intermittent flow [93] is the term for the change of the flow between laminar to turbulent and then back to laminar at irregular intervals. The Reynolds number R_e is between 2300 and 4000 for Intermittent flow to appear. This is a result of the fluid moving at various rates and under various conditions based on the pipe's cross section and other variables like flow homogeneity and pipe roughness and many other factors.

2.5 Results and Discussion

Our novel design of microposts with numerous crucial functions made our microfluidic isolation technology possible. Each micropost had a unique wing-like configuration in pairs Figure 2-11.a,b, was put in separate orientations, and had precise but irregularly curved geometry. In many areas of the micropost, bypassing, separating, and capturing functions were successfully accomplished. Each component worked together to ensure high capture efficiency while resolving common issues with previous microfluidic technologies, such as low flow rates and clogging. Several crucial aspects of the performance, including repeatability, dependability, and varying flow rates with microbeads and human cancer cells, were assessed under varied operating settings. The inertial migration of microparticles passing through a curved microchannel is used in the separation zone. According to W. R. Dean, the fluidic flow around a curvature creates helical streamlines in a curved microchannel. The secondary flow path, or these helical streamlines, are veering off from the main flow and away from the curved micropost walls Figure 2-9. In comparison to the primary flow, the secondary flow is comparatively insignificant. The secondary flow can be used to separate and capture larger particles by directing them to the isolation zone within the capture site because it depends on both the radius of the curved path and the size of the particle Figure 2-10. By adjusting these variables, we were able to create a micropost with a large enough Dean number (D_e) to produce a strong secondary flow that would help particles travel around the micropost. The device with the micropost arrangement within the device with a 7 µm gap at the capture site and an additional 14 m by-passing channel is shown in Figure 2-10.c. Asymmetrical flow comes from this unique architecture. The rotation-induced lift force

(F), a byproduct of secondary flow, can be used to explain how particles travel around these high aspect ratios (h/w) of the microfluidic channel. The particles first travel towards the sidewalls of the microposts due to shear-induced lift force (FS). The particles are then pushed away from the walls by the rotation-induced lift force (FR), and an equilibrium is reached along the long, curved surfaces of the micropost. The rotation-induced lift force (FR), which is primarily generated by our distinctive wing-like micropost design, propels bigger particles away from the micropost's walls and into the capture site. A particle's diameter must be greater than 72% of the channel depth in order for it to be considered big enough to feel this force. Moreover, as seen in Figure 2-10, tiny particles with diameters lower than 27% of the channel depth won't exert enough force to be steered toward the capture location.

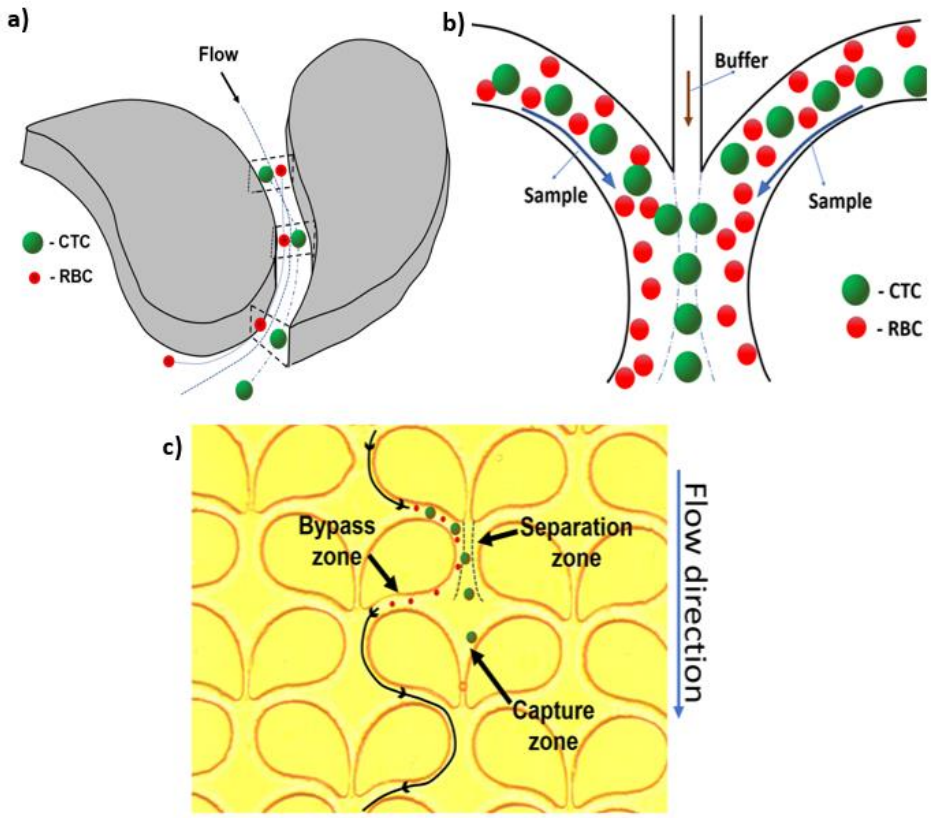

Figure 2-10. Flow around the microposts showing the trajectory of small and large particles.

The non-symmetric micropost is surrounded by a flow pattern that is unequal on both sides due to the separation of the bypass zone and the capture zone. As shown in Figure 2-10, the capture zone is a 7 µm gap where the cell is trapped after being guided by the separation zone. Transporting smaller particles, like RBCs, and isolating individual cells are the bypass zone's two key benefits. The former is achieved because smaller particles did not exert enough force to be directed towards the capture zone, whereas the latter is accomplished when a cell is trapped at the capture zone, preventing flow through the 7 µm zone and around that region, aiding in the redirection of new larger particles through the bypass route towards the next available empty capture zone and eradicating the clogging problem seen in other microfluidic technologies. COMSOL software was used to conduct finite element analysis to determine the ideal operating circumstances and design for the microposts with wing-like geometry Figure 2-12.a,c. The fluidic medium's operational conditions, which included incompressible flow, an inlet linear velocity of 12 mm/sec, no-slip boundary conditions for all walls, and an output pressure of zero, were comparable to those of water. The distribution of particles was based on normal distribution principle which mimics the real case scenarios. High velocity was seen above the capture point, which helped to successfully direct the laterally displaced particle there. To find the fluidic pattern around the microposts and at the capture zone with a trapped particle, both variations of the microposts designs were simulated using these parameters in COMSOL Software Figure 2-12. The trapping zone with a trapped particle has lowest velocity Figure 2-12.b,d indicating that the trapped particles are undisturbed by the incoming samples.

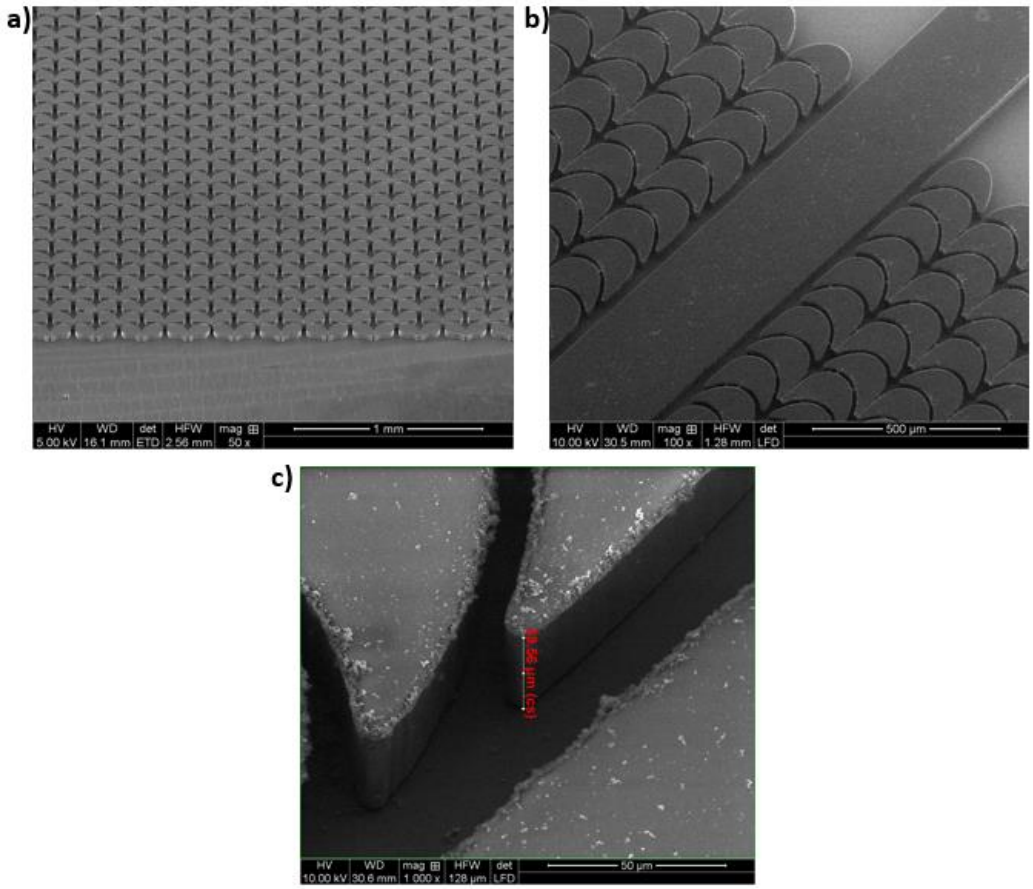

Figure 2-11. SEM image of the device designs. a). Design I b). Design II and c). Zoomed image of one of the wings of Design II

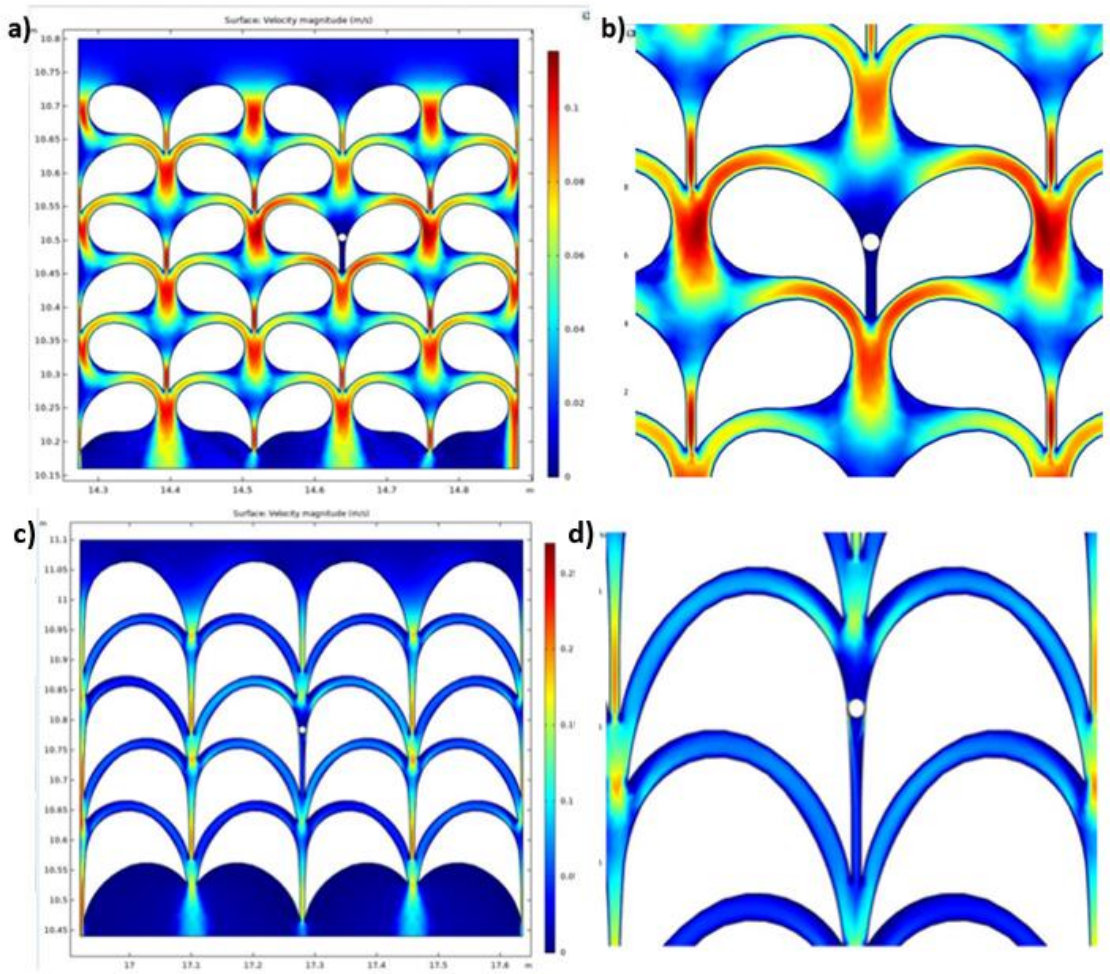

Figure 2-12. COMSOL velocity profiles of Design I and II

2.5.1 Testing performed using microbeads in PBS fluid medium.

With the use of microbeads, the capture effectiveness of our prototype (Design-I) and upgraded (Design-II) microfluidic devices were examined. For a consistent evaluation of the microfluidic isolation method, microbeads a uniform-sized particles not affected by shear stress are frequently used. At a flow rate of up to 0.5 ml/min, which is already quite high to be suitable for biomedical and clinical applications, a maximum capture efficiency of 100% was observed using microbeads in Design-I. (Figure 2-13.a). At or

above a flow rate of 0.75 ml/min, we saw a considerable decline in the capture efficiency. Crucially, throughout all the tests, there was no clogging observed inside the device. Even though Design-I showed great throughput metrics, an effort was made to boost its capture effectiveness by changing the size, geometry, and placement of the microposts. Using microbeads, this upgraded Design-II demonstrated better performance by attaining 100% capture efficiency at a flow rate of 1 ml/min (Figure 2-13.b). Moreover, in testing with higher flow rates, the device's and the microposts' integrity were also steadfastly maintained, suggesting resilience under various operational circumstances.

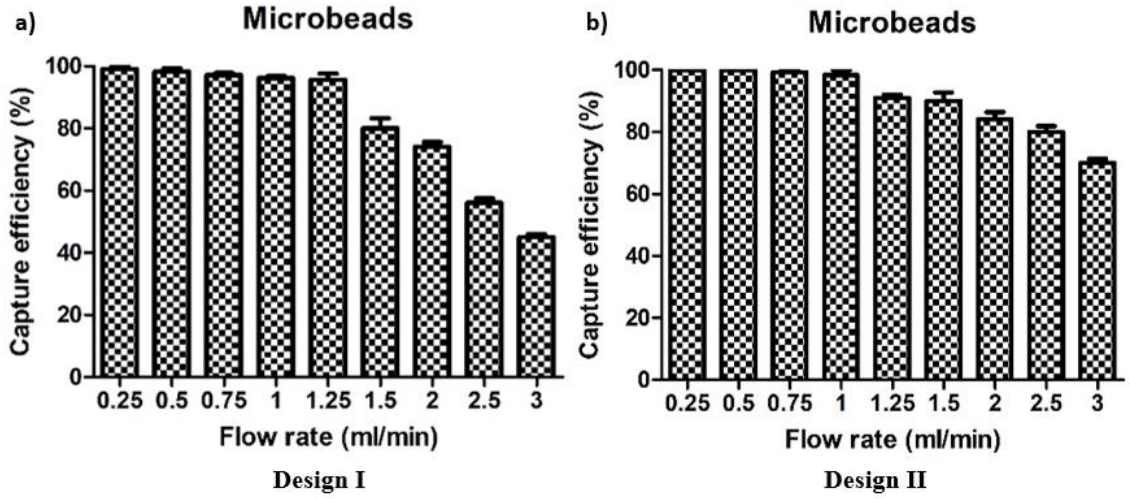

Figure 2-13. Microbeads Capture efficiencies for a). Design-I and b). Design-II.

2.5.2 Testing performed using human cancer cells in PBS fluid medium.

Cells have diverse and varying sizes, shapes, dynamics, densities, and demonstrate plasticity under physiological settings, as opposed to stable, fixed-size microbeads. Due to shear stress caused by fluid movement within the device, cells are vulnerable to injury and loss of integrity due to their biological characteristics. 87% of human cancer cells were successfully captured by Design-I at 1 ml/min (Figure 2-14.a). When compared to

conventional microfluidic methods, a flow rate of 0.5 ml/min maintained a sufficiently high capture efficiency. While traveling through the device, captured cancer cells showed signs of maintaining their integrity, including their outer membranes, cytoplasm, and nuclei, despite their susceptibility to being damaged. Using human cancer cells, the enhanced version Design-II was carried out with a capture effectiveness of 96% at a flow rate of up to 1 ml/min, in agreement with the geometrical design's theoretical aspect (Figure 2-14.b). The specific adjustments made to the geometric shape of the microposts are evident in the results, which show that Design-II has a better microfluidic profile than Design-I. It's noteworthy that the adjustments made to the microposts for Design-II kept the high throughput and clog-free qualities while preserving the integrity of the microstructural device and the survivability of microscopic cancer cells.

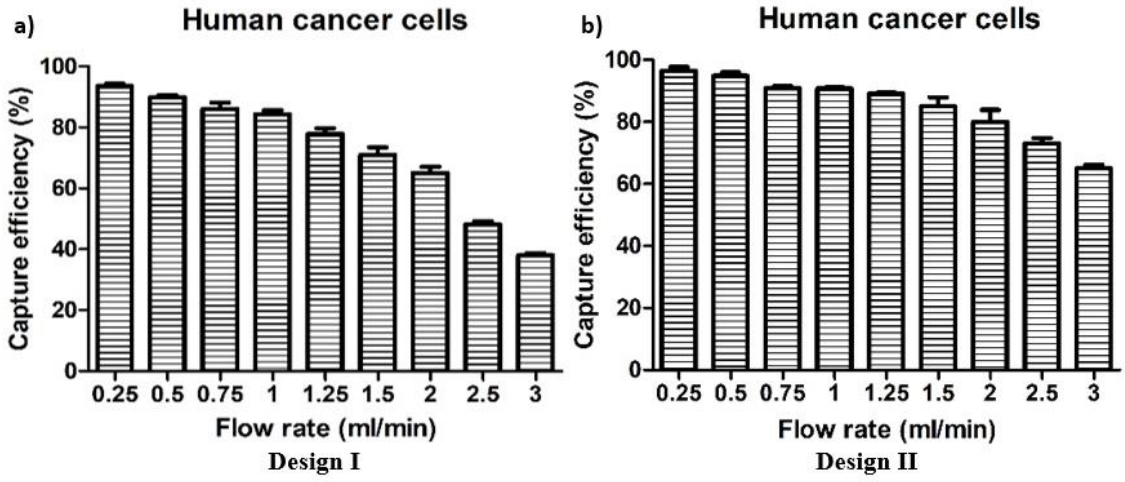

Figure 2-14. Human cancer cell Capture efficiencies for a). Design-I and b). Design-II.

2.5.3 Capture efficiency of both designs in the pre-clinical setting

In capturing human cancer cells spiked in the buffer solution, both designs worked effectively. We evaluated both Design-I and -II with healthy human blood as the final

fluid medium, however, to strengthen the basis for our method's prospective uses in actual biological and clinical situations. To provide workable and practical fluidic conditions in the device, healthy human blood diluted in a ratio of 1:5 (Blood: PBS) with a viscosity of between $3.5x10^{-3}$ and $5.5x10^{-3}$ Pa.s was used. Due to their high density in numbers (4.1 to 5.1 million/mm^3), only a tiny fraction of RBCs was trapped within the device, despite the fact that the majority of RBCs were infused with the sample. As anticipated, the small percentage of RBCs that were maintained in the device had no effect on the fluidic flow or complicated the microscopic counting of cancer cells. Before to spiking, cancer cells were frozen, permeabilized, and nuclear stained with 4',6' diamidino-2-phenylindole (DAPI) to enable identification using fluorescence microscopy in order to separate human cancer cells from the abundance of white blood cells (WBCs). With either diluted blood or PBS, each data bar in the graphs represents five replicate tests, and Figure 2-16 compares the effectiveness of the two strategies. The experimental results with human blood were quite similar to the data with PBS buffer, despite there being more variability as indicated by the range of the standard error of the means. This demonstrates the innovative microfluidic device design's potential relevance in clinical and biomedical settings where human blood is involved.

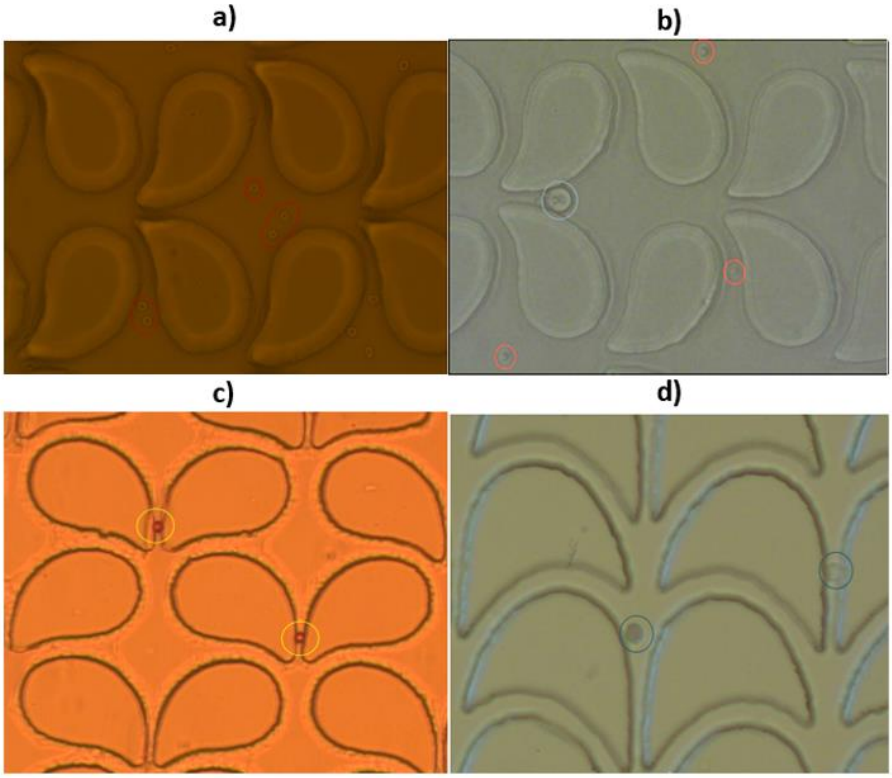

Figure 2-15. Particle size comparison in the device

Figure 2-15 shows the various particles that could come into contact with the device during testing. We have already discussed the sizes of microbeads and cancer cells and RBCs, but to give a quantitative look of the size, the particles are circled as follows. All the microbeads are which are ~10μm in size are shown ion yellow circles in Figure 2-15.c. In Figure 2-15.b both cancer cells (Blue circles) and RBCs (Red circles) are visible.

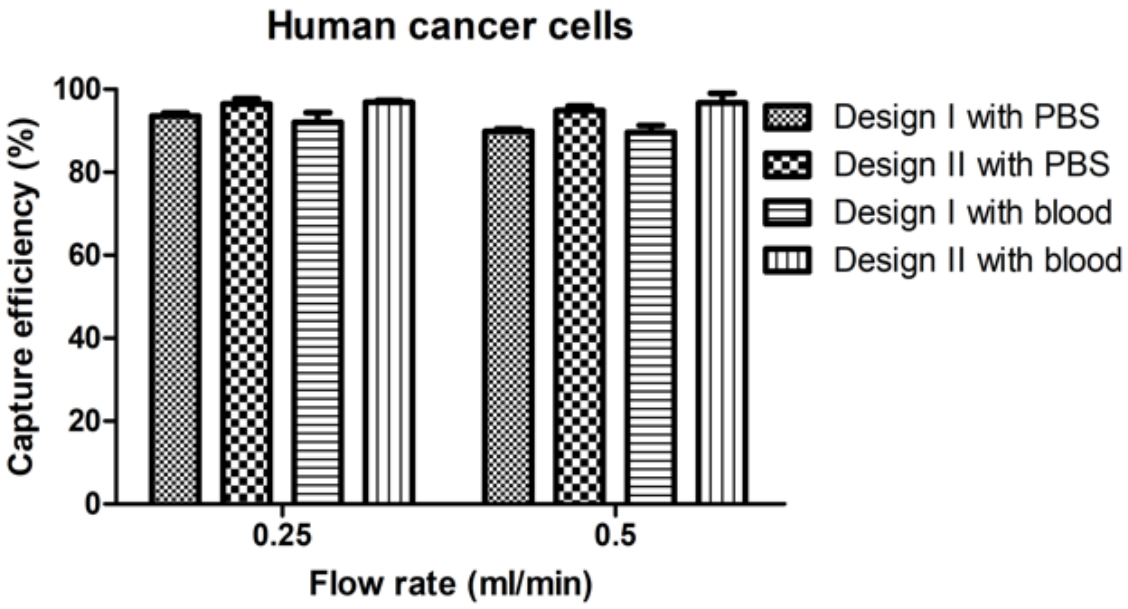

Figure 2-16. Human cancer cell Capture efficiencies with blood and PBS as fluid medium for Design-I and Design-II.

2.5.4 Leukocyte filtration through the device

The nucleus size of each type of leukocyte is listed in Table 2-1 together with their cytoplasmic ratios, which shows that the nucleus size is less than 7 μm, allowing them to easily fit through the trapping region. A few experiments were done to compare the number of leukocytes trapped in the device to an approximation of their presence in human blood injected through the device (1:5 dilution). In blood that is in good health, WBC concentrations range from $4.5x10^6$ to $11x10^6$ per mL. However, we found that when fluorescently labeled (CytoTracker™ Green) WBCs were spiked into healthy whole blood, only a very small percentage (1/10,000 WBCs) of them were captured inside the device.

Table 2-1. The composition of different types of leukocytes cells in whole blood and their volume and nucleus to cytoplasmic (N/C) ratios

Cell type	Percent in blood	N/C Ratio	Cell Size (µm)	Nucleus size (µm)
Myeloblast	<1	4:1	15 to 20	4.37
Promyelocyte	<1	3:1	14 to 20	5.66
Myelocyte	<1	2:1	12 to 18	7.5
Metamyelocyte	<1	1.5:1	10 to 15	8.33
Neutrophils	60-70	3:1	10 to 15	4.16
Eosinophils	2-4	2:1	12 to 17	7.25
Basophils	0-1	3:1	10 to 14	4
Promonocyte	<1	2 to 3:1	12 to 20	6.4
Monocyte	3-8	2 to 3:1	12 to 20	6.4
Lymphoblast	<1	4:1	10 to 18	3.5
Lymphocyte	20-30	3 to 5:1	7 to 18	3.12
Plasma Cell	<1	1 to 2:1	8 to 20	9.33

2.5.5 Cancer cell identification and verification

Microbeads are red in color and can be easily identified under white light, the same is not true for cancer cells. The fact that cancer cells and Leukocytes look almost the same under white light, makes it difficult to enumerate only trapped cancer cells. Hence, we adopted the fluorescence method of distinguishing between cancer cells and leukocytes.

Figure 2-17.a shows the DAPI stained cancer cell which is able to stain any cell with a nucleus (potential false positive for leukocyte). Hence, we use both nucleus staining and cytoplasm staining for cancer cell specific stain. Figure 2-17.b shows the two trapped cancer cells emit blue (from the center nucleus) and green light (from all surfaces except the nucleus). These can be seen in two different channels, one being Dapi (Nucleus staining of cancer cell for blue illumination) and the other GFP (cytoplasm staining of cancer cell for green illumination). When using blood samples, care must be taken to verify both channels to confirm the identity of the cell as cancer cell for accurate enumeration.

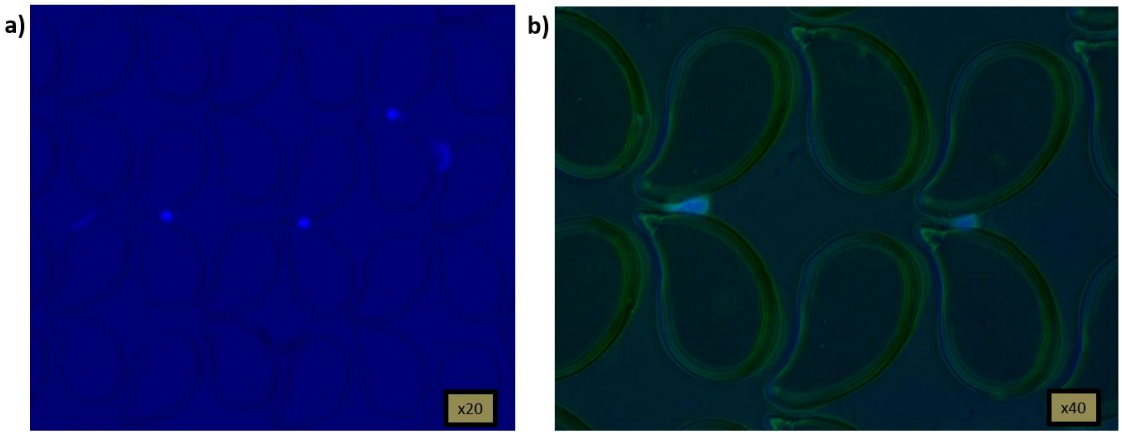

Figure 2-17. Cell visualization under microscope for enumeration. a) Dapi b) GFP and DAPI added visualization.

2.5.6 Change in velocity profile around a trapped particle.

Figure 2-18.a shows the computational analysis of the velocity profile of Design-I. When a particle is trapped as stated in the theory section that the drag forces increase in the bypass zone when a particle is trapped facilitating for it to rest and remain undisturbed

can be verified in this simulation. The velocity indicated in the red box region (near trapped particle) is slightly larger than that of the black box region (near no trapped particle) in Figure 2-18, thus verifying that once the particle is trapped the remaining incoming particles are diverted towards the slightly stronger bypass region and not disturb an already trapped particle. Similar case is observed in Design II Figure 2-18.b where the velocity is higher where the particle is trapped to make sure that all samples redirect away from the trapped particle.

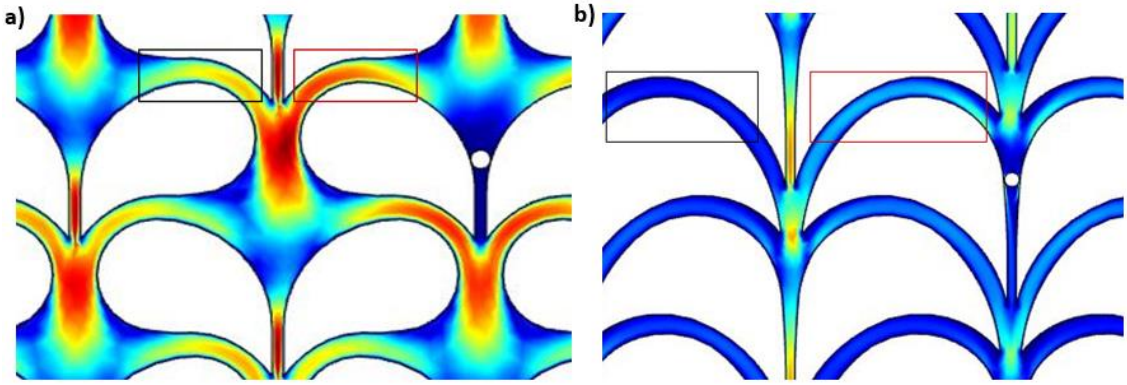

Figure 2-18. Changes in bypass velocity around a trapped particle.

2.6 Conclusions and future directions

Microfluidics has had significant effects on the biomedical disciplines and has been steadily improving for various scientific applications. Using multipurpose microposts, a novel and distinctive microfluidic isolation technique has been successfully demonstrated. In tests using microbeads and human blood infused with cancer cells, the platform showed high capture efficiency at rapid flow rates without clogging issues. Our technology used a unique size-based cell capturing unit in conjunction with a

microfluidic method in order to isolate significantly larger tumor cells from biological fluids. While the sample flow rate through the device as a whole was high, it was essential to maintain a low fluid movement velocity at the capture point in order to retain the trapped cell and minimize the shear stress on the cells to an absolute minimum. In the realm of biomedical research, these distinctive characteristics are crucial for preserving cell integrity and collecting cells for additional testing, making them a priceless asset for distinguishing uncommon cells from biological fluids (liquid biopsies). We employed a small number of cancer cells for routine testing, which reflects the clinical situation in cancer patients who normally have few CTCs in their blood.

In the future, investigations on viable cell release procedures must be carried out, along with assessments of the effect of entire blood samples on device performance. Advanced biological applications, such as tailored drug testing, mechanistic scientific research, advanced systems biology, and precision medicine, can make use of viable cell characterization. Future diagnostic and therapeutic applications of the innovative microfluidic device principles as well as molecular analysis of collected biological particles are possible; however, to achieve a robust clinical implementation, additional rigorous, standardized human application studies are required.

2.7 References

[33] J. Sun et al., “Double spiral microchannel for label-free tumor cell separation and enrichment.,” Lab Chip, vol. 12, no. 20, pp. 3952–3960, 2012, doi: 10.1039/c2lc40679a.

[50] A. Munaz, M. J. A. Shiddiky, and N. T. Nguyen, “Recent advances and current challenges in magnetophoresis based micro magnetofluidics,” Biomicrofluidics, vol. 12, no. 3, May 2018, doi: 10.1063/1.5035388.

[51] J. Chung, D. Issadore, A. Ullal, K. Lee, R. Weissleder, and H. Lee, “Rare cell isolation and profiling on a hybrid magnetic/size-sorting chip,” Biomicrofluidics, vol. 7, no. 5, Sep. 2013, doi: 10.1063/1.4821923.

[52] J. Chung, D. Issadore, A. Ullal, K. Lee, R. Weissleder, and H. Lee, “Rare cell isolation and profiling on a hybrid magnetic/size-sorting chip,” Biomicrofluidics, vol. 7, no. 5, Sep. 2013, doi: 10.1063/1.4821923.

[53] M. M. Hoque and M. M. Alam, “Effects of Dean Number and curvature on fluid flow through a curved pipe with magnetic field,” in Procedia Engineering, Elsevier Ltd, 2013, pp. 245–253. doi: 10.1016/j.proeng.2013.03.114.

[77] S. Nagrath et al., “Isolation of rare circulating tumour cells in cancer patients by microchip technology,” Nature, vol. 450, no. 7173, pp. 1235–1239, Dec. 2007, doi: 10.1038/nature06385.

[78] S. Wang, Y. Zhou, X. Qin, S. Nair, X. Huang, and Y. Liu, “Label-free detection of rare circulating tumor cells by image analysis and machine learning,” Sci Rep, vol. 10, no. 1, Dec. 2020, doi: 10.1038/s41598-020-69056-1.

[79] A. A. S. Bhagat, H. W. Hou, L. D. Li, C. T. Lim, and J. Han, “Pinched flow coupled shear-modulated inertial microfluidics for high-throughput rare blood cell

separation," Lab Chip, vol. 11, no. 11, pp. 1870–1878, Jun. 2011, doi: 10.1039/c0lc00633e.

[80] D. R. Gossett et al., "Label-free cell separation and sorting in microfluidic systems," Analytical and Bioanalytical Chemistry, vol. 397, no. 8. pp. 3249–3267, Aug. 2010. doi: 10.1007/s00216-010-3721-9.

[81] A. F. Sarioglu et al., "A microfluidic device for label-free, physical capture of circulating tumor cell clusters," Nat Methods, vol. 12, no. 7, pp. 685–691, Jun. 2015, doi: 10.1038/nmeth.3404.

[82] J. Zhou, P. V. Giridhar, S. Kasper, and I. Papautsky, "Modulation of rotation-induced lift force for cell filtration in a low aspect ratio microchannel," Biomicrofluidics, vol. 8, no. 4, Jul. 2014, doi: 10.1063/1.4891599.

[83] J. Zhou, P. V. Giridhar, S. Kasper, and I. Papautsky, "Modulation of rotation-induced lift force for cell filtration in a low aspect ratio microchannel," Biomicrofluidics, vol. 8, no. 4, Jul. 2014, doi: 10.1063/1.4891599.

[84] M. Yamada, M. Nakashima, and M. Seki, "Pinched flow fractionation: Continuous size separation of particles utilizing a laminar flow profile in a pinched microchannel," Anal Chem, vol. 76, no. 18, pp. 5465–5471, Sep. 2004, doi: 10.1021/ac049863r.

[85] S. Choi, S. Song, C. Choi, and J. K. Park, "Hydrophoretic sorting of micrometer and submicrometer particles using anisotropic microfluidic obstacles," Anal Chem, vol. 81, no. 1, pp. 50–55, Jan. 2009, doi: 10.1021/ac801720x.

[86] S. Yan et al., “On-chip high-throughput manipulation of particles in a dielectrophoresis- active hydrophoretic focuser,” Sci Rep, vol. 4, May 2014, doi: 10.1038/srep05060.

[87] H. A. Nieuwstadt, R. Seda, D. S. Li, J. B. Fowlkes, and J. L. Bull, “Microfluidic particle sorting utilizing inertial lift force,” Biomed Microdevices, vol. 13, no. 1, pp. 97–105, Feb. 2011, doi: 10.1007/s10544-010-9474-6.

[88] N. Nivedita, P. Ligrani, and I. Papautsky, “Dean Flow Dynamics in Low-Aspect Ratio Spiral Microchannels,” Sci Rep, vol. 7, Mar. 2017, doi: 10.1038/srep44072.

[89] E. Dressaire and A. Sauret, “Clogging of microfluidic systems,” Soft Matter, vol. 13, no. 1. Royal Society of Chemistry, pp. 37–48, 2017. doi: 10.1039/C6SM01879C.

[90] D. Venugopal, N. Kasani, Y. Manjunath, G. Li, J. T. Kaifi, and J. W. Kwon, “Clog-free high-throughput microfluidic cell isolation with multifunctional microposts,” Sci Rep, vol. 11, no. 1, Dec. 2021, doi: 10.1038/s41598-021-94123-6.

[91] J. Y. Park, S. J. Yoo, E. J. Lee, D. H. Lee, J. Y. Kim, and S. H. Lee, “Increased poly(dimethylsiloxane) stiffness improves viability and morphology of mouse fibroblast cells,” Biochip J, vol. 4, no. 3, pp. 230–236, 2010, doi: 10.1007/s13206-010-4311-9.

[92] B. Nath, A. Raza, V. Sethi, A. Dalal, S. S. Ghosh, and G. Biswas, “Understanding flow dynamics, viability and metastatic potency of cervical cancer (HeLa) cells through constricted microchannel,” Sci Rep, vol. 8, no. 1, Dec. 2018, doi: 10.1038/s41598-018-35646-3.

[93] A. Krishnan Thota Radhakrishnan, C. Poelma, J. van Lier, and F. Clemens, “Laminar-turbulent transition of a non-Newtonian fluid flow,” Journal of Hydraulic Research, vol. 59, no. 2, pp. 235–249, 2021, doi: 10.1080/00221686.2020.1770876.

[94] A. Krishnan Thota Radhakrishnan, C. Poelma, J. van Lier, and F. Clemens, “Laminar-turbulent transition of a non-Newtonian fluid flow,” Journal of Hydraulic Research, vol. 59, no. 2, pp. 235–249, 2021, doi: 10.1080/00221686.2020.1770876.

[95] O. S. Ismail and G. T. Adewoye, “Analyses and Modeling of Laminar Flow in Pipes Using Numerical Approach,” Journal of Software Engineering and Applications, vol. 05, no. 09, pp. 653–658, 2012, doi: 10.4236/jsea.2012.59076.

[96] A. Drózdz and W. Elsner, “Study of Reynolds number effect on turbulent boundary layer near the separation,” in Journal of Physics: Conference Series, Institute of Physics Publishing, Nov. 2016. doi: 10.1088/1742-6596/760/1/012003.

[97] K. Cielicki and A. Piechna, “Can the dean number alone characterize flow similarity in differently bent tubes?,” Journal of Fluids Engineering, Transactions of the ASME, vol. 134, no. 5, 2012, doi: 10.1115/1.4006417.

[98] I. D. Johnston, M. B. McDonnell, C. K. L. Tan, D. K. McCluskey, M. J. Davies, and M. C. Tracey, “Dean flow focusing and separation of small microspheres within a narrow size range,” Microfluid Nanofluidics, vol. 17, no. 3, pp. 509–518, 2014, doi: 10.1007/s10404-013-1322-6.

[99] F. Schönfeld and S. Hardt, “Simulation of Helical Flows in Microchannels,” AIChE Journal, vol. 50, no. 4, pp. 771–778, Apr. 2004, doi: 10.1002/aic.10071.

[100] “Flow control in microfluidic devices.” [Online]. Available: www.elveflow.com

[101] J. Winslow, H. Otsuka, B. Govindarajan, and I. Chopra, “Basic understanding of airfoil characteristics at low Reynolds numbers (104–105),” J Aircr, vol. 55, no. 3, pp. 1050–1061, 2018, doi: 10.2514/1.C034415.

Chapter 3 Biocompatible nature of the novel microfluidic cell isolator with multifunctional microposts

3.1 Abstract

By enabling the management of biological samples in minuscule channels and chambers, microfluidic technology has proven to be a potent tool in medical and biological research. Due to its biocompatibility, microfluidics for cell cultures has garnered the attention of experts from all over the world among the various uses. In this article we present and evaluate the toxicity of the device which comprises of PDMS, PTFE and glass surfaces to which the biological entity comes in contact with. Furthermore, even the rare cells are isolated and retrieved separately to test for their viability. The viability test is carried out by culturing the cells that had contact with the microfluidic device. The test is concluded by verifying the status of cell-free DNA (CfDNA) and EVs from the flowthrough sample of patient's blood to finalize the biocompatibility of the said microfluidic device.

3.2 Introduction

The silicon-based elastomer polydimethylsiloxane (PDMS) has become widely used in the quickly growing industry of microfluidics over the past ten years. Technologies known as "lab-on-a-chip" [52], [54], [86] offer a number of benefits, including the simplicity of executing analytical procedures on tiny microfabricated platforms and the ease of cell culture. So, compared to standard in vitro investigations that are carried out in sizable commercial plates and flasks, these devices use a tiny fraction of the reagents,

tissue culture media, and priceless biological specimens. It is a well-liked polymer for uses ranging from surface micropatterning to the casting of 2D and 3D geometries from rigid master molds due to its straightforward fabrication process and design versatility. PDMS attaches spontaneously and irreversibly to common substrates like polystyrene and glass and is both optically transparent and gas permeable. Recent reviews have focused on the growing use of PDMS-based microfluidic systems in cell culture applications over the past few years. In the study of cell biology, cell culture is crucial. A better understanding of cell activity, including mutation over time, reaction to external stimuli (physical or chemical), cell-cell interaction [102], and other phenomena, can be achieved by allowing the growth and proliferation of cells [67], [103]–[105] in an artificial environment. Modern in vitro cell culture techniques are widely standardized and enable the growth of the majority of each type of cell without any problems [106], [107]. It should be considered that small volumes also equate to a smaller number of cells in addition to the optimal spatial and temporal control made possible by microfluidics. This is a significant feature since it enables the study of single cells as well as tiny cell populations rather than the canonical in vitro large cell populations.

The throughput of several research areas, including tests for drug testing [66], [108], has been demonstrated to increase with the use of microfluidic cell culture. In relation to this, recent years have seen tremendous success with these microtechnology approaches, both for 2D and 3D culture models. In this article we present a fully working microfluidic device (previously characterized) comprising not only of PDMS, but also other materials embedded in the fabrication process that needs to be evaluated for its toxicity towards live blood and cancer cells. The stated device comprises of materials such as PDMS

(Sylgard™ 184), glass slide and PTFE (Polytetrafluoroethylene) tubing with which cells come in contact while testing. Therefore, validating all surfaces for its biocompatibility is crucial for cell investigation on the said microfluidic platform device. By applying various approaches like viability of cell retrieved [48], [109], [110] and cell culturing [3], [74], we were able to successfully demonstrate the biocompatibility of the device towards all blood cells and cancer cells.

3.2.1 Cancer cell trapping and retrieval

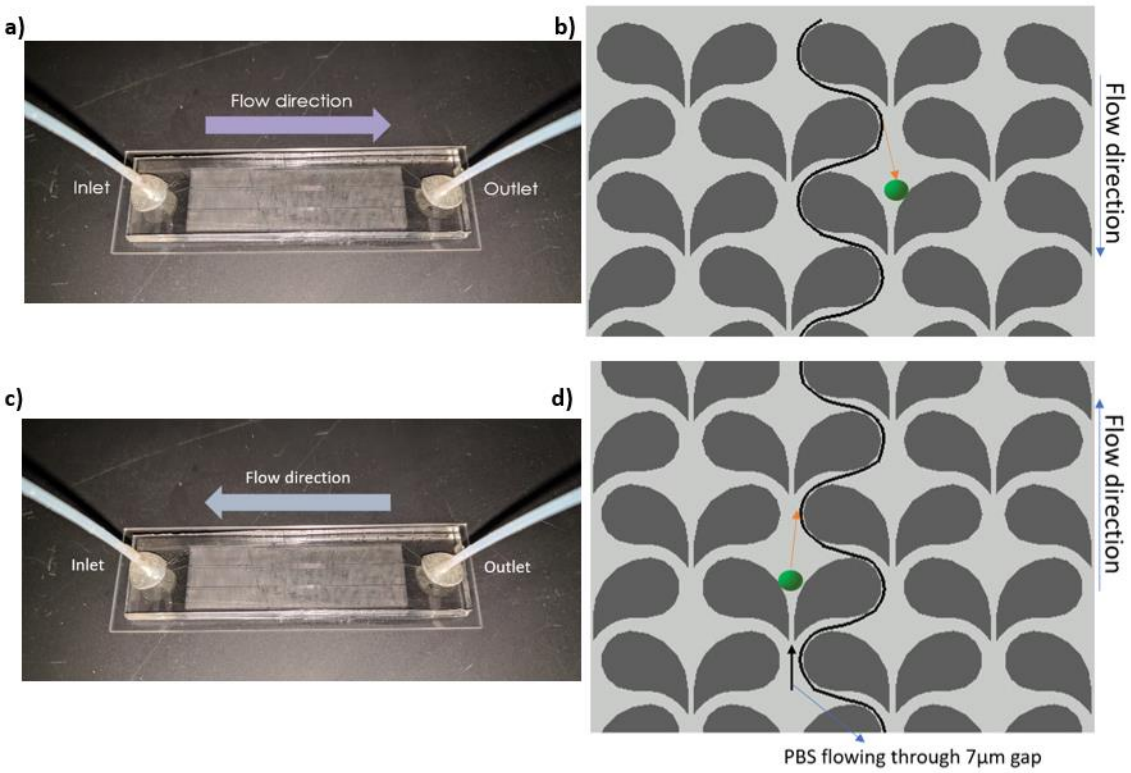

Figure 3-1. Cell trapping and retrieval process overview

In microfluidic, cell retrieval gives a huge advantage since picking out rare cancer cells in a vast pool of blood cells is a near to impossible task to achieve by pipette sorting. In the

previous chapter we have discussed a novel cell isolation microfluidic device and characterized its efficiency with various processes. Now that we have a very highly efficient trapping device for cancer cells, we must further focus on the biological aspect of the trapped cells. For this to succeed, first the trapped cell should be retrieved out of the device undamaged and in a time efficient manner since cells die off quickly in the outside environment. Figure 3-1 depicts the whole process of trapping and retrieval part of the experiment. For trapping the flow direction is from inlet to outlet Figure 3-1.a,b and once the cells are trapped (investigated under microscope), PBS solution could be flown from outlet to inlet Figure 3-1.c,d to force and nudge the trapped cell out of the trapping zone and then retrieved through the inlet. This sample can be now used for further biological tests since it only contains the rare cells and may be fewer number of blood cells. In the next section we will prove that the cells retrieved are viable and not damaged and discuss about their ability to run in coherent as other biological cells.

3.2.2 Other microfluidic designs

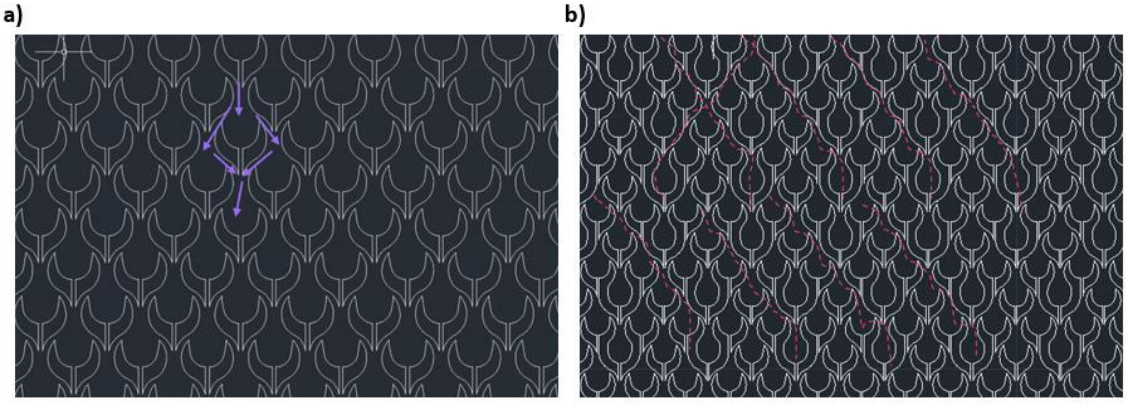

Figure 3-2. Horn and fused horn microposts design for microfluidic device

Once the success of Design I and Design II were evaluated, we ventured out for other designs to improve the retrieval efficiency. Both Design I and II had excellent capture efficiency of greater than 90% for both cells and microbeads but suffered a drawback with the cell retrieval. The retrieval efficiency for Design I and II were on an average of about 66%, that is for every ten rare cells trapped the highest probability of retrieved cells were about six. This issue had to be addressed and we produced horn design Figure 3-2.a . The horn design was assessed with both microbeads and cells and then retrieval was performed, the retrieval efficiency was above 80% which was a massive boost. But the drawbacks of this design were that the trapping efficiency was exceptionally low (around 60-70%). The trapping efficiency was improved a little (by 10%) using the fused horn design. Figure 3-2.b shows the fused horn design which has an extended horn every alternate row, the path of the fluid (red dotted lines in Figure 3-2.b) is always directed to a trapping zone once every 5^{th} row.

3.2.3 Comparison with other prevailing technologies

Table 3-1. Various CTC detection and isolation platforms

	Cell isolation principle	Efficiency	Quick process	Direct in-situ imaging/characterization of single CTC	Viable cell retrieval
Epic	Density	√			
Ikonisys	Density				
RareCyte	Density				
RosetteSep™	Density				√
ApoStream®	Dielectrophoresis		√		√
DEPArray™	Dielectrophoresis				√
AdnaTest	Immunomagnetic				
Biocep	Immunomagnetic	√			√
Biofluidica	Immunocapture	√			
CellSearch®	Immunomagnetic				
Cynvenio	Immunomagnetic	√			
Fluxion	Immunomagnetic	√			
Admonitrix	Laser-based	√	√		√
Clearbridge	Size-based	√	√		
Creatv	Size-based	√	√		
ISET	Size-based				
Parsortix™	Size & microfluidics		√	√	√
ScreenCell	Size-based		√		
TUMORTRAP	**Size & microfluidics**	**√**	**√**	**√**	**√**
Vortex	Size & microfluidics	√	√		√

Table 3-1 enlists current platforms available for CTC detection [111]–[114] or/and isolation [73], [115], [116]. The device we fabricated is known as TumorTrap [117], and we compared against other technologies with respect to efficiency, rate of process, and viable cell retrieval ability. The cell isolation principles used by these technologies are one of the following, Density, size-based, laser-based, immunomagnetic and size and microfluidics. The TumorTrap device ranks good in efficiency and imaging since the

device is transparent. Further, we will discuss the ability of TumorTrap to successfully retrieve single trapped cancer cells with ease and safe.

3.2.4 Cell free DNA isolation

Throughout the body, cells release cell-free DNA (cfDNA) into the bloodstream. Plasma and other bodily fluids, including cerebral spinal fluid (CSF), pleural fluid, urine, saliva, and others, can contain cfDNA. It is widely known that in healthy persons, majority of the plasma cfDNA molecules come from the hematological system. The related/affected organs, however, may release extra DNA [118]–[120] into the peripheral circulation in certain physiological or pathological situations, such as pregnancy, organ donation, and malignancies. Hence, noninvasively detecting cfDNA in peripheral blood could reveal a person's problems. Liquid biopsy, which is renowned for being non-invasive or minimally invasive, has demonstrated strong potential in identifying cancers at an early stage or pre-cancerous lesions. It is also capable of identifying cancers by detecting circulating tumor cells, exosomes [121]–[123], cfDNA, mRNA, microRNAs (miRNAs), proteins, or metabolites, among other things, few of which is graphically depicted in Figure 3-3. The most promising of them for identifying early-stage tumors is cfDNA, which are extracellular nucleic acid fragments released by cancer cells after apoptosis, necrosis, or secretion. Cancer-related genetic and epigenetic abnormalities, including as mutations, copy number changes, chromosomal rearrangements, hypermethylation, and hypomethylation, are visible in cfDNA.

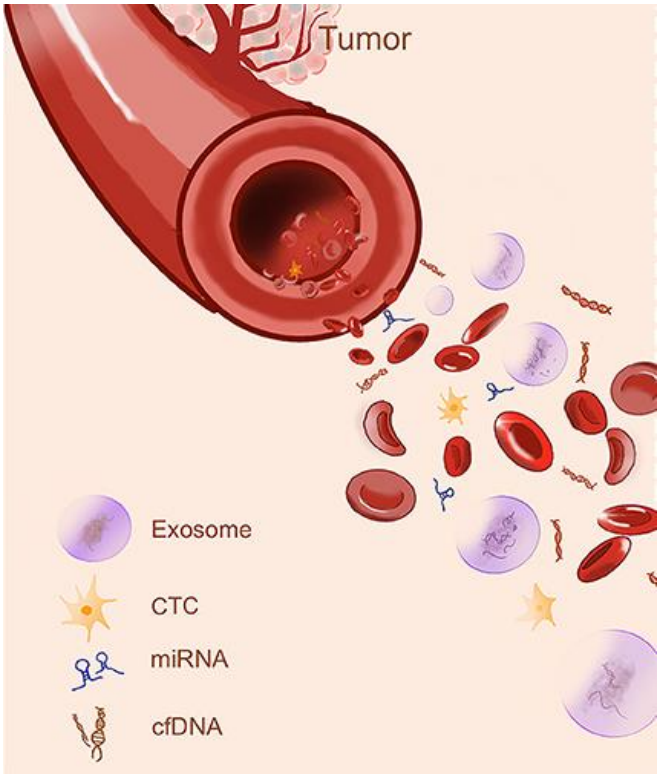

Figure 3-3. Micro-Particles that could originate from a tumor. [118]

3.2.5 Extracellular Vesicles

Extracellular vesicles (EVs) are lipid bilayer-delimited particles that are released by all types of cells in a normal manner but are unable to proliferate like cells. Although the vast majority of EVs are smaller than 200 nm, their diameter can range from 20 to 30 nano meters, which is close to the size of the smallest unilamellar liposome that is technically conceivable, to 10 microns or more [71], [124]–[128]. Exosomes, microvesicles, and apoptotic bodies are three categories into which EVs can be separated based on size and synthesis process. Proteins, nucleic acids [129], lipids, metabolites, and even organelles from the parent cell are all carried by them. Most cells that have been

investigated to date—including certain archaeal, bacterial, fungal, and plant cells that are enclosed by cell walls—are believed to release EVs.

Extracellular vesicles (EVs) are a special type of intercellular communication that are created by cancer cells and their importance is also depicted in the Figure 3-4 . These EVs can assist alter the tumor microenvironment, promote cell growth and survival, and improve invasive and metastatic activities. The way that EVs mediate their effects is what makes them so intriguing. Many bioactive cargo items, including as cell surface [130], cytosolic, and nuclear proteins, RNA transcripts, micro-RNAs (miRNAs), and even DNA fragments, have been found to be present in both MVs and exosomes. Both normal cell types and other cancer cells can receive EVs and their associated cargo, resulting in the recipient cells going through phenotypic alterations that support various elements of cancer growth. On the discovery that cancers release minute particles extracellular vesicles (EVs) into the bloodstream, including proteins from the tumor, new cancer detection techniques are being investigated.

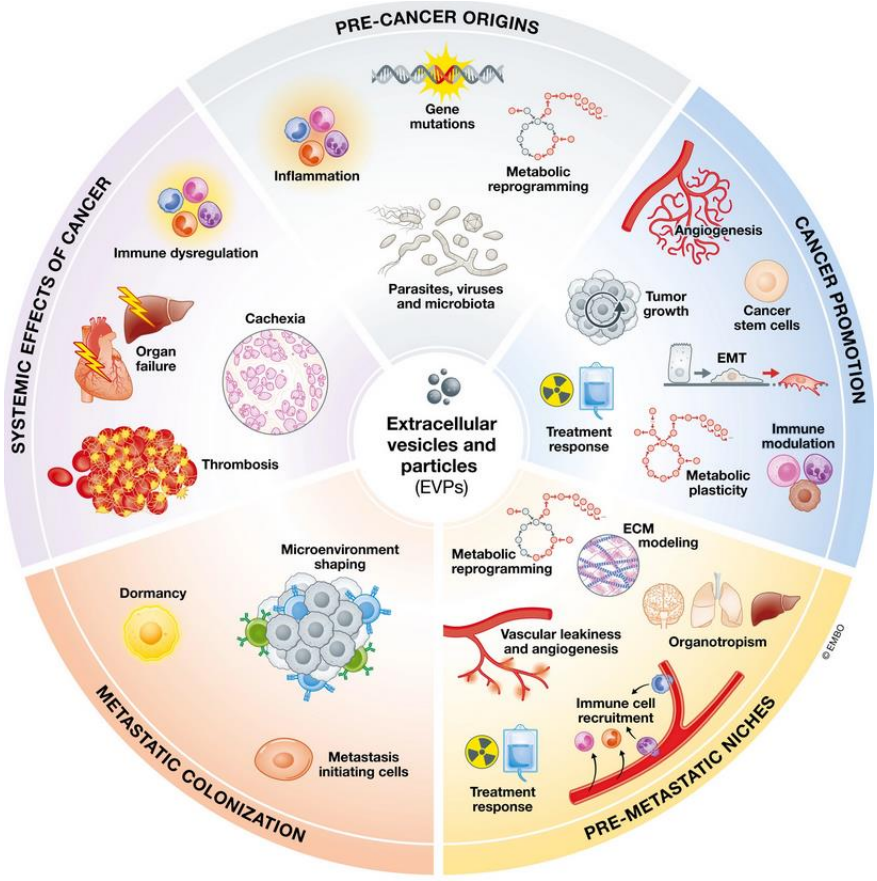

Figure 3-4. Overall contribution of EVs to different aspects of cancer. [126]

3.3 Materials and Methods

3.3.1 Cancer cell trapping and retrieval

The device was first prepped by infusing a total of 2ml phosphate-buffered saline (PBS) (Cat#: 14190250; Thermo-Fisher Scientific) at a flowrate of 0.5ml/min through the inlet. A known number of A549 cells were formalin-fixed, permeabilized, and stained with DAPI are carefully pipetted out from a culture dish and then spiked with either PBS or diluted human blood (1:5 in PBS) depending on the testing parameters. This mixture is infused using a syringe pump at a

flowrate of 0.5ml/min and the cancer cells are trapped. The device is later flushed with 2 ml of PBS buffer if diluted blood was used to remove the excess RBC's. Further, for the retrieval process the device is infused with PBS from the outlet port at a higher flowrate of 1.5 ml/min to dislocate the trapped cancer cells which will be retrieved at the inlet port.

3.3.2 Trapping efficiency and retrieval efficiency

Once the cells are trapped, the device is verified under brightfield microscope to ensure that enough cells are trapped. The number of cells trapped in the whole device are counted and then headed to the retrieval process. The sample retrieved from the inlet are stored in Falcon tubes. The sample was centrifuged at 1000 RPM for 5 minutes and the supernatant was discarded. The pellet at the bottom of the tube is collected and spread evenly on a glass slide from one end to another. Now using a brightfield microscopy, the number of cells on the glass slides are counted thoroughly. The retrieval efficiency is calculated by the percentage ratio of retrieved cells to the trapped cell count from the beginning of the experiment.

3.3.3 COMSOL simulation of new Designs

The velocity profiles inside the device were computationally simulated using COMSOL Multiphysics® version 5.3a finite element analysis software (COMSOL Inc., Burlington, MA), as shown in Figure 2-12. By joining two partial curves the asymmetrical geometry of horn Design was created. For fused design neighboring microposts were fused

alternatively to form the fused design. Using the COMSOL software, numerical analysis was done to determine the ideal operating circumstances and design for the microposts. The fluidic medium under the test was operated under conditions similar to that of water, including incompressible flow, an inlet linear velocity of 2 mm/sec, no-slip boundary conditions for all walls, and zero outlet pressure.

3.3.4 Device toxicity towards A549 cancer cells with PBS as fluid medium

The device was first prepped by infusing a total of 2ml phosphate-buffered saline (PBS) (Cat#: 14190250; Thermo-Fisher Scientific) followed by 4ml of 70% ethanol at 0.1 ml/min to sterilize the microfluidic channels and then followed by 2ml of PBS buffer to clear out ethanol. The trapping test was first performed by infusing the device inlet with a mixture of approx. 5000 A549 cancer cells suspended in 4ml PBS buffer solution. The trapping and retrieval were performed in succession. The sample was centrifuged at 1000 RPM for 5 minutes and the supernatant was discarded, and the pellet was pipetted into a 96 well plate. Simultaneously, approx. 5000 naive A549 cells were pipetted into another 96 well plate which will be used for comparison. Each test was performed three times to check for repeatability.

3.3.5 Device toxicity towards A549 cancer cells with blood as fluid medium

The device was first prepped by infusing a total of 2ml phosphate-buffered saline (PBS) (Cat#: 14190250; Thermo-Fisher Scientific) followed by 4ml of 70%

ethanol at 0.1 ml/min to sterilize the microfluidic channels and then followed by 2ml of PBS buffer to clear out ethanol. Healthy human blood was diluted 1:5 (Blood: PBS) by using 1ml of blood and mixing it with 4ml of PBS. The trapping test was first performed by infusing the device inlet with a mixture of approx. 5000 A549 cancer cells suspended in the above stated mixture. The trapping and retrieval were performed in succession. The sample was centrifuged at 1000 RPM for 5 minutes and the supernatant was discarded, and the pellet was pipetted into a 96 well plate. Simultaneously, approx. 5000 naive A549 cells were pipetted into another 96 well plate which will be used for comparison. Each test was performed three times to check for repeatability.

3.3.6 Cell free DNA isolation

The patient blood sample is diluted 1:1 and infused through the device for CTC isolation and the flowthrough fluid is collected at the outlet port. Flowthrough blood and control blood (from the same patient without device contact) are double-centrifuged and the supernatant (cell free plasma) to isolate cfDNA using Qlamp circulating nucleic acid kit (Qiagen). The DNA concentration (ng/µl) is measured using a high sensitivity (HS) Qubit® assay. cfDNA quality will be determined by ~1ng on Agilent Bioanalyzer HS DNA chip.

3.3.7 Extracellular Vesicles

The patient blood sample is diluted 1:1 and infused through the device for CTC isolation and the flowthrough fluid is collected at the outlet port. Flowthrough blood and control blood (from the same patient without device contact) are double centrifuged to remove platelets and the platelet poor plasma. Size exclusion chromatography (SEC) succeeded with ultracentrifugation to purify the EVs. The EV particle size (nm) and concentration (particles/ml) are determined using nanoparticle tracking analysis (NTA). 5µl of purified EV sample is applied to a freshly glow discharged (PELCO easiGlow™) carbon coated TEM grid over ice. Samples are washed three times with distilled water, incubated for 2min on 2% paraformaldehyde followed by incubation for 30 sec on 2% uranyl acetate (aqueous) and back blotted with filter paper (Whatman P1; Fisher Scientific) and dried. Images are collected on a JEOL JEM 1400 transmission electron microscope at 120V equipped with a Gatan Ultra scan 1000 CCD camera.

3.3.8 Reproducibility among users

A known number of cancer cells are spiked into diluted human blood (1:5 in PBS) and given to the user who performs the testing experiments unaware of the numerical value of spiked cells. The test is performed as described in cancer cell testing methods using Design-I device by infusing using a syringe pump at a constant flowrate of 0.5 ml/min. The capture efficiency is later calculated after the

blind study has ended by using the ratio of captured cell to number of spiked cells. The test is repeated three times for each cell counts type (1,2,5 and 10).

3.3.9 Patient sample CTC comparison

The blood samples were retrieved from the same patient using three 10 ml CellSave preservative tubes. One tube was sent out to cell search processing facility while the second and third were being tested at home using cell sieve and our microfluidic device. Our device was first prepped by flushing it with PBS at 1 ml/min for 2 minutes. Then the blood sample was diluted (1:5) with PBS and infused at a rate of 0.25 ml/min to obtain maximum capture efficiency. Now the excess RBCs are removed by flushing the device using PBS and then 0.5 ml of 4% formalin solution in injected and kept stationary for 20 minutes. The final step involves injecting staining solution just enough to fill the microfluidic channels (approx. 200µl) and then stored at 4°C overnight. The number of trapped cells is noted by traversing through the entire device from inlet to outlet under a microscope.

3.4 Results and Discussion

3.4.1 Retrieval efficiency for Design I and II

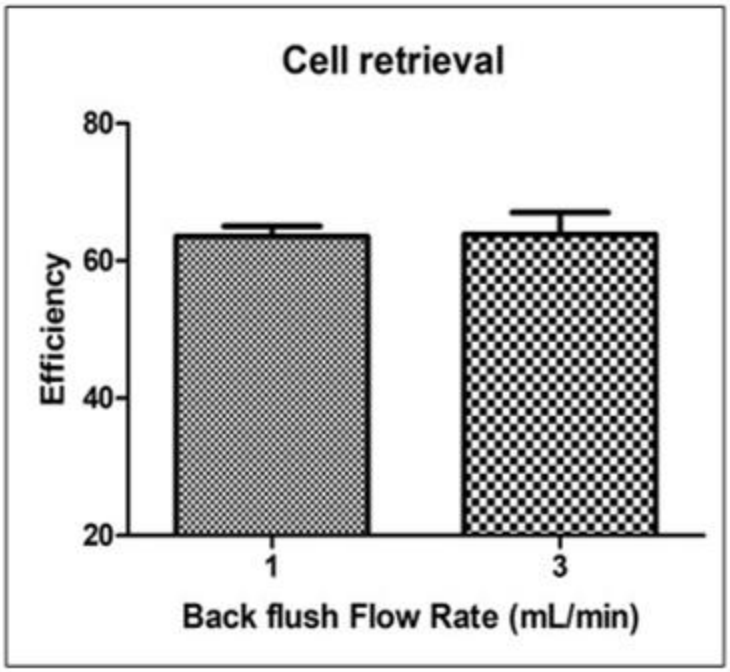

Figure 3-5. Cell retrieval efficiency of Design I and II

Cells have diverse and varying sizes, shapes, dynamics, densities, and demonstrate plasticity under physiological settings, as opposed to stable, fixed-size microbeads [131], [132]. Due to shear stress caused by fluid movement within the device, cells are vulnerable to injury and loss of integrity due to their biological characteristics. 87% of human cancer cells were successfully captured by Design-I at 1 ml/min Figure 2-14.a . When compared to conventional microfluidic methods, a flow rate of 0.5 ml/min maintained a sufficiently high capture efficiency. As seen from the Figure 3-5, the efficiency of retrieval is around 66% for Design I and II. This is mainly because the geometry is designed to trap efficiently but in the reverse direction the flow changes rapidly and lot of interactions and bouncing off the microposts walls leading to a chaotic and unpredictable flow of the particles leading to a very low efficiency. Figure 3-5 also shows that the retrieval efficiency increases slightly with increase in the backflush

flowrate. This proves that the lodged particle experiences more fluid force from the trapping region to follow the main flow path thus increasing the retrieval rate.

3.4.2 COMSOL simulation of the new Designs

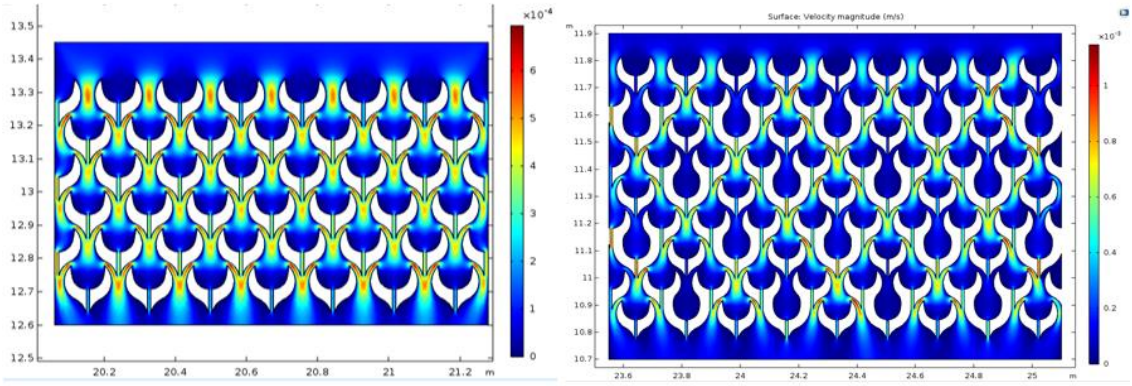

Figure 3-6. COMSOL Velocity profiles of a). Horn design and b). Fused horn design.

COMSOL software was used to conduct finite element analysis to determine the ideal operating circumstances and design for the microposts with horn-like geometry Figure 3-6. The fluidic medium's operational conditions, which included incompressible flow, an inlet linear velocity of 12 mm/sec, no-slip boundary conditions for all walls, and an output pressure of zero, were comparable to those of water. For the horn design the thermal graph's depiction of the velocity profile in the area separating the two by-passing channels is shown in Figure 3-6.a . High velocity was seen above the capture point, which helped to successfully direct the laterally displaced particle there. Here each microposts pair has a directing velocity profile above it suggests the direction of larger particle is always to the next trapping pair. The COMSOL simulation case is quite

different for fused horn design. As shown in Figure 3-6.b, the downward directing velocity profile is only visible once every 5th row due to the alignment of the microposts and its geometry. In the intermediate rows the flow pattern follows the microposts exterior all the way to be directed downwards at the 5th row. This gives enough time and distance for a particle to achieve the necessary force to be redirected away from the main flow. This certainly is the main deciding factor on to why the retrieval is so high in these designs since the flow follows an almost straight path in the reverse direction in Figure 3-6.b. The above simulation was then verified by testing the device with microbeads and cancer cells as shown in Figure 3-7.a and b respectively.

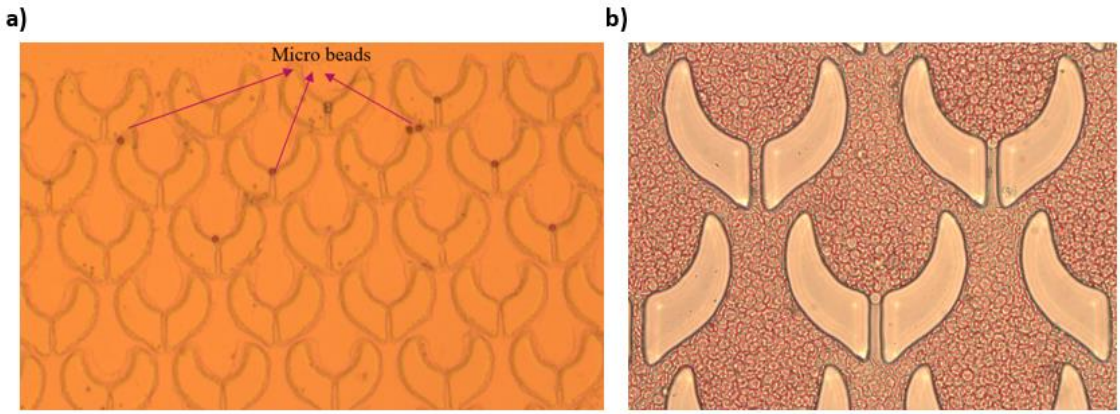

Figure 3-7. Microscopic images of trapped a). Microbeads and b). Cancer cell in horn design

3.4.3 Device toxicity with PBS as fluid medium

To check the device toxicity, the A549 lung cancer cells were passed through the device and were retrieved using backflush mechanism using Design-I. The cells were then cultured in a controlled environment to see their growth rate and analyze the device toxicity towards these cells. This test was performed using cells and PBS only as an

initial step. The Figure 3-8.a shows the images of cultured cells that were retrieved from the device and Figure 3-8.b shows the cell cultured without the device contact (naïve cells) as a control reference. The cells growth was acceptable with no contamination concluding the device biocompatibility towards A549 cells. The naïve cells culture rate was much higher since the device retrieval efficiency is a little low.

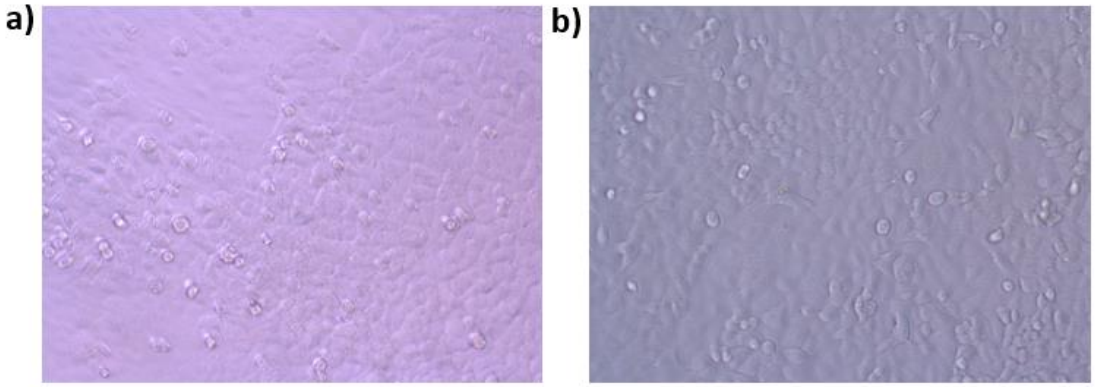

Figure 3-8. Cell culture of the retrieved cells from the device tested using PBS as fluid medium.

3.4.4 Device toxicity with blood as fluid medium

To further verify the device toxicity in a clinical setting, the A549 lung cancer cells were mixed in diluted blood and then passed through the device and were retrieved using backflush mechanism using Design-I. The cells were then cultured in a controlled environment to see their growth rate and analyze the device toxicity towards these cells. Since this test was performed using cells and diluted blood, a PBS wash step was performed to remove excess RBCs. The Figure 3-9.a shows the images of cultured cells that were retrieved from the device and Figure 3-9.b shows the cell cultured without the device contact (naïve cells) as a control reference. The cells growth was acceptable with

no contamination even with the presence of few RBCs from the device and thus concluding the device biocompatibility towards A549 cells and blood cells. The naïve cells culture rate was much higher since the device retrieval efficiency is a little low.

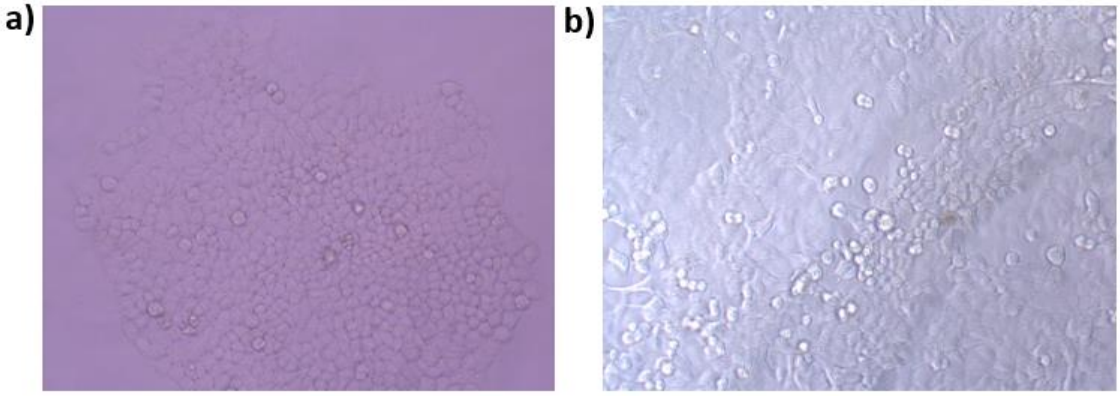

Figure 3-9. Cell culture of the retrieved cells from the device tested using blood as fluid medium.

3.4.5 Cell free DNA isolation

Table 2. CfDNA analysis of the plasma with and without device contact

Sample	Concentration (ng/µl)	260/280	260/230	Yield/ml plasma (µg/ml)
Plasma (no device)	16.1	1.82	0.46	0.161
Plasma (after device)	15.3	1.62	0.26	0.153

The CfDNA enrichment was performed to demonstrate the multiple utility of the device using a single blood drawn from the patient. CfDNA concentration was measured in plasma that has been enriched from the whole blood passed through the device for CTC

isolation and the parameters are listed in Table 2. The CfDNA concentration in plasma from fresh blood and device processed blood was not significantly different (Student t test p=0.572) demonstrating that single blood draw from the patient is sufficient for both CTC and cfDNA enrichment (Figure 3-10.a). Furthermore, CfDNA fragment size analysis revealed that DNA is not fragmented after passing through the chip (Figure 3-10.b).

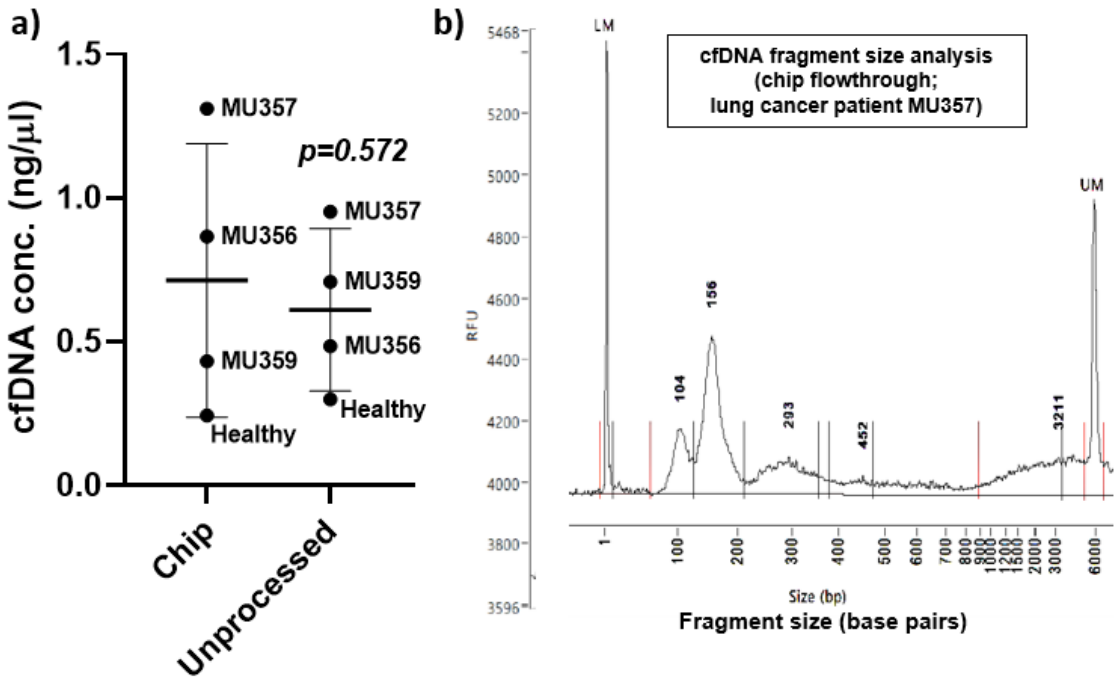

Figure 3-10. cfDNA fragment size analysis from patient blood sample

3.4.6 Extracellular Vesicles (EVs)

Another major component of liquid biopsies together with CTCs and cfDNA is EVs. There was a slight difference observed in the size of EVs that collected in device flow through compared to EVs that were enriched using the columns directly from patient

plasma. This could be due to the fact that the microposts in the device pose some shear stress on EVs that results in reshaping of EVs while flowing through (Figure 3-11.c,d). However, the intensity of EVs was not significantly changed between the two groups (Figure 3-11.a,b). Overall, cfDNA and EVs data demonstrates the multiple utility of the device. Figure 3-11.e,f. provides the Transmission Electron Microscopy (TEM) images of the EVs found to show the structural intactness of the EVs after flowing through the device.

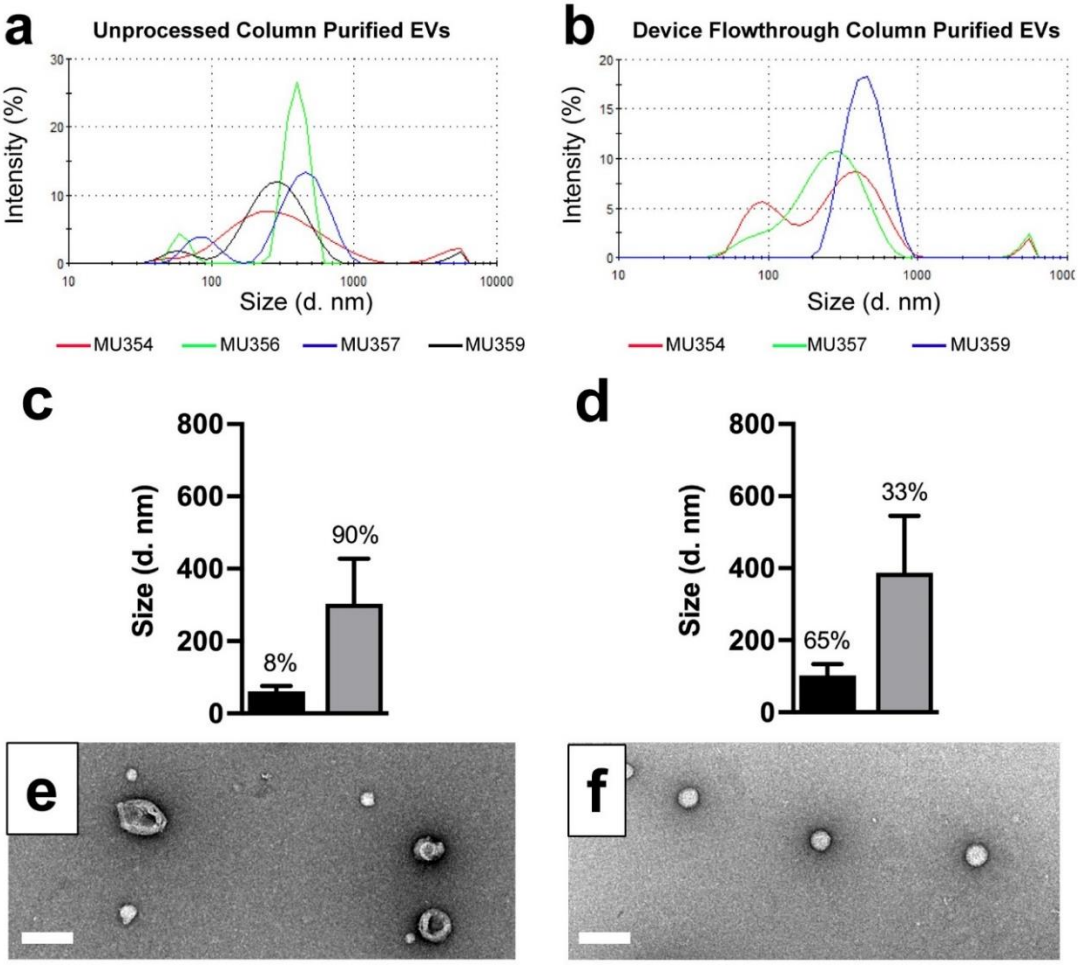

Figure 3-11. Size exclusion chromatography of EVs in patient blood sample

3.4.7 CTC Technology comparison using patient samples.

The FDA approved CellSearch® technology [112], [133] is the only prevailing method out there for CTCs specific cells detection, enumeration, and analysis. But the Cell search uses a unique immunomagnetic and fluorescence imaging to analyze the CTC in a blood sample. The CellSearch® technology does not produce a permanent specimen or derivative slide to be used down the road, in contrast to other technologies that capture CTCs for further study; instead, only electronic results (cell pictures) are stored, restricting further examination of the caught cell. Based on these parameters the number of cells enumerated by cell search is very less as compared to the TumorTrap which relies on cell size, density, and microfluidic flow patterns. Cell sieve is another technology we use in the lab for enumeration and further analysis of cancer cells which costs less than the cell search process. Cellsieve™ is a membrane-based filter which has pores of the dimension to trap specific cells by size. Figure 3-12 shows the comparison of the rare cancer cells in 7.5 mL of patient blood sample, caught by the three technologies mentioned. From the figure it is evident that the TumorTrap can trap cells with higher efficiency and also can be released for single cell analysis [134], [135].

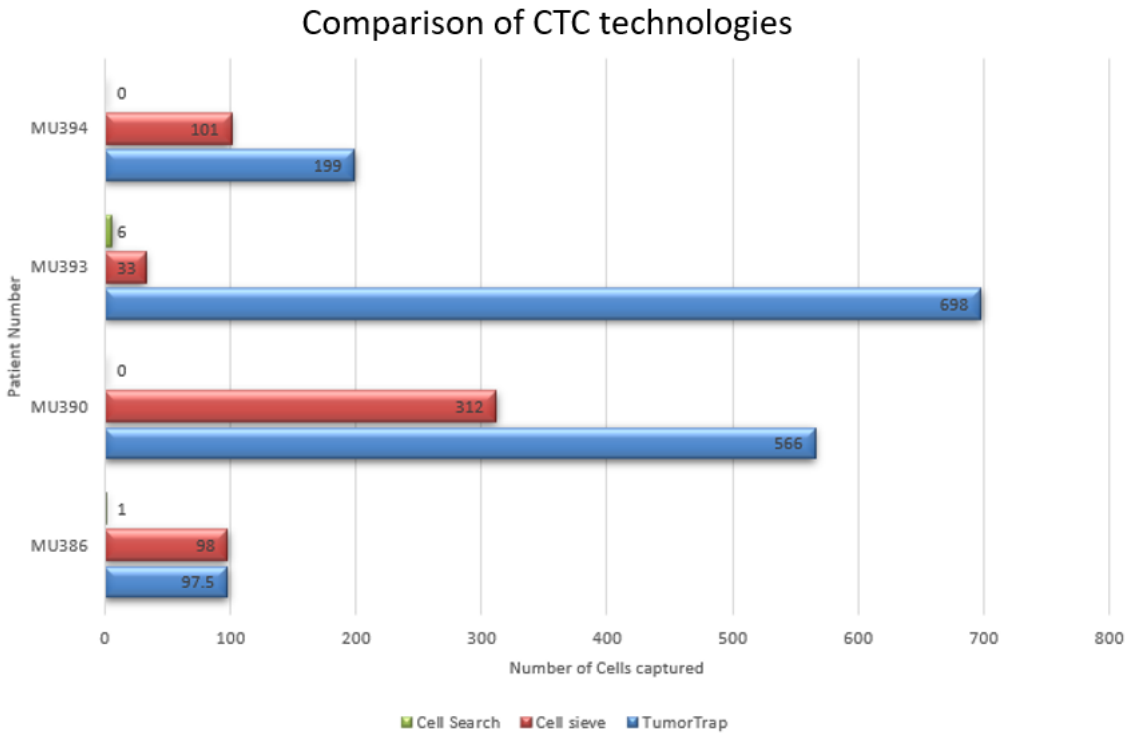

Figure 3-12. Patient cancer cell detection comparison with our device and other technologies.

3.4.8 Reproducibility among users

The process by which it is determined, through laboratory investigations, that the method's performance characteristics fulfill the requirements for its intended purpose is known as method validation. It is a step in the whole validation process, which also involves the validation of software, the qualification of instruments, and the applicability of systems. The difference in measurements between two operators are required to evaluate a said device on its way for commercialization. This is done to ensure that any user with basic knowledge should be able to recreate the exact laboratory scenarios. The Figure 3-13 we can observe that two users were used to validate the method process. All tests were single blinded test for the second operator to compare with the main tester.

Figure 3-13.d shows the maximum number of trapped cells counted between two users and the variation as plotted is not far from the original. The inter operator variability shown in Figure 3-13.c shows slight deviation from the original user, mainly because of the rarity of the cancer cells in blood and 1 cell loss accounts to more than 10% decrease in efficiency for tests.

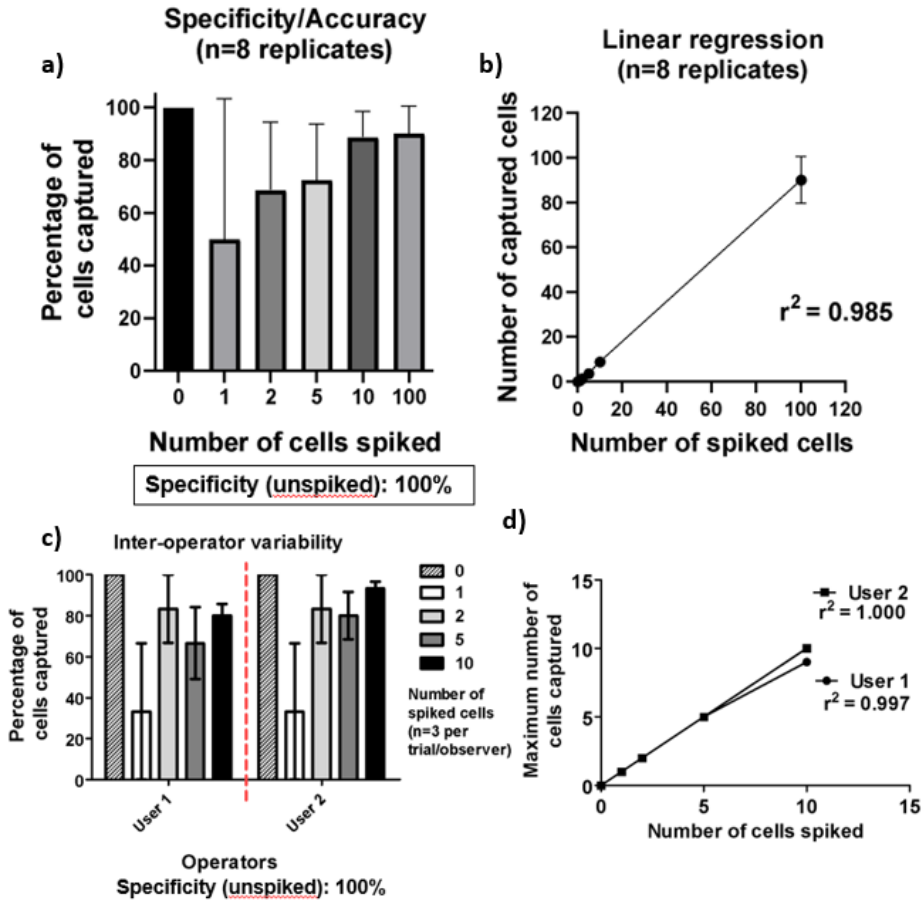

Figure 3-13. Methods validation with different user

3.5 Conclusion and future path

A common biological substance in microfluidic for medical purposes is now PDMS. This article discusses the usefulness of PDMS in various medical applications, and the investigation of its biocompatibility towards cancer cells and other blood cells, demonstrating its significance for both the present and the future of biomedicine. For contemporary medical, biological, and pharmacological research, cell culture is at a critical stage. Modern laboratories employ culture techniques that have been developed over a century of research. In conclusion, we can affirm that the device presented here made of multiple materials like PDMS, PTFE and glass slide are biologically compatible with all types of cells used and verified by a number of techniques as stated before. However, it must be stressed that more testing is required to standardize and commercialize this patented device for use in clinical trials. Currently having a device like TumorTrap [117] in research laboratory settings for alternate cell line analysis could give more data and help towards significant reach towards commercialization.

3.6 References

[3] S. Torino, B. Corrado, M. Iodice, and G. Coppola, “Pdms-based microfluidic devices for cell culture,” Inventions, vol. 3, no. 3. MDPI Multidisciplinary Digital Publishing Institute, Sep. 01, 2018. doi: 10.3390/inventions3030065.

[48] P. E. Thiriet, J. Pezoldt, G. Gambardella, K. Keim, B. Depla, and C. Guiducci, “Selective retrieval of individual cells from microfluidic arrays combining dielectrophoretic force and directed hydrodynamic flow,” Micromachines (Basel), vol. 11, no. 3, Mar. 2020, doi: 10.3390/mi11030322.

[52] J. Chung, D. Issadore, A. Ullal, K. Lee, R. Weissleder, and H. Lee, “Rare cell isolation and profiling on a hybrid magnetic/size-sorting chip,” Biomicrofluidics, vol. 7, no. 5, Sep. 2013, doi: 10.1063/1.4821923.

[54] J. Grant, A. Özkan, C. Oh, G. Mahajan, R. Prantil-Baun, and D. E. Ingber, “Simulating drug concentrations in PDMS microfluidic organ chips,” Lab Chip, vol. 21, no. 18, pp. 3509–3519, Sep. 2021, doi: 10.1039/d1lc00348h.

[66] M. I. Khot et al., “Characterising a PDMS based 3D cell culturing microfluidic platform for screening chemotherapeutic drug cytotoxic activity,” Sci Rep, vol. 10, no. 1, Dec. 2020, doi: 10.1038/s41598-020-72952-1.

[67] S. J. Streichan, C. R. Hoerner, T. Schneidt, D. Holzer, and L. Hufnagel, “Spatial constraints control cell proliferation in tissues,” Proc Natl Acad Sci U S A, vol. 111, no. 15, pp. 5586–5591, Apr. 2014, doi: 10.1073/pnas.1323016111.

[71] S. S. Deville and N. Cordes, “The Extracellular, Cellular, and Nuclear Stiffness, a Trinity in the Cancer Resistome—A Review,” Frontiers in Oncology, vol. 9. Frontiers Media S.A., Dec. 06, 2019. doi: 10.3389/fonc.2019.01376.

[73] K. G. Phillips et al., “Optical quantification of cellular mass, volume, and density of circulating tumor cells identified in an ovarian cancer patient,” Front Oncol, vol. 2 JUL, 2012, doi: 10.3389/fonc.2012.00072.

[74] K. J. Regehr et al., “Biological implications of polydimethylsiloxane-based microfluidic cell culture,” Lab on a Chip, vol. 9, no. 15. Royal Society of Chemistry, pp. 2132–2139, 2009. doi: 10.1039/b903043c.

[102] P. Friedl, K. S. Zänker, and E. B. Bröcker, “Cell migration strategies in 3-D extracellular matrix: Differences in morphology, cell matrix interactions, and integrin function,” Microscopy Research and Technique, vol. 43, no. 5. pp. 369–378, Dec. 01, 1998. doi: 10.1002/(SICI)1097-0029(19981201)43:5<369::AID-JEMT3>3.0.CO;2-6.

[103] M. A. Heinrich, R. Alert, J. M. Lachance, T. J. Zajdel, A. K. Mrlj, and D. J. Cohen, “Size-dependent patterns of cell proliferation and migration in freely-expanding epithelia,” Elife, vol. 9, pp. 1–21, Aug. 2020, doi: 10.7554/ELIFE.58945.

[104] C. Gérard and A. Goldbeter, “The balance between cell cycle arrest and cell proliferation: Control by the extracellular matrix and by contact inhibition,” Interface Focus, vol. 4, no. 3, 2014, doi: 10.1098/rsfs.2013.0075.

[105] C. Gérard and A. Goldbeter, “The balance between cell cycle arrest and cell proliferation: Control by the extracellular matrix and by contact inhibition,” Interface Focus, vol. 4, no. 3, 2014, doi: 10.1098/rsfs.2013.0075.

[106] “Chapter 12 - Cell Growth first-page-pdf”.

[107] J. J. Tyson and B. Novak, “Control of cell growth, division and death: Information processing in living cells,” Interface Focus, vol. 4, no. 3. Royal Society, 2014. doi: 10.1098/rsfs.2013.0070.

[108] J. Sun, A. R. Warden, and X. Ding, “Recent advances in microfluidics for drug screening,” Biomicrofluidics, vol. 13, no. 6. American Institute of Physics Inc., Nov. 01, 2019. doi: 10.1063/1.5121200.

[109] “RETRIEVAL OF ARTIFICIAL BLOOD CELLS (PERFLUOROCHEMICAL) FROM WHOLE BLOOD RETRIEVAL_OF_ARTIFICIAL_BLOOD_CELLS.89”.

[110] H. W. Hou et al., “Isolation and retrieval of circulating tumor cells using centrifugal forces,” Sci Rep, vol. 3, 2013, doi: 10.1038/srep01259.

[111] P. Paterlini-Brechot and N. L. Benali, “Circulating tumor cells (CTC) detection: Clinical impact and future directions,” Cancer Letters, vol. 253, no. 2. Elsevier Ireland Ltd, pp. 180–204, Aug. 18, 2007. doi: 10.1016/j.canlet.2006.12.014.

[112] M. C. Miller, G. V. Doyle, and L. W. M. M. Terstappen, “Significance of Circulating Tumor Cells Detected by the CellSearch System in Patients with Metastatic Breast Colorectal and Prostate Cancer,” J Oncol, vol. 2010, pp. 1–8, 2010, doi: 10.1155/2010/617421.

[113] Z. Shen, A. Wu, and X. Chen, “Current detection technologies for circulating tumor cells,” Chemical Society Reviews, vol. 46, no. 8. Royal Society of Chemistry, pp. 2038–2056, Apr. 21, 2017. doi: 10.1039/c6cs00803h.

[114] S. Ju et al., “Detection of circulating tumor cells: opportunities and challenges,” Biomarker Research, vol. 10, no. 1. BioMed Central Ltd, Dec. 01, 2022. doi: 10.1186/s40364-022-00403-2.

[115] C. V. Pecot et al., “A novel platform for detection of CK + and CK - CTCs,” Cancer Discov, vol. 1, no. 7, pp. 580–586, Dec. 2011, doi: 10.1158/2159-8290.CD-11-0215.

[116] N. Norouzi, H. C. Bhakta, and W. H. Grover, “Sorting cells by their density,” PLoS One, vol. 12, no. 7, Jul. 2017, doi: 10.1371/journal.pone.0180520.

[117] “Patent uspto 16830617 microfluidic device patent tumortrap ”.

[118] Y. Y. Yan et al., “Cell-Free DNA: Hope and Potential Application in Cancer,” Frontiers in Cell and Developmental Biology, vol. 9. Frontiers Media S.A., Feb. 22, 2021. doi: 10.3389/fcell.2021.639233.

[119] Q. Gao et al., “Circulating cell-free DNA for cancer early detection,” Innovation, vol. 3, no. 4. Cell Press, Jul. 12, 2022. doi: 10.1016/j.xinn.2022.100259.

[120] M. Cisneros-Villanueva et al., “Cell-free DNA analysis in current cancer clinical trials: a review,” British Journal of Cancer. Springer Nature, 2022. doi: 10.1038/s41416-021-01696-0.

[121] J. Dai et al., “Exosomes: key players in cancer and potential therapeutic strategy,” Signal Transduction and Targeted Therapy, vol. 5, no. 1. Springer Nature, Dec. 01, 2020. doi: 10.1038/s41392-020-00261-0.

[122] Y. L. Tai, K. C. Chen, J. T. Hsieh, and T. L. Shen, “Exosomes in cancer development and clinical applications,” Cancer Science, vol. 109, no. 8. Blackwell Publishing Ltd, pp. 2364–2374, Aug. 01, 2018. doi: 10.1111/cas.13697.

[123] M. D. A. Paskeh et al., “Emerging role of exosomes in cancer progression and tumor microenvironment remodeling,” Journal of Hematology and Oncology, vol. 15, no. 1. BioMed Central Ltd, Dec. 01, 2022. doi: 10.1186/s13045-022-01305-4.

[124] X. Zhang et al., “The Biology and Function of Extracellular Vesicles in Cancer Development,” Frontiers in Cell and Developmental Biology, vol. 9. Frontiers Media S.A., Nov. 05, 2021. doi: 10.3389/fcell.2021.777441.

[125] N. Tominaga, “Anti-cancer role and therapeutic potential of extracellular vesicles,” Cancers, vol. 13, no. 24. MDPI, Dec. 01, 2021. doi: 10.3390/cancers13246303.

[126] S. Lucotti, C. M. Kenific, H. Zhang, and D. Lyden, “Extracellular vesicles and particles impact the systemic landscape of cancer,” EMBO J, vol. 41, no. 18, Sep. 2022, doi: 10.15252/embj.2021109288.

[127] R. Xu, A. Rai, M. Chen, W. Suwakulsiri, D. W. Greening, and R. J. Simpson, “Extracellular vesicles in cancer — implications for future improvements in cancer care,” Nature Reviews Clinical Oncology, vol. 15, no. 10. Nature Publishing Group, pp. 617–638, Oct. 01, 2018. doi: 10.1038/s41571-018-0036-9.

[128] K. Qian, W. Fu, T. Li, J. Zhao, C. Lei, and S. Hu, “The roles of small extracellular vesicles in cancer and immune regulation and translational potential in cancer therapy,” Journal of Experimental and Clinical Cancer Research, vol. 41, no. 1. BioMed Central Ltd, Dec. 01, 2022. doi: 10.1186/s13046-022-02492-1.

[129] “Assessment of Nucleic Acid Purity.” [Online]. Available: www.nanodrop.com

[130] W. Zhang, D. S. Choi, Y. H. Nguyen, J. Chang, and L. Qin, “Studying cancer stem cell dynamics on PDMS surfaces for microfluidics device design,” Sci Rep, vol. 3, 2013, doi: 10.1038/srep02332.

[131] M. A. Giese, L. E. Hind, and A. Huttenlocher, “Neutrophil plasticity in the tumor microenvironment,” 2019. [Online]. Available: https://ashpublications.org/blood/article-pdf/133/20/2159/1557207/blood844548.pdf

[132] D. Zink, A. H. Fischer, and J. A. Nickerson, “Nuclear structure in cancer cells,” Nature Reviews Cancer, vol. 4, no. 9. pp. 677–687, Sep. 2004. doi: 10.1038/nrc1430.

[133] S. Riethdorf et al., “Detection of circulating tumor cells in peripheral blood of patients with metastatic breast cancer: A validation study of the cell search system,” Clinical Cancer Research, vol. 13, no. 3, pp. 920–928, Feb. 2007, doi: 10.1158/1078-0432.CCR-06-1695.

[134] Z. Miao, P. Moreno, N. Huang, I. Papatheodorou, A. Brazma, and S. A. Teichmann, “Putative cell type discovery from single-cell gene expression data,” Nat Methods, vol. 17, no. 6, pp. 621–628, Jun. 2020, doi: 10.1038/s41592-020-0825-9.

[135] C. L. Chen et al., “Single-cell analysis of circulating tumor cells identifies cumulative expression patterns of EMT-related genes in metastatic prostate cancer,” Prostate, vol. 73, no. 8, pp. 813–826, Jun. 2013, doi: 10.1002/pros.22625.

Chapter 4 Solid-State 3D- Printed $CsPbX_3$ perovskite color conversion layers for tunable emission for use in fluorescence imaging of stained cancer cells

4.1 Abstract

Because of their high photoluminescence quantum yield (PLQY), adjustable and band gap energy, and earth-abundant materials, inorganic metal halide-based perovskites (MHP) have a great deal of potential for use in solid-state lighting. Nonetheless, the problem with stability is still present. Here, we describe how to construct resin-perovskite color conversion layers using a 3D printing process to close the gap between material development and device applications. This resulted in a significant improvement in the device's performance while also simplifying the fabrication process. Green, yellow, and red color-emitting perovskite NCs were combined with a highly transparent UV resin to create a thin color conversion layer, which was then printed using an affordable 3D printer. After 180 days of storage in ambient circumstances, these 3D-printed color conversion layers still had more than 80% of their original PLQY, demonstrating their excellent stability. Additionally, we stacked the printed color conversion layers over the UV LED chip to create white lights with adjustable correlated color temperatures (CCT), high color rendering indices (CRI) up to 94, color coordinates that are close to neutral (0.32, 0.33), and high luminous efficacy of radiation (LER) up to 299 lm/W. This work will bring solid-state lighting usage on a larger scale one step closer to becoming a reality.

4.2 Introduction

4.2.1 Metal Halide Perovskites

Over the past ten years, metal halide perovskites (MHPs) [136]–[139] have emerged as a rising star in the field of optoelectronics. State-of-the-art optoelectronic technologies based on MHPs, including perovskite solar cells (PSCs) [139]–[142], light emitting diodes (LEDs), photodetectors (PDs) [137], [139], [143], and lasers, have been driving the prevailing paradigm. The crystalline structure of a perovskite material is the same as that of CaTiO3, and it has the chemical formula ABX3, where A is a cation with a large ionic radius, B is a metal cation, and X is an anion. Figure 4-1 illustrates the perovskite structure as an AX12 cuboctahedron with BX6 octahedral edges, which is the simplest way to describe it. In a typical ABX_3 perovskite, A is 12-fold cuboctahedra coordinated with X anions and occupies the interspace of the octahedral BX_6 framework, while B occupies the center of an octahedral $[BX_6]_4$ cluster, which creates corner-shared octahedral BX_6 framework.

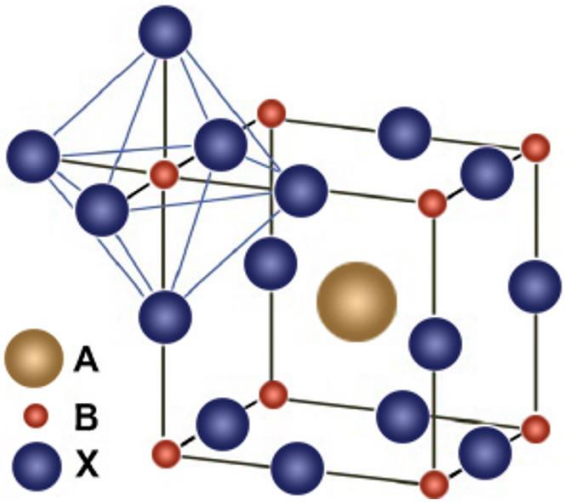

Figure 4-1. Structural representation of a ABX_3 Perovskites molecule

In terms of optoelectronic materials, the cesium lead halide perovskites ($CsPbX_3$, where X is Br, I) nanocrystals (NCs) are promising due to their superior photophysical characteristics and inexpensive manufacturing. By varying the size and composition, it has been shown that $CsPbX_3$ perovskite NCs have a high photoluminescence quantum yield (PLQY) [144]–[146] and a controllable emission range between 400 nm and 700 nm. They are perfect for making solid-state white light-emitting diodes since they can tune over the whole visible spectrum (LEDs). Figure 4-2 shows how MHP NCs are currently undergoing additional chemical engineering in relation to shape-controlled synthesis using various precursors and ligands, surface functionalization to induce additional functionality (for example, chirality), metal-ion doping, and search for Pb-free NCs alternatives, phase stability (thermal and moisture), and self-assembly [147]. These several avenues of investigation are all focused on enhancing and stabilizing their optical characteristics. There have been several great reviews written about MHP NCs over the

years, covering topics including their colloidal chemistry [148], optical properties (both linear and nonlinear), and prospective applications.

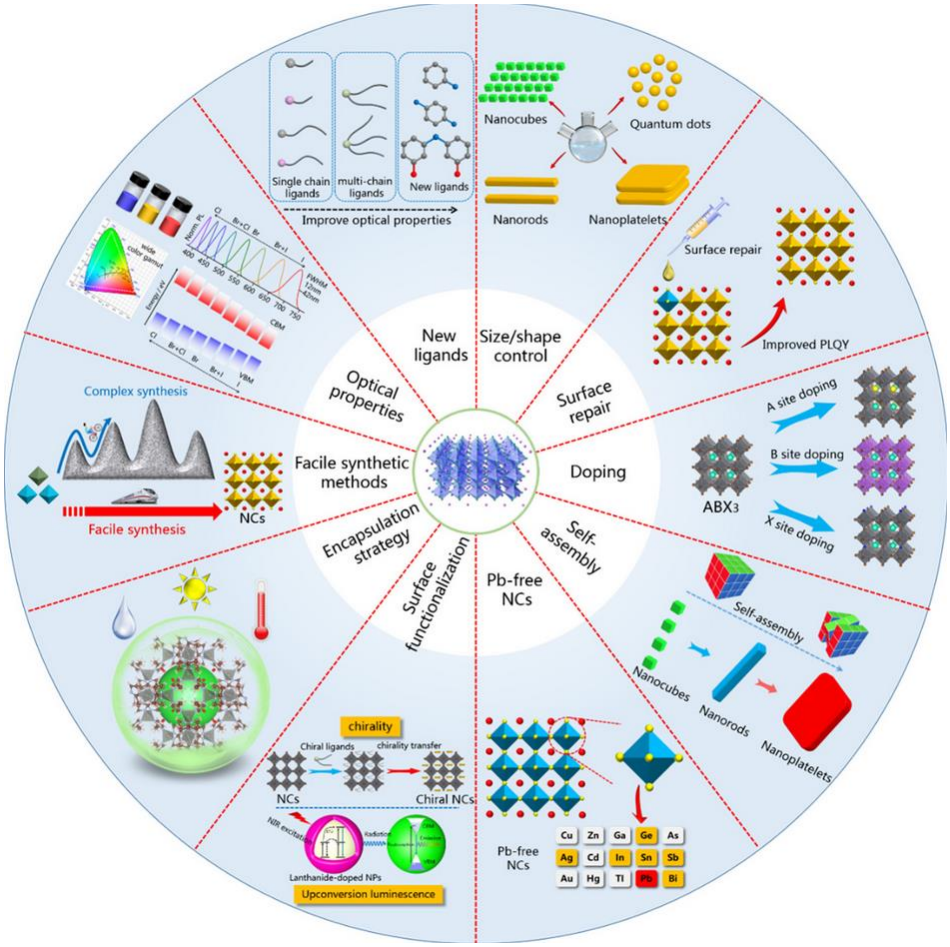

Figure 4-2. Overview of the current research topics on the chemistry of colloidal Metal-halide perovskites NCs in a schematic format.

Much effort has been put into creating simple and dependable synthesis methods for MHP NCs over the past few years. Based on the growth process, these strategies can be broadly categorized as either "bottom-up" or "top-down" approaches, as graphically represented in Figure 4-3. Based on the kind of synthesis, the bottom-up techniques can be further divided into three groups: (1) heat-up, (2) reprecipitation, and (3) in situ synthesis. HI and Ligand-assisted reprecipitation (LARP) [140], [149] have been the

most widely employed techniques for the synthesis of MHP NCs out of all the methodologies shown in Figure 4-3. Other reliable synthetic techniques were used to demonstrate the fabrication of the Cesium based specific $CsPbX_3$ perovskite NCs with control over their photoluminescence characteristics and high quantum yields. Hot injection (HI), supersaturated recrystallization, and anion exchange processes are a few of these techniques. These synthesis approaches have only found limited use because of the difficulty of the experimental setup and the high reagent and time consumption.

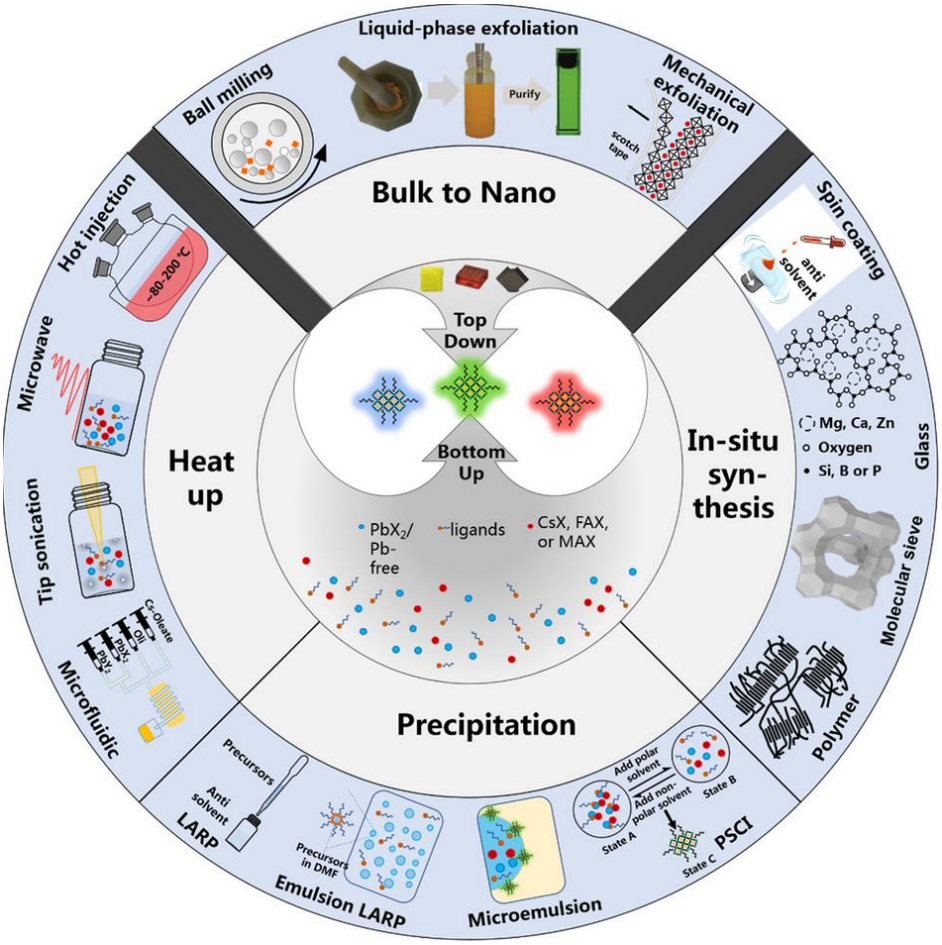

Figure 4-3. Overview diagram of several synthetic techniques used for Metal-halide perovskites NCs.

Our lab has recently shown that the saponification reprecipitation technique [150], [151] of synthesis at room temperature (RT) may be utilized to synthesize these structures

because of the creation of a simple, quick, real-time monitoring, and one-pot continuous system for the synthesis approach of $CsPbX_3$ NCs. However, the prospective uses of as-produced nanocrystals are limited by their long-term stability under various environmental conditions, such as air and moisture. The addition of lead thiocyanate [$Pb(SCN)_2$] has increased photoluminescence (PL) emission stability for up to a few weeks, but further work must be done to increase stability immediately in order to increase the appeal of these inexpensively synthesized NCs for device manufacturing. For lighting applications, researchers have used a variety of techniques, such as surface ligands, ligand cross-linking [152]–[154], and protective coatings [155], to preserve a stable structure of as-synthesized NCs. Because of the structural vulnerability of perovskite NCs, it is challenging to control the expansion of the coating layer on PNCs and the aggregation of NCs in response to ligand detachment. The creation of high-performance perovskites-polymers composites, such as those made of poly (methyl methacrylate) (PMMA), polystyrene (PS), epoxy, polyvinylpyrrolidone (PVP), and poly(dimethylsiloxane) (PDMS), is a significant step forward because it removes a significant barrier to the use of such materials in emerging technologies.

In a prior study, we found that UV resin [156] can extend the life of perovskite NCs without affecting their optical characteristics. Since then, we have been working to bridge the gap between material creation and device applications by creating a low-cost, large-scale methodology. The use of three-dimensional (3D) printing, also known as additive manufacturing, has increased over the past ten years and is now widespread in a number of industries, including the automotive, aerospace, dental, soft robotics, and medical sectors. The use of perovskite-based solid-state lighting will surely become more scalable

in the near future thanks to the clear resin and the high-speed 3D printing technology used here. Resin printing techniques are continuously being developed for designing lighting equipment [10], [57], [157], [158]. Although resin 3D printing technology is capable of producing stable, precise, and customizable designs with minimal material waste, the possibility of using the technology to build LED components, including the conversion layer, has not been investigated. The limitations associated with the listed NCs and the outstanding characteristics of the resin for a longer lifespan served as the driving forces behind our research. In this study, saponification-produced $CsPb(Br_xI_{1-x})_3$ ($0< x < 1$) NCs were combined with UV resin to make UV-$CsPb(Br_xI_{1-x})_3$ composites. Using a resin 3D printer, a color conversion layer was created for the first time. Figure 4-4 depicts the methods' specifics schematically. The process of saponification developed by our research team was used to create colloidal suspensions with great color purity and tunable emission from 448 nm to 639 nm, as illustrated in Figure 4-4.a .The NOVA3D ultra-clear resin was combined with the four different color-emitting NCs, especially the blue, green, yellow, and red-emitting NCs, to create the 3D printed structure. As demonstrated in Figure 4-4, the innovative printing method produces a thin, extremely transparent printed layer with a uniform distribution of NCs within it. As seen in Figure 4-4.c, white light emission was achieved by covering the UV LED chip with 3D-printed color conversion layers. The spectrum power distribution might be designed as illustrated in Figure 4-4.d by altering the layer thickness. Our test results show that these 3D printed objects maintained their luminescent characteristics throughout a six-month storage period in comparison to the similar colloidal solution. A UV LED chip and as-obtained color conversion layers were layered together to provide white light. The device's setup

produces white emission with tunable correlated color temperatures (CCT) [148], [159], [160] and a color rendering index (CRI) of up to 94. The color coordinates are near to those of neutral white light, which has the advantage of being better for vision.

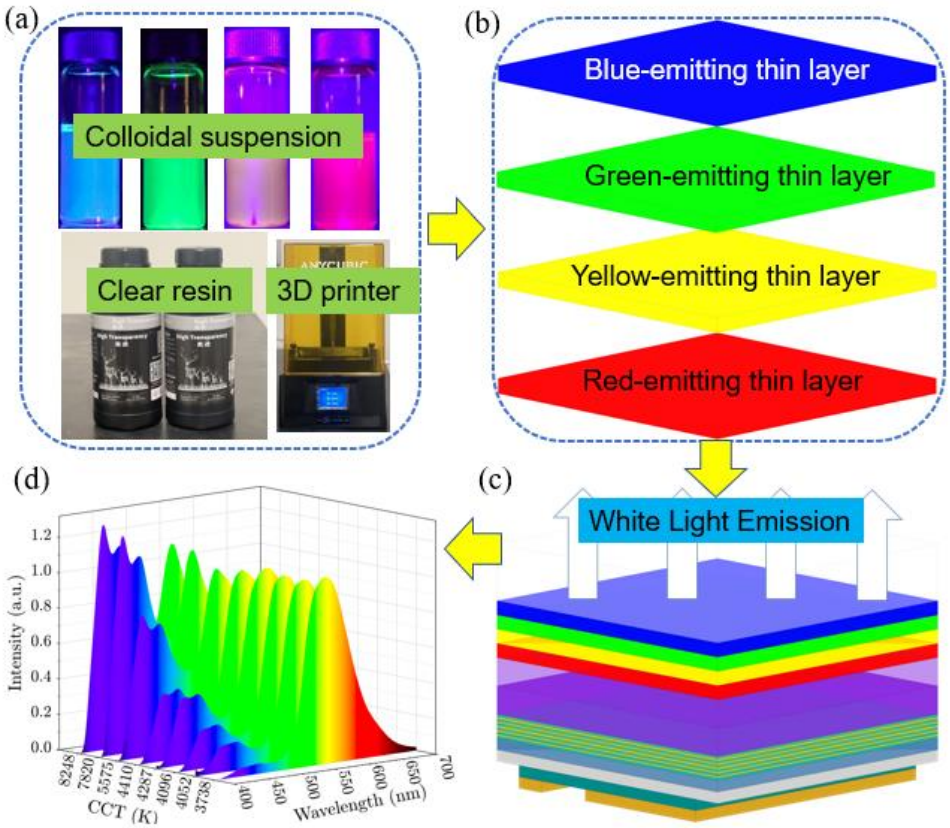

Figure 4-4. Overall process of device fabrication and testing

4.2.2 Resin based 3D Printing.

A resin 3D printer is a device that uses UV LED light beams to gradually solidify photosensitive liquid resin into a plastic 3D object while it is in a vat. Stereolithography, or SLA Figure 4-5.a, is the name of the technology, which can produce 3D prints with incredibly fine detail at a 0.01mm layer height. An ultraviolet (UV) laser is used in stereolithography, an additive manufacturing technique, to concentrate on a vat of

photopolymer resin. The UV laser is used to etch a pre-programmed pattern or shape into the surface of the photopolymer vat using computer-aided manufacturing (CAM) or computer-aided design (CAD) software. Due to the photopolymers' sensitivity to UV light, the resin is photochemically solidified and generates the desired 3D object in a single layer. The build platform is then lowered by one layer, and a blade applies resin to the tank's top once more. Until the 3D model is finished, this process is repeated for each layer of the design. The resin printer used here is Anycubic Photon MONO 4k Figure 4-5.b and it is an SLA based 3D printer that is capable of printing clear resin for the use in optoelectronics.

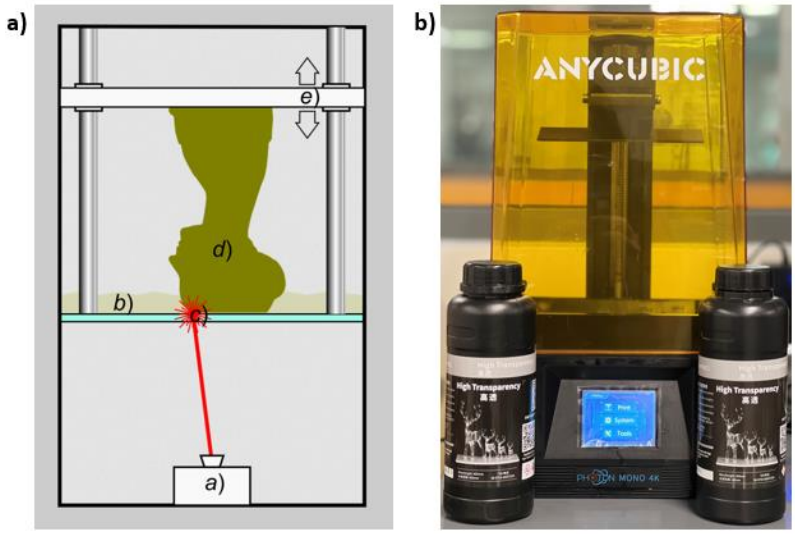

Figure 4-5. 3D printing overview a). SLA based printing process approach. b). Anycubic Photon MONO 4k Printer with clear resin.

4.2.3 Applications

Metal halide Perovskites have tunable bandgaps [161], high photoluminescent efficiency, ease of synthesis, great optical and electrical properties and larger binding energies has paved way into numerous applications. Some of the main applications are shown in Figure 4-6. MHP NCs are majorly used in solar cells, LED fabrication and research. The field involving Photodiode[162], phototransistor and photoconductors have been significantly researched using Metal halide perovskites to improve and replace the current semiconductor technologies for optical applications. Also, highly efficient lasers [161], [163] and X-ray detectors with the use of MHPs are being considered as an option for manufacturing.

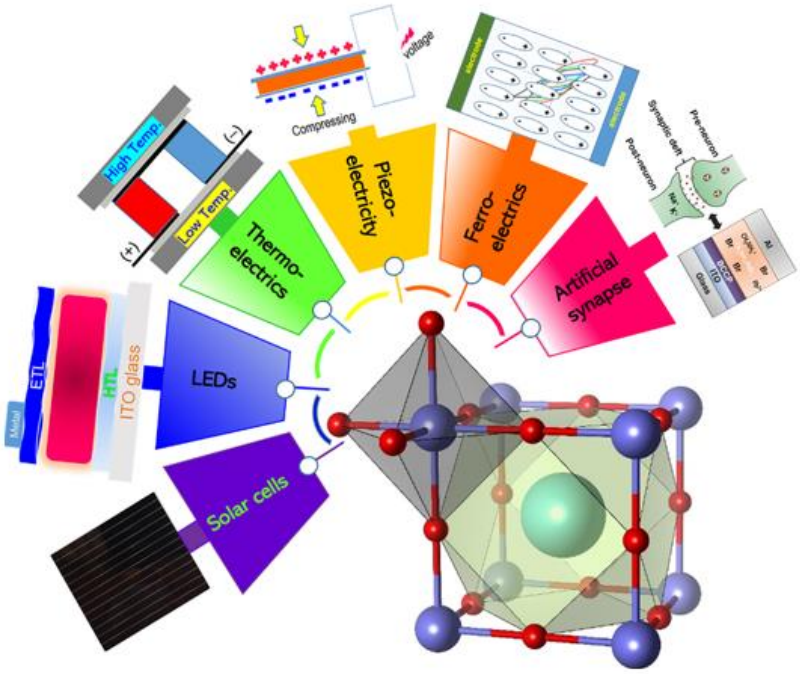

Figure 4-6. The vast applications of Perovskites materials[136]

4.3 Materials and Methods

4.3.1 Sample synthesis

4.3.1.1 Synthesis of CsPb $(B_xI_{1-x})_3$ NCs

As described in our prior work, this experiment used a saponification approach to create CsPb $(Br_xI_{1-x})_3$ (0< x< 1). By combining 0.735g of PbBr2 and 0.922g of PbI_2 into 5ml of Dimethylformamide (DMF), respectively, and stirring the mixture on a hot plate for 2.5 hours with a magnetic stirrer, the desired concentrations of $PbBr_2$ and PbI_2 were produced. By combining 0.2g of cesium hydroxide (CsOH), 433ul of glycerol trioleate (GTO), and 3ml of octadecene (ODE) with 30 minutes of hot plate mixing, the 0.4M Cs-Oleate precursor solution was created. 2.5 ml of ODE, 0.25 ml of oleic acid (OA), and 0.25 ml of Oleylamine (OLA) were combined and swirled at high speed for an additional minute before Cs-Oleate was added. Afterwards, 10 ml of acetone was added to the mixture to aid in NC nucleation. By varying the $PbBr_2/PbI_2$ ratios, tunable emission was made possible. All samples were centrifuged for 8 minutes at 5000 rpm to separate the supernatant from the aggregates. The aggregate is then stored and characterized while suspended in toluene.

4.3.1.2 Synthesis of $BaMgAl_{10}O_{17}:Eu^{2+}$ (BAM: Eu^{2+}) Phosphor

According to our earlier research, Eu_2O_3, Ba $(NO_3)_2$, $Mg(NO_3)_2.6.H_2O$, $Al(NO_3).9.H_2O$, and $C_6H_8O_7H_2O$ were the starting materials used to synthesis BAM:Eu2+ samples using

the sol-gel method.Eu_2O_3 was dissolved in a nitric solution to produce solutions containing europium nitrate. The metal nitrate was then dissolved in distilled water in a stoichiometric proportion. Citric acid ($C_6H_8O_7H_2O$) was weighed out and added to the nitrate solution. By setting the mole ratio of citric acid to metal ions to 1.5, a uniform, colorless solution was produced. The pH was changed to 5 to 6 and 30% ammonia was injected after three hours. At 110 °C, the solution's water gradual evaporation created a suspension of a dark metal citrate. Amorphous citrate gels with a high viscosity were created after an additional hour of heating, and they were calcined at 700° C for two hours in the air to eliminate any remaining organic matter. Under CO-reducing circumstances, calcined powder was heated for two hours at 1450°C.

4.3.2 Spectral Optimization

Four different materials that emit blue, green, yellow, and red light, respectively, were utilized to fabricate white LEDs in order to achieve white light emission. Then, spectral optimization was carried out to calculate the color quality, eyesight performance, and health consequences of white light. The following spectral power distributions (SPDs) were investigated to optimize color properties:

$$S_{total}(\lambda) = r_B \times S_B(\lambda) + r_G \times S_G(\lambda) + r_Y \times S_Y(\lambda) + r_R \times S_R(\lambda), \quad (1)$$

$$\text{With, } r_B = 0{:}0.05{:}2,\ r_G = 0{:}0.05{:}2,\ r_Y = 0{:}0.05{:}2,\ r_R = 0{:}0.05{:}2 \quad (2)$$

The ratios (B: G: Y: R) were calculated using the following equation:

$$(B{:}\ G{:}\ Y{:}\ R) = (r_B \times I_B){:}\ (r_G \times S_G){:}\ (r_Y \times S_Y){:}\ (r_R \times S_R) \quad (3)$$

Where I_B, I_G, I_Y, and I_R are the integrated intensities of corresponding SPDs of blue, green, yellow, and red. Four emission spectra with corresponding power ratios were initially considered during the optimization process. At the conclusion, 2825761 alternative spectral power distributions were found, with 41 options for each color spectrum. To assess color purity, vision performance, and light's impact on health, we calculated the CCT [148], [159], [160], CRI [148], [159], D_{uv} [160], luminous effectiveness of radiation (LER), and circadian action factor (CAF) of 2825761 distinct SPDs. Our earlier research provided a full explanation of the computation process.

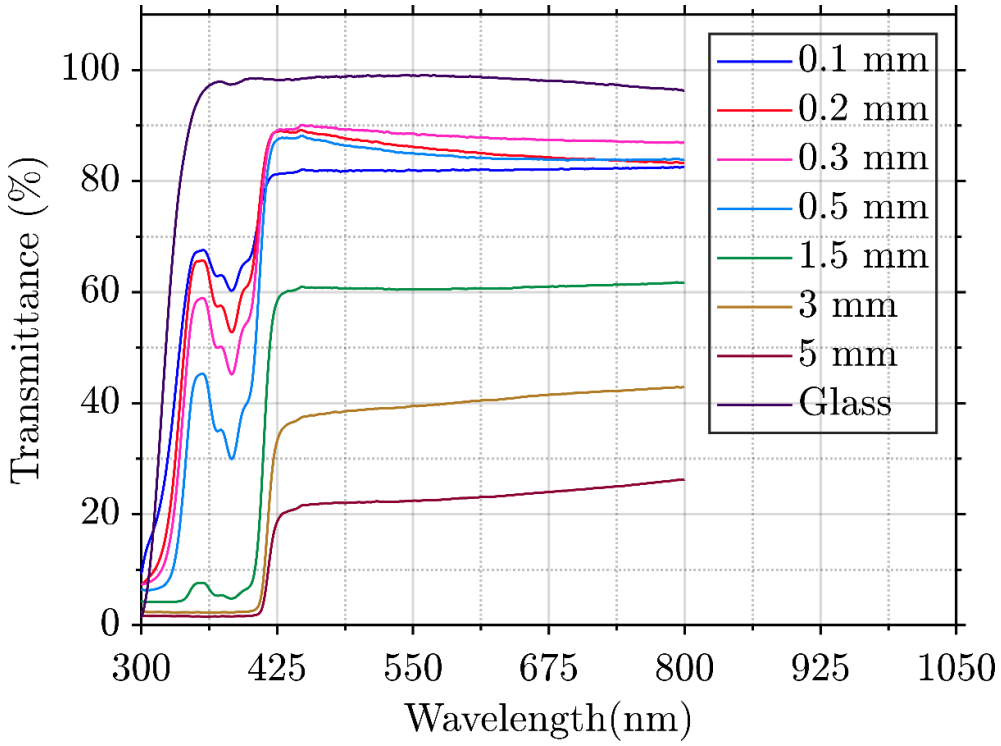

Figure 4-7. The transmission coefficient of 3D printed clear UV resin layers with various thicknesses and microscopic glass slides.

4.3.3 3D Printing Color conversion layers

The 3D models were built with Tinker CAD, and they were sliced with AnyCubic Photon Mono program. A format (PWMO) that is compatible with the Photon Mono 3D Printer was created from the STL files after they were exported to the Photon Workshop. Testing several resins revealed that printings made with Nova 3D high-transparency UV resin had the highest level of transparency. Figure 4-8.a compares the printed layers made with Nova 3D high transparency UV resin and Form labs clear resin. As we can see, the layer that was printed with Nova 3D high transparency UV resin has a higher degree of transparency. To create a layer with great transparency, it is crucial to choose the right resin type. The thickness of the layer has an impact on printing quality as well. According to Figure 4-8.b, the thick layer causes low transparency while the thin layer is curved and overly flimsy. As shown in Figure 4-7, the transmission coefficients of layers of varying thicknesses were measured and contrasted with those of microscopic glass slides [164]. With an increase in the printed layer's thickness, the transmission coefficient falls. In the end, a translucent clear resin that had been uniformly mixed with the synthesized nanocrystals was used to print a square sheet pattern that was 24 mm wide and 3 mm high. The early designs needed to be cured to solidify their surfaces.

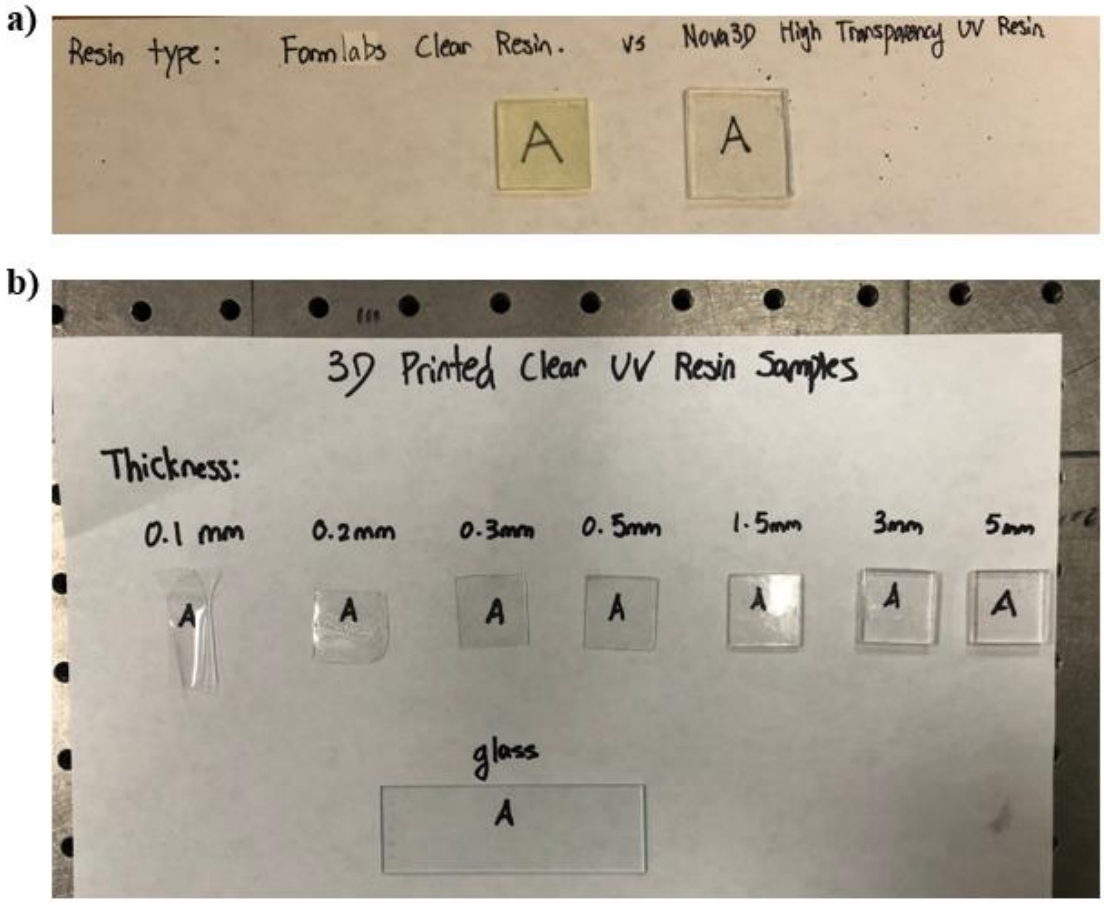

Figure 4-8. a) Photographs of printings using Form labs clear resin and using Nova 3D high transparency UV resin, (b) photographs of printings with different layer thicknesses: 0.1 mm, 0.2 mm, 0.3 mm, 0.5 mm, 1.5 mm, 3 mm, and 5 mm, and a microscopic glass slide.

4.3.4 Characterizations

The PL spectra were measured using a Shimadzu RF6000 Spectro fluorophotometer. A QE-pro spectrometer (QEP02037, Ocean Optics), an integrating sphere (819C-SF-6, Newport), and a 405nm laser source were used to measure the PLQYs. A QE-pro spectrometer (QEP02037, Ocean Optics) with a Keithley 2450 source meter running at 7.6 V and 7.9 mA under forward bias was used to capture EL spectra. By employing the

technique described in our earlier study, we were able to calculate the CIE coordinates, CRI, CCT, and LER.

4.4 Results and Discussion

4.4.1 Optical Properties of Perovskite NCs

Figure 4-9.a illustrates how changing the mix of halides can be used to modify the PL emission spectra. The entire visible spectrum is covered by the emission from perovskites, and when the molar ratio of I- to Br- increases, the emission peak location changes towards longer wavelengths. The lattice's capacity to be tuned is ascribed to the substitution of bigger I- ions for smaller Br- ions. The substitution action caused the lattice to expand, which raised NC dimensions, as demonstrated in our prior study. The variational influence of NCs' surface qualities can be used to confirm the emission spectrum's tunability. Calculating the halide mixed NCs' full width at half-maximum demonstrates that they emit narrow PL radiation (FWHM). With FWHMs between 24 and 48 nm, the NCs created in this study are excellent for lighting and display applications. The ratio of I- to Br- in the composition increases together with the FWHM. The non-radiative defect states inside the crystal structure are further controlled by the variation in FWHM, which in turn modifies the PLQY of the NCs. A smaller FWHM corresponds to a greater PLQY and fewer non-radiative defect states, and vice versa.

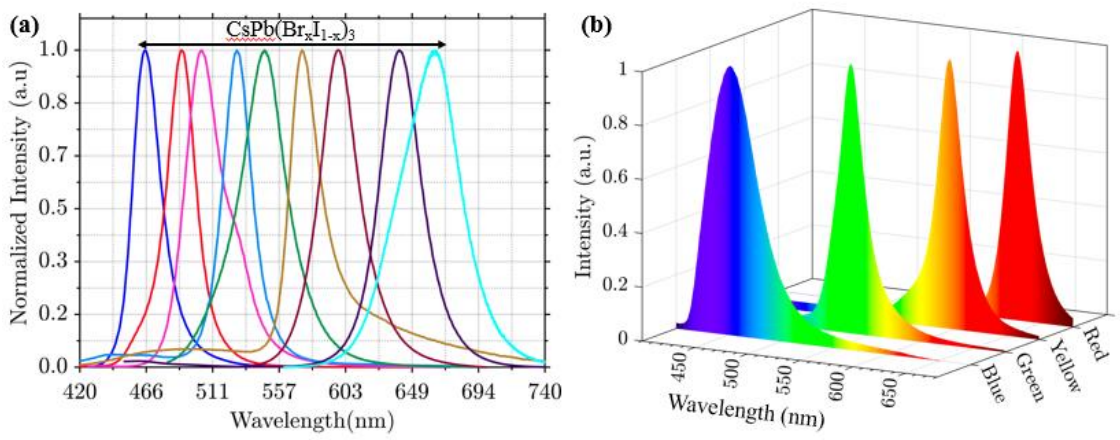

Figure 4-9. a). PL spectra CsPb (Br_xI_{1-x})$_3$ (x=0-1) with tunable emission, b). the blue emission from BAM: Eu, green, yellow, and red emission from perovskite nanocrystals selected for white LED fabrication.

4.4.2 Spectral Optimization

Perovskite NCs are particularly suited for white light applications because of their highly controllable emission. The spectral optimization of four different hues of NCs that emit light over the whole visible spectrum was done to create white LEDs. Figure 4-9.b displays the blue emission from BAM: Eu3+, the green, yellow, and red emission from CsPb (BrxI1-x) 3 NCs, each with emission peaks at wavelengths of 448 nm, 528 nm, 597.2 nm, and 639.2 nm. Figure 3 displays the results of the optimization. The CRI is displayed in the color bar. By mixing the blue emissions from BAM with the green, yellow, and red emissions from perovskites, a white light with an incredibly high CRI has been produced. Also, as seen in Figures 3(a), (b), and (c), the ratio of the total amount of blue and green emissions to the total amount of yellow and red emissions has a significant impact on CCT, CAF, and LER. The ratio causes the CCT and CAF to rise, but the LER to fall. The relationship between CCT, CAF, and LER in terms of their relationships with one another is depicted in Figures 3(d), (e), and (f). With an increase in

CAF, CCT increases, and with a rise in LER, CCT decreases. As CAF rises, there is a trend toward LER decline.

A higher ratio could result in a higher CCT [Figure 3. (a)], a higher CAF [Figure 3. (b)], and a lower LER [Figure 3. (c)]. By merely altering SPDs, white light with a tunable CCT might be produced, opening a wide range of applications. For instance, low CCT and CAF lighting is preferable in bedrooms as it encourages sleep; in contrast, high CCT and CAF lighting is appropriate for workspaces as it boosts productivity. The superior white light obtained here compared to the standard value is indicated by the high CRI value shown in Figure 3. Also, the narrow linewidth emission of color conversion layers can be linked to the comparatively high LER value, further demonstrating its great energy efficiency.

4.4.3 3D Printing of Color Conversion Layer and White LED Characterization

Poor atmospheric and thermal stability are characteristics of halide perovskites. To address this problem, we created a resin-based composite by combining $CsPb(Br_{1-x}I_x)_3$ NCs with clear resin. The specifics of the preparation are covered in the experimental section. Four separate color-emitting substances blue, green, yellow, and red that span sizeable portions of the visible spectrum are employed to make the composite. The mixing strategy results in a homogeneously dispersed, filmlike structure with good luminescent properties, as seen in the inset of Figure 4-10. Anycubic UV resin-printed models experience little shrinkage during photocuring, guaranteeing great precision and flawless surfaces. The build platform's scalability is demonstrated by the capacity to print numerous layers at once. Figure 4-10 displays the PL emission spectra of colloidal

suspensions of NCs and resin composites when illuminated by UV light. Insets of the figure show images of the suspensions when illuminated by UV light. The peak positions and FWHMs for these composites are displayed in Figure 4-10. With the exception of a slight variation in the peak position and FWHM, the PL emission profiles of NC colloidal suspension and resin-based composite are nearly identical, confirming NCs' compatibility with resin. Figure 4-10.a shows that the emission peak of BAM in powder form, which is 447.6, remains unaltered when combined with resin, demonstrating improved compatibility. The biggest shift in the PL peak is seen in red-emitting perovskites because of their greater sensitivity to iodine concentration (11 nm). The optical characteristics of NCs are mostly unaffected by the PL emission profile, peak position, and FWHM, therefore once integrated into the resin, the NCs will be shielded without suffering considerably from their optical characteristics.

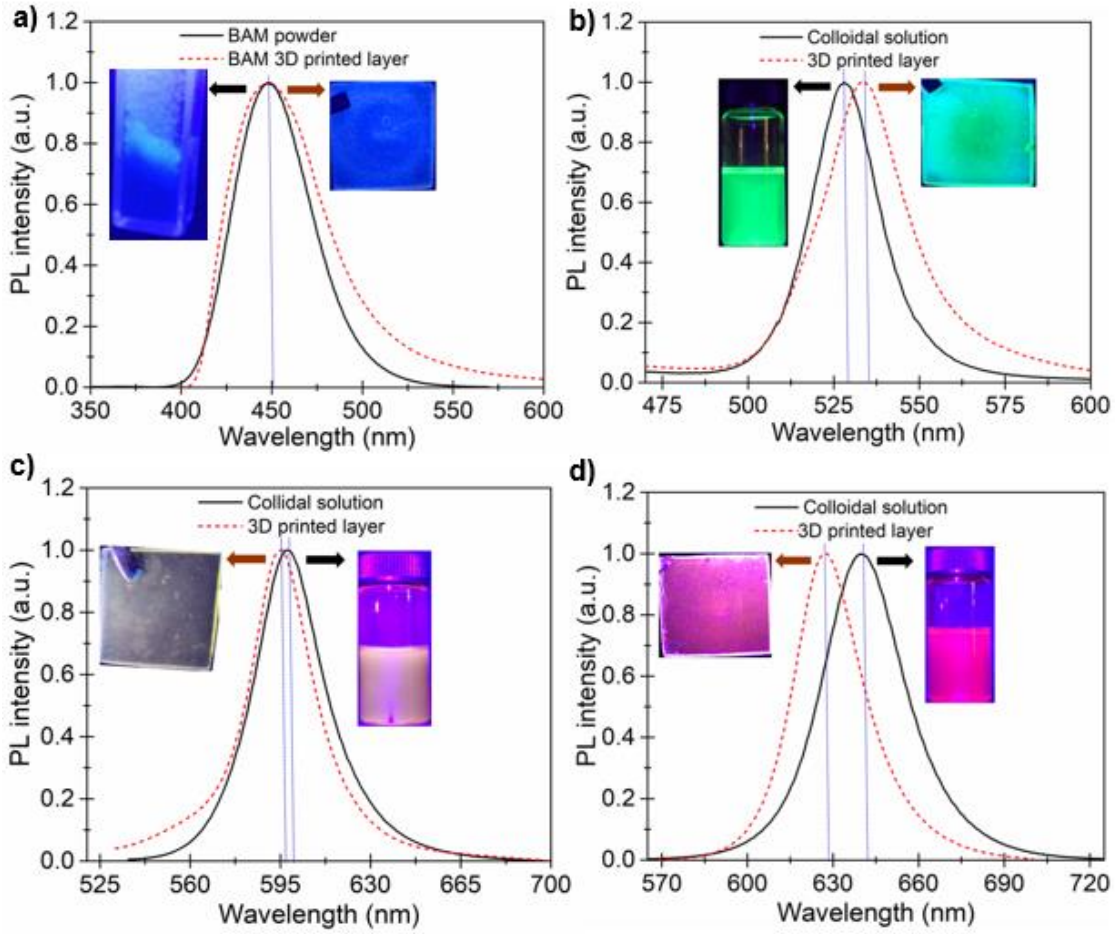

Figure 4-10. PL emission profiles of the different color emitting colloidal NCs and their resin-based composite.

We shall talk about resin's ability to protect various hues that emit NCs in the part that follows. ANYCUBIC photopolymer resin displays exceptional stability in wet and corrosive situations. This resin overcomes the limits of conventional resins, such as environmental corrosion and damp softening, because of its durability under a variety of climatic circumstances and ease of storage. Resin composites have been thoroughly studied to determine their potential for application in white light emission. We looked at the white light generated color quality, eyesight performance, and health impact to get to a trustworthy conclusion. As illustrated in Figure 4-11.a,b,c, the various color-emitting substances were consistently mixed with the transparent resin to create the separate color

conversion layers. Under a forward bias, the intense blue, green, and green emissions were seen. Thereafter, white LEDs were created by fusing UV LED chips with various color conversion layers. When optically pumped with a UV LED chip, the color conversion layers act as photon downconverters. To prevent the reabsorption problem, the red downconverters were positioned right above the UV LED chip, followed by the yellow, green, and blue emitters, in that order. The forward bias used to detect the bright white light is depicted in Figure 4-11.d. We adjusted the thickness ratios of four separate color conversion layers in order to design the CCT of white light. Figure 4-11.e displays the EL spectra of seven distinct white LEDs (designated as A, B, C, D, E, F, and G), each with a different CCT. These spectra were normalized by 620 nm emission. As the thickness ratios increase from the total of the blue and green color conversion layers to the sum of the yellow and red color conversion layers, the color temperature rises.

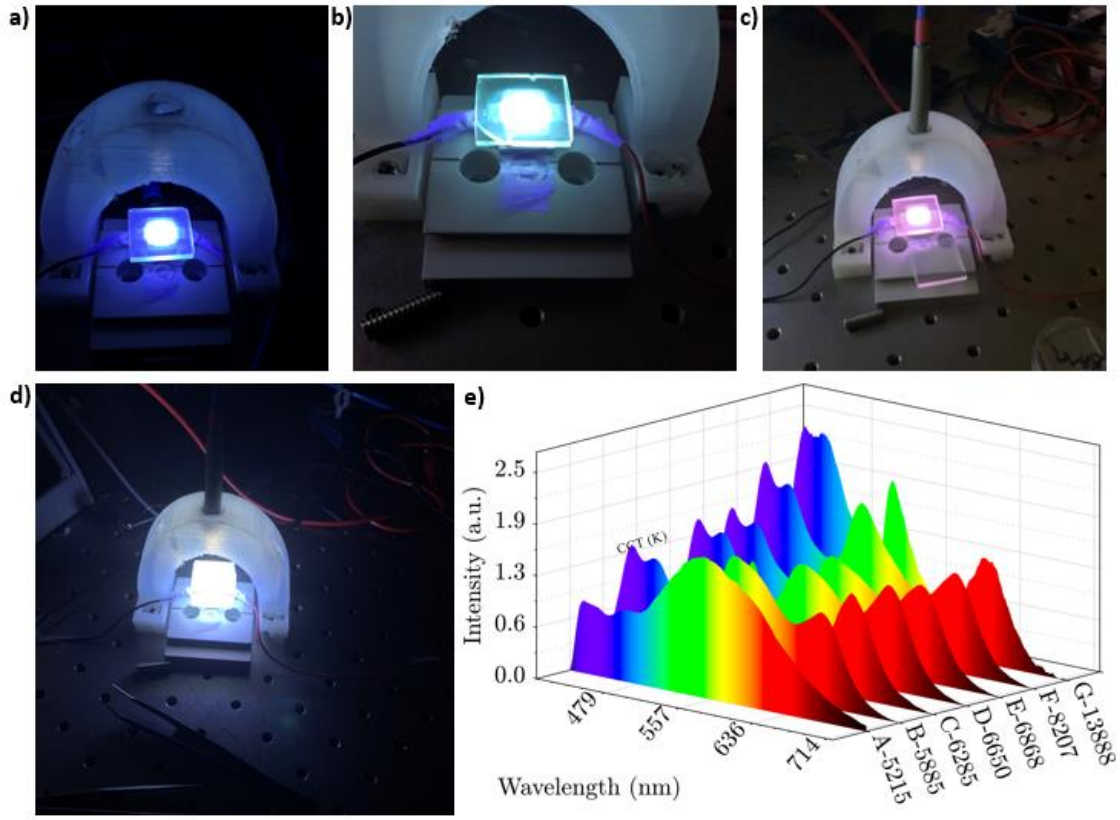

Figure 4-11. Electroluminescence measurements of a). Blue color conversion layer, b) Green color conversion layer, c) Red color conversion layer, d) white light emission. (e) Tunable emission from white LEDs with various CCTs.

4.4.4 Stability Test for the Conversion Layers

Perovskite composites' important properties for use in photovoltaic and optoelectronic devices include air stability and water resistance. The research of the NCs' stability toward ambient air and moisture is another crucial topic to evaluate its quality, as we have already highlighted how the instability of the metal halide PNCs hinders the commercial development of these materials. In order to test the PL stability of as-produced perovskite NC, we left it exposed to the atmosphere for three days without encapsulation. As shown in Figure 4-12 , we discovered that the intensity of the blue,

green, yellow, and red-emitting NCs significantly decreased over time. Under normal atmospheric conditions, CsPbBr3 NCs are quite unstable. The PL emission intensity of resin composites was monitored for 180 days (roughly six months) to determine how PLQY and peak positions changed when exposed to air and moisture. As can be seen in Figure 4-12 , the samples are noticeably more stable than bare NCs. This demonstrates one more thing that the NCs' lifespan can be extended using the resin utilized in this application. Figure 4-12.a, b, c shows the PL emission profile, which has a shorter line width and single-peak emission spectra. When evaluated after 180 days, the high-I-content perovskite composite exhibits a comparatively substantial blue shift in the peak location (about 6 months). We attributed this result to the perovskite NCs' ionization. Reactive etching causes perovskite to lose halide ions from its surface, which causes it to shrink and introduce more flaws. This causes the PL peak to quench and move to the blue. Accordingly, the increase in defect concentration in $CsPbBr_3$ NCs causes a significant decrease in its PLQY, which only retains 25% of its initial measurement, whereas the CsPbBr3 printed NCs exceptionally maintain above 80% of the initial PLQY after 180 days (roughly 6 months) of storage, as shown in Figure 4-12.d. The dynamic surface's constraint brought about by the removal of defect states vulnerable to the non-radiative recombination process is responsible for the increased performance and stability.

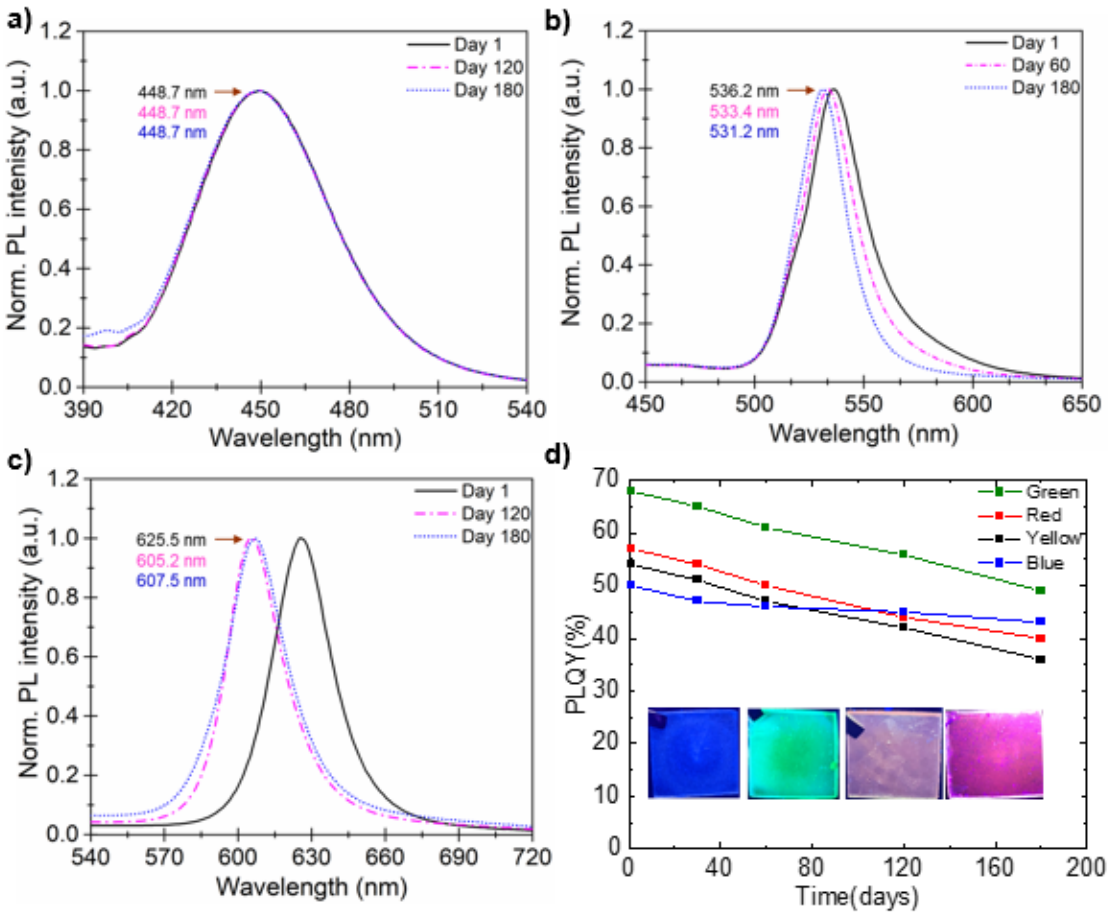

Figure 4-12. a), b), c) are time dependent PL emissions of blue, green, and red layers respectively. d). PLQY of all layers with time.

4.5 Conclusion and Future path

In conclusion, we created a process for making resin-based inorganic halide perovskite composites. By using this method, perovskites and polymers are created in a single reaction rather than having to go through the laborious separation and preparation of perovskites. These composites had very high PLQYs (>60%) and were highly luminous with good PL performance. It's also vital to observe how stable these composites are in the air. White LED technology using perovskite and resin composites has been

successfully demonstrated. The adoption of this strategy might result in a practical and affordable method for creating perovskite-resin composites, which might broaden the uses of perovskites in optoelectronic devices and transform lighting.

4.6 References

[10] H. Y. Jeong, E. Lee, S. C. An, Y. Lim, and Y. C. Jun, “3D and 4D printing for optics and metaphotonics,” Nanophotonics, vol. 9, no. 5. De Gruyter, pp. 1139–1160, May 01, 2020. doi: 10.1515/nanoph-2019-0483.

[57] J. Huang, B. Zhang, J. Xiao, and Q. Zhang, “An Approach to Improve the Resolution of DLP 3D Printing by Parallel Mechanism,” Applied Sciences (Switzerland), vol. 12, no. 24, Dec. 2022, doi: 10.3390/app122412905.

[136] S. Il Seok and T. F. Guo, “Halide perovskite materials and devices,” MRS Bull, vol. 45, no. 6, pp. 427–430, Jun. 2020, doi: 10.1557/mrs.2020.140.

[137] Y. Dong, Y. Zou, J. Song, X. Song, and H. Zeng, “Recent progress of metal halide perovskite photodetectors,” Journal of Materials Chemistry C, vol. 5, no. 44. Royal Society of Chemistry, pp. 11369–11394, 2017. doi: 10.1039/c7tc03612d.

[138] H. Dong, C. Ran, W. Gao, M. Li, Y. Xia, and W. Huang, “Metal Halide Perovskite for next-generation optoelectronics: progresses and prospects,” eLight, vol. 3, no. 1, Jan. 2023, doi: 10.1186/s43593-022-00033-z.

[139] C. H. Liao, M. A. Mahmud, and A. W. Y. Ho-Baillie, “Recent progress in layered metal halide perovskites for solar cells, photodetectors, and field-effect transistors,” Nanoscale, vol. 15, no. 9. Royal Society of Chemistry, pp. 4219–4235, Feb. 06, 2023. doi: 10.1039/d2nr06496k.

[140] S. Vijaya, J. Subbiah, D. J. Jones, and S. Anandan, “LARP-assisted synthesis of CsBi 3 I 10 perovskite for efficient lead-free solar cells,” RSC Adv, vol. 13, no. 15, pp. 9978–9982, 2023, doi: 10.1039/D3RA00365E.

[141] T. H. Han et al., “Perovskite-polymer composite cross-linker approach for highly-stable and efficient perovskite solar cells,” Nat Commun, vol. 10, no. 1, Dec. 2019, doi: 10.1038/s41467-019-08455-z.

[142] T. Yokoyama et al., “Overcoming Short-Circuit in Lead-Free CH3NH3SnI3 Perovskite Solar Cells via Kinetically Controlled Gas-Solid Reaction Film Fabrication Process,” Journal of Physical Chemistry Letters, vol. 7, no. 5, pp. 776–782, Mar. 2016, doi: 10.1021/acs.jpclett.6b00118.

[143] Y. Wang, M. L. Gao, J. L. Wu, and X. W. Zhang, “Metal halide perovskite photodetectors: Material features and device engineering,” Chinese Physics B, vol. 28, no. 1. Institute of Physics Publishing, 2019. doi: 10.1088/1674-1056/28/1/018502.

[144] I. Poli, G. W. Kim, E. L. Wong, A. Treglia, G. Folpini, and A. Petrozza, “High External Photoluminescence Quantum Yield in Tin Halide Perovskite Thin Films,” ACS Energy Lett, vol. 6, no. 2, pp. 609–611, Feb. 2021, doi: 10.1021/acsenergylett.0c02612.

[145] S. Jung et al., “Enhancement of Photoluminescence Quantum Yield and Stability in CsPbBr3 Perovskite Quantum Dots by Trivalent Doping,” Nanomaterials, vol. 10, no. 4, Apr. 2020, doi: 10.3390/nano10040710.

[146] M. G. La-Placa, G. Longo, A. Babaei, L. Martínez-Sarti, M. Sessolo, and H. J. Bolink, “Photoluminescence quantum yield exceeding 80% in low dimensional perovskite thin-films: Via passivation control,” Chemical Communications, vol. 53, no. 62, pp. 8707–8710, 2017, doi: 10.1039/c7cc04149g.

[147] M. Kafetzi, S. Pispas, and G. Mousdis, “Hybrid perovskite/polymer materials: Preparation and physicochemical properties,” Journal of Composites Science, vol. 5, no. 11, Nov. 2021, doi: 10.3390/jcs5110304.

[148] C.-F. Lai, C.-C. Chang, M.-J. Wang, and M.-K. Wu, “CCT- and CRI-tuning of white light-emitting diodes using three-dimensional non-close-packed colloidal photonic crystals with photonic stop-bands,” Opt Express, vol. 21, no. S4, p. A687, Jul. 2013, doi: 10.1364/oe.21.00a687.

[149] S. Vijaya, J. Subbiah, D. J. Jones, and S. Anandan, “LARP-assisted synthesis of CsBi 3 I 10 perovskite for efficient lead-free solar cells,” RSC Adv, vol. 13, no. 15, pp. 9978–9982, 2023, doi: 10.1039/D3RA00365E.

[150] G. C. Adhikari, P. A. Vargas, H. Zhu, and P. Zhu, “Saponification Precipitation Method for CsPbBr 3 Nanocrystals with Blue-Green Tunable Emission,” Journal of Physical Chemistry C, vol. 123, no. 2, pp. 1406–1412, Jan. 2019, doi: 10.1021/acs.jpcc.8b10636.

[151] S. Thapa, G. C. Adhikari, H. Zhu, and P. Zhu, “Blue-red color-tunable all-inorganic bromide–iodide mixed-halide perovskite nanocrystals using the saponification technique for white-light-emitting diodes,” Journal of the Optical Society of America B, vol. 36, no. 6, p. 1616, Jun. 2019, doi: 10.1364/josab.36.001616.

[152] D. Liu et al., “Direct optical patterning of perovskite nanocrystals with ligand cross-linkers,” 2022. [Online]. Available: https://www.science.org

[153] D. Liu et al., “Direct optical patterning of perovskite nanocrystals with ligand cross-linkers,” 2022. [Online]. Available: https://www.science.org

[154] A. H. Proppe, M. Wei, B. Chen, R. Quintero-Bermudez, S. O. Kelley, and E. H. Sargent, “Photochemically Cross-Linked Quantum Well Ligands for 2D/3D Perovskite Photovoltaics with Improved Photovoltage and Stability,” J Am Chem Soc, vol. 141, no. 36, pp. 14180–14189, Sep. 2019, doi: 10.1021/jacs.9b05083.

[155] H. Xiao et al., “Polymer ligands induced remarkable spectral shifts in all-inorganic lead halide perovskite nanocrystals,” J Mater Chem C Mater, vol. 8, no. 29, pp. 9968–9974, Aug. 2020, doi: 10.1039/d0tc01822h.

[156] W. Peng and B. Riedl, “Thermosetting Resins,” UTC, 1995. [Online]. Available: https://pubs.acs.org/sharingguidelines

[157] D. Ahn, L. M. Stevens, K. Zhou, and Z. A. Page, “Rapid High-Resolution Visible Light 3D Printing,” ACS Cent Sci, vol. 6, no. 9, pp. 1555–1563, Sep. 2020, doi: 10.1021/acscentsci.0c00929.

[158] H. Quan, T. Zhang, H. Xu, S. Luo, J. Nie, and X. Zhu, “Photo-curing 3D printing technique and its challenges,” Bioactive Materials, vol. 5, no. 1. KeAi Communications Co., pp. 110–115, Mar. 01, 2020. doi: 10.1016/j.bioactmat.2019.12.003.

[159] J. Jargus, J. Vitasek, J. Nedoma, V. Vasinek, and R. Martinek, “Effect of selected luminescent layers on CCT, CRI, and response times,” Materials, vol. 12, no. 13, Jul. 2019, doi: 10.3390/ma12132095.

[160] Y. Ohno, “Calculation of CCT and Duv and Practical Conversion Formulae.”

[161] T. S. Kao, Y. H. Hong, K. Bin Hong, and T. C. Lu, “Perovskite random lasers: A tunable coherent light source for emerging applications,” Nanotechnology, vol. 32, no. 28. IOP Publishing Ltd, Jul. 09, 2021. doi: 10.1088/1361-6528/abe907.

[162] J. Yao, L. Xu, S. Wang, and J. Song, “Metal halide perovskites-based white light-emitting diodes,” JPhys Photonics, vol. 4, no. 4. Institute of Physics, Oct. 01, 2022. doi: 10.1088/2515-7647/ac91b7.

[163] W. Sun et al., “Lead halide perovskite vortex microlasers,” Nat Commun, vol. 11, no. 1, Dec. 2020, doi: 10.1038/s41467-020-18669-1.

[164] D. A. Barcelos, D. C. Leitao, L. C. J. Pereira, and M. C. Gonçalves, “What is driving the growth of inorganic glass in smart materials and opto-electronic devices?,” Materials, vol. 14, no. 11. MDPI AG, Jun. 01, 2021. doi: 10.3390/ma14112926

Chapter 5 Summaries and Conclusions

5.1 Summaries and Conclusions

Over the past few decades, research and development on microfluidic devices, also referred to as lab-on-a-chip systems or microfluidic total analysis systems (TAS), have advanced quickly. There aren't many commercial success stories for microfluidic devices, despite the many advantages they offer, including improved analytical performance, decreased sample and reagent usage, and reduced device footprint in the biomedical disciplines. Utilizing multipurpose microposts, a novel and distinctive microfluidic isolation technique has been successfully demonstrated. In tests using microbeads and human blood infused with cancer cells, the platform showed high capture efficiency at rapid flow rates without clogging issues.

Our technology used a unique size-based cell capturing unit in conjunction with a microfluidic method in order to isolate significantly larger tumor cells from biological fluids. While the sample flow rate through the device as a whole was high, it was essential to maintain a low fluid movement velocity at the capture site in order to retain the captured cell and keep the shear stress on the cells to an absolute minimum. The device was characterized by the usage of both microbeads and A549 human lung cancer cells. The ability to characterize rare cells from bodily fluids (liquid biopsies) is a crucial step in biomedical investigations for retaining cell integrity and recovering cells for further testing. We employed a small number of cancer cells for routine testing, which reflects the clinical situation in cancer patients who normally have few CTCs in their blood. The clinical setting parameters employed such as use of blood as fluid medium,

lower cancer cell to begin with, all provided excellent capture rate stabilized the motivation to go forward with actual patient blood samples.

PDMS is currently a typical biological substance used in microfluidic devices for medical applications. We also explored the applications of PDMS in medicine and looked at how it interacts with blood cells and cancer cells to show how important it is for both the present and the future of biomedicine. Cell culture is at a crucial stage for current medical, biological, and pharmacological research. Culture methods used in modern laboratories have been refined over a century of research. As a result, we can claim with confidence that the device described here, which is made of a variety of materials including PDMS, PTFE, and glass slides, is biologically compatible with all cell types used and has been proven by a variety of methods such as cell culture, efficacy of CfDNA and EVs which came in contact with the device. It must be emphasized, nonetheless, that additional research is necessary before standardizing and marketing this patented equipment for use in clinical studies. Utilizing a tool like TumorTrap in research lab settings for alternative cell line analysis could provide more information and help significantly with the commercialization process.

Furthermore, we synthesized, fabricated, and characterized perovskite compounds with an ability to tune the emission wavelength that has significant applications in the field of fluorescence imaging of stained cancer cells for easier identification. We developed a method for producing resin-based inorganic halide perovskite composites, to sum up. Instead of going through the time-consuming separation and preparation of perovskites, this approach creates perovskites and polymers in a single reaction. These composites were highly bright with good PL performance and very high PLQYs (>60%). The

stability of these composites in the air must also be carefully monitored. Perovskite and resin composites have been effectively used in white LED technology demonstrations. Adopting this approach could lead to a workable and affordable technique for producing perovskite-resin composites, which could expand the applications of perovskites in optoelectronic devices and revolutionize lighting and fluorescence imaging.

Be it the microfluidic device and/or the tunable perovskite, one thing for sure is the wide application possibilities in the field of Biomedical diagnostics and imaging. New materials, portable design, characterization techniques, and fabrication methods can all be developed in the subject of miniaturization. Last but not least, there is the potential for leveraging this technology to create a point-of-care hybrid microfluidic device that could identify rare cancer cells from a simple blood draw rather than a risky tissue biopsy. In conclusion, the work conducted in this dissertation helps to introduce a new wave of low-cost fabrication methods, which advances the field of microfluidics. These fabrication methods can be easily scaled up to accommodate mass production as well as rapid prototyping and small-scale manufacture in academic research labs.

Chapter 6 References

[1] E. A. Flores-Contreras, R. B. González-González, I. P. Rodríguez-Sánchez, J. F. Yee-De León, H. M. N. Iqbal, and E. González-González, "Microfluidics-Based Biosensing Platforms: Emerging Frontiers in Point-of-Care Testing SARS-CoV-2 and Seroprevalence," *Biosensors*, vol. 12, no. 3. MDPI, Mar. 01, 2022. doi: 10.3390/bios12030179.

[2] X. Xiong, L. Zhang, J. Hu, and L. Hmurcik, "Introducing the small world-developing MEMS/nanotechnology curriculum," in *ASEE Annual Conference and Exposition, Conference Proceedings*, American Society for Engineering Education, 2009. doi: 10.18260/1-2--4555.

[3] S. Torino, B. Corrado, M. Iodice, and G. Coppola, "Pdms-based microfluidic devices for cell culture," *Inventions*, vol. 3, no. 3. MDPI Multidisciplinary Digital Publishing Institute, Sep. 01, 2018. doi: 10.3390/inventions3030065.

[4] K. Raj M and S. Chakraborty, "PDMS microfluidics: A mini review," *Journal of Applied Polymer Science*, vol. 137, no. 27. John Wiley and Sons Inc., Jul. 15, 2020. doi: 10.1002/app.48958.

[5] L. Lin and C. K. Chung, "PDMS microfabrication and design for microfluidics and sustainable energy application: Review," *Micromachines*, vol. 12, no. 11. MDPI, Nov. 01, 2021. doi: 10.3390/mi12111350.

[6] M. I. Khot *et al.*, "Characterising a PDMS based 3D cell culturing microfluidic platform for screening chemotherapeutic drug cytotoxic activity," *Sci Rep*, vol. 10, no. 1, Dec. 2020, doi: 10.1038/s41598-020-72952-1.

[7] S. Nishat, A. T. Jafry, A. W. Martinez, and F. R. Awan, “Paper-based microfluidics: Simplified fabrication and assay methods,” *Sens Actuators B Chem*, vol. 336, Jun. 2021, doi: 10.1016/j.snb.2021.129681.

[8] H. M. Ji, V. Samper, Y. Chen, C. K. Heng, T. M. Lim, and L. Yobas, “Silicon-based microfilters for whole blood cell separation,” *Biomed Microdevices*, vol. 10, no. 2, pp. 251–257, Apr. 2008, doi: 10.1007/s10544-007-9131-x.

[9] S. Razavi Bazaz *et al.*, “3D Printing of Inertial Microfluidic Devices,” *Sci Rep*, vol. 10, no. 1, Dec. 2020, doi: 10.1038/s41598-020-62569-9.

[10] H. Y. Jeong, E. Lee, S. C. An, Y. Lim, and Y. C. Jun, “3D and 4D printing for optics and metaphotonics,” *Nanophotonics*, vol. 9, no. 5. De Gruyter, pp. 1139–1160, May 01, 2020. doi: 10.1515/nanoph-2019-0483.

[11] A. Shakeri, N. A. Jarad, S. Khan, and T. F Didar, “Bio-functionalization of microfluidic platforms made of thermoplastic materials: A review,” *Analytica Chimica Acta*, vol. 1209. Elsevier B.V., May 29, 2022. doi: 10.1016/j.aca.2021.339283.

[12] Y. Chen, “ii PATTERNING ELASTOMER, THERMOPLASTICS AND SHAPE MEMORY MATERIAL BY UVO LITHOGRAPHY AND SOFT LITHOGRAPHY.”

[13] K. Ren, J. Zhou, and H. Wu, “Materials for microfluidic chip fabrication,” *Acc Chem Res*, vol. 46, no. 11, pp. 2396–2406, Nov. 2013, doi: 10.1021/ar300314s.

[14] P. N. Nge, C. I. Rogers, and A. T. Woolley, “Advances in microfluidic materials, functions, integration, and applications,” *Chemical Reviews*, vol. 113, no. 4. pp. 2550–2583, Apr. 10, 2013. doi: 10.1021/cr300337x.

[15] S. M. Scott and Z. Ali, “Fabrication methods for microfluidic devices: An overview,” *Micromachines*, vol. 12, no. 3. MDPI AG, Mar. 01, 2021. doi: 10.3390/mi12030319.

[16] C. W. Tsao, “Polymer microfluidics: Simple, low-cost fabrication process bridging academic lab research to commercialized production,” *Micromachines*, vol. 7, no. 12. MDPI AG, 2016. doi: 10.3390/mi7120225.

[17] J. Friend and L. Yeo, “Fabrication of microfluidic devices using polydimethylsiloxane,” *Biomicrofluidics*, vol. 4, no. 2, 2010, doi: 10.1063/1.3259624.

[18] B. Wang, Y. Wang, S. Du, J. Zhu, and S. Ma, “Upcycling of thermosetting polymers into high-value materials,” *Materials Horizons*, vol. 10, no. 1. Royal Society of Chemistry, pp. 41–51, Oct. 26, 2022. doi: 10.1039/d2mh01128j.

[19] X. Li, D. R. Ballerini, and W. Shen, “A perspective on paper-based microfluidics: Current status and future trends,” *Biomicrofluidics*, vol. 6, no. 1. American Institute of Physics Inc., Mar. 02, 2012. doi: 10.1063/1.3687398.

[20] L. Yu and Z. Z. Shi, “Microfluidic paper-based analytical devices fabricated by low-cost photolithography and embossing of Parafilm®,” *Lab Chip*, vol. 15, no. 7, pp. 1642–1645, Apr. 2015, doi: 10.1039/c5lc00044k.

[21] H. Asano and Y. Shiraishi, “Development of paper-based microfluidic analytical device for iron assay using photomask printed with 3D printer for fabrication of hydrophilic and hydrophobic zones on paper by photolithography,” *Anal Chim Acta*, vol. 883, pp. 55–60, Jul. 2015, doi: 10.1016/j.aca.2015.04.014.

[22] C. M. Pandey *et al.*, “Microfluidics Based Point-of-Care Diagnostics,” *Biotechnology Journal*, vol. 13, no. 1. Wiley-VCH Verlag, Jan. 01, 2018. doi: 10.1002/biot.201700047.

[23] J. H. Nichols, “Utilizing point-of-care testing to optimize patient care.”

[24] M. Sonker, V. Sahore, and A. T. Woolley, “Recent advances in microfluidic sample preparation and separation techniques for molecular biomarker analysis: A critical review,” *Analytica Chimica Acta*, vol. 986. Elsevier B.V., pp. 1–11, Sep. 15, 2017. doi: 10.1016/j.aca.2017.07.043.

[25] M. Hill and E. Wagenaars, “Modelling of Plasma Temperatures and Densities in Laser Ablation Plumes of Different Metals,” *Photonics*, vol. 9, no. 12, Dec. 2022, doi: 10.3390/photonics9120937.

[26] J. Shi, Z. Wang, T. Zheng, X. Liu, B. Guo, and J. Xu, “Thermal and UV light adaptive polyurethane elastomers for photolithography-transfer printing of flexible circuits,” *Mater Horiz*, vol. 9, no. 12, pp. 3070–3077, Oct. 2022, doi: 10.1039/d2mh01005d.

[27] S. Paik *et al.*, “Near-field sub-diffraction photolithography with an elastomeric photomask,” *Nat Commun*, vol. 11, no. 1, Dec. 2020, doi: 10.1038/s41467-020-14439-1.

[28] J. Wu *et al.*, “Parallel near-field photolithography with metal-coated elastomeric masks,” *Langmuir*, vol. 31, no. 3, pp. 1210–1217, Jan. 2015, doi: 10.1021/la504260x.

[29] A. Karimi, S. Yazdi, and A. M. Ardekani, “Hydrodynamic mechanisms of cell and particle trapping in microfluidics,” *Biomicrofluidics*, vol. 7, no. 2, Apr. 2013, doi: 10.1063/1.4799787.

[30] R. Ozawa, H. Iwadate, H. Toyoda, M. Yamada, and M. Seki, “A numbering-up strategy of hydrodynamic microfluidic filters for continuous-flow high-throughput cell sorting,” *Lab Chip*, vol. 19, no. 10, pp. 1828–1837, May 2019, doi: 10.1039/c9lc00053d.

[31] M. E. Warkiani, A. K. P. Tay, G. Guan, and J. Han, “Membrane-less microfiltration using inertial microfluidics,” *Sci Rep*, vol. 5, Jul. 2015, doi: 10.1038/srep11018.

[32] N. Herrmann, P. Neubauer, and M. Birkholz, “Spiral microfluidic devices for cell separation and sorting in bioprocesses,” *Biomicrofluidics*, vol. 13, no. 6. American Institute of Physics Inc., Nov. 01, 2019. doi: 10.1063/1.5125264.

[33] J. Sun *et al.*, “Double spiral microchannel for label-free tumor cell separation and enrichment.,” *Lab Chip*, vol. 12, no. 20, pp. 3952–3960, 2012, doi: 10.1039/c2lc40679a.

[34] A. Hochstetter *et al.*, “Deterministic Lateral Displacement: Challenges and Perspectives,” *ACS Nano*, vol. 14, no. 9. American Chemical Society, pp. 10784–10795, Sep. 22, 2020. doi: 10.1021/acsnano.0c05186.

[35] J. McGrath, M. Jimenez, and H. Bridle, “Deterministic lateral displacement for particle separation: A review,” *Lab on a Chip*, vol. 14, no. 21. Royal Society of Chemistry, pp. 4139–4158, Nov. 07, 2014. doi: 10.1039/c4lc00939h.

[36] T. Salafi, Y. Zhang, and Y. Zhang, “A Review on Deterministic Lateral Displacement for Particle Separation and Detection,” *Nano-Micro Letters*, vol. 11, no. 1. SpringerOpen, Dec. 01, 2019. doi: 10.1007/s40820-019-0308-7.

[37] K. T. Knizner, R. R. Kibbe, K. P. Garrard, J. R. Nuñez, C. R. Anderton, and D. C. Muddiman, “On the importance of color in mass spectrometry imaging,” *Journal of Mass Spectrometry*, vol. 57, no. 12, Dec. 2022, doi: 10.1002/jms.4898.

[38] M. F. Wang, A. N. Joignant, A. L. Sohn, K. P. Garrard, and D. C. Muddiman, “Time of acquisition and high spatial resolution mass spectrometry imaging,” *Journal of Mass Spectrometry*, vol. 58, no. 3, Mar. 2023, doi: 10.1002/jms.4911.

[39] M. J. Moore, J. A. Sebastian, and M. C. Kolios, “Determination of cell nucleus-to-cytoplasmic ratio using imaging flow cytometry and a combined ultrasound and photoacoustic technique: a comparison study,” *J Biomed Opt*, vol. 24, no. 10, p. 1, Oct. 2019, doi: 10.1117/1.jbo.24.10.106502.

[40] X. Gao *et al.*, “Piezoelectric Actuators and Motors: Materials, Designs, and Applications,” *Advanced Materials Technologies*, vol. 5, no. 1. Wiley-Blackwell, Jan. 01, 2020. doi: 10.1002/admt.201900716.

[41] A. Aabid, M. Hrairi, S. J. Mohamed Ali, and Y. E. Ibrahim, “Review of Piezoelectric Actuator Applications in Damaged Structures: Challenges and Opportunities,” *ACS Omega*, 2022, doi: 10.1021/acsomega.2c06573.

[42] S. Mohith, A. R. Upadhya, K. P. Navin, S. M. Kulkarni, and M. Rao, “Recent trends in piezoelectric actuators for precision motion and their applications: a review,” *Smart Materials and Structures*, vol. 30, no. 1. IOP Publishing Ltd, Jan. 01, 2021. doi: 10.1088/1361-665X/abc6b9.

[43] K. Chen, H. Lu, M. Sun, L. Zhu, and Y. Cui, “Mixing enhancement of a novel C-SAR microfluidic mixer,” *Chemical Engineering Research and Design*, vol. 132, pp. 338–345, Apr. 2018, doi: 10.1016/j.cherd.2018.01.032.

[44] C. Y. Lee, C. L. Chang, Y. N. Wang, and L. M. Fu, “Microfluidic mixing: A review,” *International Journal of Molecular Sciences*, vol. 12, no. 5. pp. 3263–3287, May 2011. doi: 10.3390/ijms12053263.

[45] F. Jiang, K. S. Drese, S. Hardt, M. Küpper, and F. Schönfeld, “Helical flows and chaotic mixing in curved micro channels,” *AIChE Journal*, vol. 50, no. 9, pp. 2297–2305, Sep. 2004, doi: 10.1002/aic.10188.

[46] W. S. Low, N. A. Kadri, and W. A. B. Bin Wan Abas, “Computational fluid dynamics modelling of microfluidic channel for dielectrophoretic biomems application,” *Scientific World Journal*, vol. 2014, 2014, doi: 10.1155/2014/961301.

[47] G. R. Pesch and F. Du, “A review of dielectrophoretic separation and classification of non-biological particles,” *Electrophoresis*, vol. 42, no. 1–2. Wiley-VCH Verlag, pp. 134–152, Jan. 01, 2021. doi: 10.1002/elps.202000137.

[48] P. E. Thiriet, J. Pezoldt, G. Gambardella, K. Keim, B. Depla, and C. Guiducci, “Selective retrieval of individual cells from microfluidic arrays combining dielectrophoretic force and directed hydrodynamic flow,” *Micromachines (Basel)*, vol. 11, no. 3, Mar. 2020, doi: 10.3390/mi11030322.

[49] H. G. Kye *et al.*, “Dual-neodymium magnet-based microfluidic separation device,” *Sci Rep*, vol. 9, no. 1, Dec. 2019, doi: 10.1038/s41598-019-45929-y.

[50] A. Munaz, M. J. A. Shiddiky, and N. T. Nguyen, “Recent advances and current challenges in magnetophoresis based micro magnetofluidics,” *Biomicrofluidics*, vol. 12, no. 3, May 2018, doi: 10.1063/1.5035388.

[51] J. Chung, D. Issadore, A. Ullal, K. Lee, R. Weissleder, and H. Lee, “Rare cell isolation and profiling on a hybrid magnetic/size-sorting chip,” *Biomicrofluidics*, vol. 7, no. 5, Sep. 2013, doi: 10.1063/1.4821923.

[52] J. Chung, D. Issadore, A. Ullal, K. Lee, R. Weissleder, and H. Lee, “Rare cell isolation and profiling on a hybrid magnetic/size-sorting chip,” *Biomicrofluidics*, vol. 7, no. 5, Sep. 2013, doi: 10.1063/1.4821923.

[53] M. M. Hoque and M. M. Alam, “Effects of Dean Number and curvature on fluid flow through a curved pipe with magnetic field,” in *Procedia Engineering*, Elsevier Ltd, 2013, pp. 245–253. doi: 10.1016/j.proeng.2013.03.114.

[54] J. Grant, A. Özkan, C. Oh, G. Mahajan, R. Prantil-Baun, and D. E. Ingber, “Simulating drug concentrations in PDMS microfluidic organ chips,” *Lab Chip*, vol. 21, no. 18, pp. 3509–3519, Sep. 2021, doi: 10.1039/d1lc00348h.

[55] T. C. Cameron *et al.*, “PDMS Organ-On-Chip Design and Fabrication: Strategies for Improving Fluidic Integration and Chip Robustness of Rapidly Prototyped Microfluidic In Vitro Models,” *Micromachines (Basel)*, vol. 13, no. 10, Oct. 2022, doi: 10.3390/mi13101573.

[56] D. Ahn, L. M. Stevens, K. Zhou, and Z. A. Page, “Rapid High-Resolution Visible Light 3D Printing,” *ACS Cent Sci*, vol. 6, no. 9, pp. 1555–1563, Sep. 2020, doi: 10.1021/acscentsci.0c00929.

[57] J. Huang, B. Zhang, J. Xiao, and Q. Zhang, “An Approach to Improve the Resolution of DLP 3D Printing by Parallel Mechanism,” *Applied Sciences (Switzerland)*, vol. 12, no. 24, Dec. 2022, doi: 10.3390/app122412905.

[58] J. Zhang, Q. Hu, S. Wang, J. Tao, and M. Gou, “Digital light processing based three-dimensional printing for medical applications,” *Int J Bioprint*, vol. 6, no. 1, pp. 12–27, 2020, doi: 10.18063/ijb.v6i1.242.

[59] A. Gökaltun, Y. B. (Abraham) Kang, M. L. Yarmush, O. B. Usta, and A. Asatekin, “Simple Surface Modification of Poly(dimethylsiloxane) via Surface Segregating Smart Polymers for Biomicrofluidics,” *Sci Rep*, vol. 9, no. 1, Dec. 2019, doi: 10.1038/s41598-019-43625-5.

[60] Y. J. Chuah, Y. T. Koh, K. Lim, N. V. Menon, Y. Wu, and Y. Kang, “Simple surface engineering of polydimethylsiloxane with polydopamine for stabilized mesenchymal stem cell adhesion and multipotency,” *Sci Rep*, vol. 5, Dec. 2015, doi: 10.1038/srep18162.

[61] P. B. Luppa, “Point-of-care testing at the interface of emerging technologies and new clinical applications,” *Journal of Laboratory Medicine*, vol. 44, no. 2. Walter de Gruyter GmbH, pp. 59–61, Apr. 01, 2020. doi: 10.1515/labmed-2020-0020.

[62] E. Valera *et al.*, “COVID-19 Point-of-Care Diagnostics: Present and Future,” *ACS Nano*, vol. 15, no. 5. American Chemical Society, pp. 7899–7906, May 25, 2021. doi: 10.1021/acsnano.1c02981.

[63] S. J. Kim *et al.*, “Evaluation of the biocompatibility of a coating material for an implantable bladder volume sensor,” *Kaohsiung Journal of Medical Sciences*, vol. 28, no. 3, pp. 123–129, Mar. 2012, doi: 10.1016/j.kjms.2011.10.016.

[64] Y. Gou, Y. Jia, P. Wang, and C. Sun, “Progress of inertial microfluidics in principle and application,” *Sensors (Switzerland)*, vol. 18, no. 6. MDPI AG, Jun. 01, 2018. doi: 10.3390/s18061762.

[65] J. Feng, J. Neuzil, A. Manz, C. Iliescu, and P. Neuzil, “Microfluidic trends in drug screening and drug delivery,” *TrAC - Trends in Analytical Chemistry*, vol. 158. Elsevier B.V., Jan. 01, 2023. doi: 10.1016/j.trac.2022.116821.

[66] M. I. Khot *et al.*, “Characterising a PDMS based 3D cell culturing microfluidic platform for screening chemotherapeutic drug cytotoxic activity,” *Sci Rep*, vol. 10, no. 1, Dec. 2020, doi: 10.1038/s41598-020-72952-1.

[67] S. J. Streichan, C. R. Hoerner, T. Schneidt, D. Holzer, and L. Hufnagel, “Spatial constraints control cell proliferation in tissues,” *Proc Natl Acad Sci U S A*, vol. 111, no. 15, pp. 5586–5591, Apr. 2014, doi: 10.1073/pnas.1323016111.

[68] E. Amstad, “Capsules: Their past and opportunities for their future,” *ACS Macro Lett*, vol. 6, no. 8, pp. 841–847, Aug. 2017, doi: 10.1021/acsmacrolett.7b00472.

[69] A. Le Goff, B. Kaoui, G. Kurzawa, B. Haszon, and A. V. Salsac, “Squeezing bio-capsules into a constriction: Deformation till break-up,” *Soft Matter*, vol. 13, no. 41, pp. 7644–7648, 2017, doi: 10.1039/c7sm01417a.

[70] Z. Y. Luo and B. F. Bai, “Off-center motion of a trapped elastic capsule in a microfluidic channel with a narrow constriction,” *Soft Matter*, vol. 13, no. 44, pp. 8281–8292, 2017, doi: 10.1039/c7sm01425b.

[71] S. S. Deville and N. Cordes, “The Extracellular, Cellular, and Nuclear Stiffness, a Trinity in the Cancer Resistome—A Review,” *Frontiers in Oncology*, vol. 9. Frontiers Media S.A., Dec. 06, 2019. doi: 10.3389/fonc.2019.01376.

[72] G. Wang, K. Crawford, C. Turbyfield, W. Lam, A. Alexeev, and T. Sulchek, "Microfluidic cellular enrichment and separation through differences in viscoelastic deformation," *Lab Chip*, vol. 15, no. 2, pp. 532–540, Jan. 2015, doi: 10.1039/c4lc01150c.

[73] K. G. Phillips *et al.*, "Optical quantification of cellular mass, volume, and density of circulating tumor cells identified in an ovarian cancer patient," *Front Oncol*, vol. 2 JUL, 2012, doi: 10.3389/fonc.2012.00072.

[74] K. J. Regehr *et al.*, "Biological implications of polydimethylsiloxane-based microfluidic cell culture," *Lab on a Chip*, vol. 9, no. 15. Royal Society of Chemistry, pp. 2132–2139, 2009. doi: 10.1039/b903043c.

[75] S. Chow, D. Hedley, P. Grom, R. Magari, J. W. Jacobberger, and T. V. Shankey, "Whole blood fixation and permeabilization protocol with red blood cell lysis for flow cytometry of intracellular phosphorylated epitopes in leukocyte subpopulations," *Cytometry Part A*, vol. 67, no. 1, pp. 4–17, Sep. 2005, doi: 10.1002/cyto.a.20167.

[76] A. Reece, B. Xia, Z. Jiang, B. Noren, R. McBride, and J. Oakey, "Microfluidic techniques for high throughput single cell analysis," *Current Opinion in Biotechnology*, vol. 40. Elsevier Ltd, pp. 90–96, Aug. 01, 2016. doi: 10.1016/j.copbio.2016.02.015.

[77] S. Nagrath *et al.*, "Isolation of rare circulating tumour cells in cancer patients by microchip technology," *Nature*, vol. 450, no. 7173, pp. 1235–1239, Dec. 2007, doi: 10.1038/nature06385.

[78] S. Wang, Y. Zhou, X. Qin, S. Nair, X. Huang, and Y. Liu, “Label-free detection of rare circulating tumor cells by image analysis and machine learning,” *Sci Rep*, vol. 10, no. 1, Dec. 2020, doi: 10.1038/s41598-020-69056-1.

[79] A. A. S. Bhagat, H. W. Hou, L. D. Li, C. T. Lim, and J. Han, “Pinched flow coupled shear-modulated inertial microfluidics for high-throughput rare blood cell separation,” *Lab Chip*, vol. 11, no. 11, pp. 1870–1878, Jun. 2011, doi: 10.1039/c0lc00633e.

[80] D. R. Gossett *et al.*, “Label-free cell separation and sorting in microfluidic systems,” *Analytical and Bioanalytical Chemistry*, vol. 397, no. 8. pp. 3249–3267, Aug. 2010. doi: 10.1007/s00216-010-3721-9.

[81] A. F. Sarioglu *et al.*, “A microfluidic device for label-free, physical capture of circulating tumor cell clusters,” *Nat Methods*, vol. 12, no. 7, pp. 685–691, Jun. 2015, doi: 10.1038/nmeth.3404.

[82] J. Zhou, P. V. Giridhar, S. Kasper, and I. Papautsky, “Modulation of rotation-induced lift force for cell filtration in a low aspect ratio microchannel,” *Biomicrofluidics*, vol. 8, no. 4, Jul. 2014, doi: 10.1063/1.4891599.

[83] J. Zhou, P. V. Giridhar, S. Kasper, and I. Papautsky, “Modulation of rotation-induced lift force for cell filtration in a low aspect ratio microchannel,” *Biomicrofluidics*, vol. 8, no. 4, Jul. 2014, doi: 10.1063/1.4891599.

[84] M. Yamada, M. Nakashima, and M. Seki, “Pinched flow fractionation: Continuous size separation of particles utilizing a laminar flow profile in a pinched microchannel,” *Anal Chem*, vol. 76, no. 18, pp. 5465–5471, Sep. 2004, doi: 10.1021/ac049863r.

[85] S. Choi, S. Song, C. Choi, and J. K. Park, “Hydrophoretic sorting of micrometer and submicrometer particles using anisotropic microfluidic obstacles,” *Anal Chem*, vol. 81, no. 1, pp. 50–55, Jan. 2009, doi: 10.1021/ac801720x.

[86] S. Yan *et al.*, “On-chip high-throughput manipulation of particles in a dielectrophoresis- active hydrophoretic focuser,” *Sci Rep*, vol. 4, May 2014, doi: 10.1038/srep05060.

[87] H. A. Nieuwstadt, R. Seda, D. S. Li, J. B. Fowlkes, and J. L. Bull, “Microfluidic particle sorting utilizing inertial lift force,” *Biomed Microdevices*, vol. 13, no. 1, pp. 97–105, Feb. 2011, doi: 10.1007/s10544-010-9474-6.

[88] N. Nivedita, P. Ligrani, and I. Papautsky, “Dean Flow Dynamics in Low-Aspect Ratio Spiral Microchannels,” *Sci Rep*, vol. 7, Mar. 2017, doi: 10.1038/srep44072.

[89] E. Dressaire and A. Sauret, “Clogging of microfluidic systems,” *Soft Matter*, vol. 13, no. 1. Royal Society of Chemistry, pp. 37–48, 2017. doi: 10.1039/C6SM01879C.

[90] D. Venugopal, N. Kasani, Y. Manjunath, G. Li, J. T. Kaifi, and J. W. Kwon, “Clog-free high-throughput microfluidic cell isolation with multifunctional microposts,” *Sci Rep*, vol. 11, no. 1, Dec. 2021, doi: 10.1038/s41598-021-94123-6.

[91] J. Y. Park, S. J. Yoo, E. J. Lee, D. H. Lee, J. Y. Kim, and S. H. Lee, “Increased poly(dimethylsiloxane) stiffness improves viability and morphology of mouse fibroblast cells,” *Biochip J*, vol. 4, no. 3, pp. 230–236, 2010, doi: 10.1007/s13206-010-4311-9.

[92] B. Nath, A. Raza, V. Sethi, A. Dalal, S. S. Ghosh, and G. Biswas, “Understanding flow dynamics, viability and metastatic potency of cervical cancer (HeLa) cells

through constricted microchannel," *Sci Rep*, vol. 8, no. 1, Dec. 2018, doi: 10.1038/s41598-018-35646-3.

[93] A. Krishnan Thota Radhakrishnan, C. Poelma, J. van Lier, and F. Clemens, "Laminar-turbulent transition of a non-Newtonian fluid flow," *Journal of Hydraulic Research*, vol. 59, no. 2, pp. 235–249, 2021, doi: 10.1080/00221686.2020.1770876.

[94] A. Krishnan Thota Radhakrishnan, C. Poelma, J. van Lier, and F. Clemens, "Laminar-turbulent transition of a non-Newtonian fluid flow," *Journal of Hydraulic Research*, vol. 59, no. 2, pp. 235–249, 2021, doi: 10.1080/00221686.2020.1770876.

[95] O. S. Ismail and G. T. Adewoye, "Analyses and Modeling of Laminar Flow in Pipes Using Numerical Approach," *Journal of Software Engineering and Applications*, vol. 05, no. 09, pp. 653–658, 2012, doi: 10.4236/jsea.2012.59076.

[96] A. Drózdz and W. Elsner, "Study of Reynolds number effect on turbulent boundary layer near the separation," in *Journal of Physics: Conference Series*, Institute of Physics Publishing, Nov. 2016. doi: 10.1088/1742-6596/760/1/012003.

[97] K. Cielicki and A. Piechna, "Can the dean number alone characterize flow similarity in differently bent tubes?," *Journal of Fluids Engineering, Transactions of the ASME*, vol. 134, no. 5, 2012, doi: 10.1115/1.4006417.

[98] I. D. Johnston, M. B. McDonnell, C. K. L. Tan, D. K. McCluskey, M. J. Davies, and M. C. Tracey, "Dean flow focusing and separation of small microspheres within a narrow size range," *Microfluid Nanofluidics*, vol. 17, no. 3, pp. 509–518, 2014, doi: 10.1007/s10404-013-1322-6.

[99] F. Schönfeld and S. Hardt, “Simulation of Helical Flows in Microchannels,” *AIChE Journal*, vol. 50, no. 4, pp. 771–778, Apr. 2004, doi: 10.1002/aic.10071.

[100] “Flow control in microfluidic devices.” [Online]. Available: www.elveflow.com

[101] J. Winslow, H. Otsuka, B. Govindarajan, and I. Chopra, “Basic understanding of airfoil characteristics at low Reynolds numbers (104–105),” *J Aircr*, vol. 55, no. 3, pp. 1050–1061, 2018, doi: 10.2514/1.C034415.

[102] P. Friedl, K. S. Zänker, and E. B. Bröcker, “Cell migration strategies in 3-D extracellular matrix: Differences in morphology, cell matrix interactions, and integrin function,” *Microscopy Research and Technique*, vol. 43, no. 5. pp. 369–378, Dec. 01, 1998. doi: 10.1002/(SICI)1097-0029(19981201)43:5<369::AID-JEMT3>3.0.CO;2-6.

[103] M. A. Heinrich, R. Alert, J. M. Lachance, T. J. Zajdel, A. K. Mrlj, and D. J. Cohen, “Size-dependent patterns of cell proliferation and migration in freely-expanding epithelia,” *Elife*, vol. 9, pp. 1–21, Aug. 2020, doi: 10.7554/ELIFE.58945.

[104] C. Gérard and A. Goldbeter, “The balance between cell cycle arrest and cell proliferation: Control by the extracellular matrix and by contact inhibition,” *Interface Focus*, vol. 4, no. 3, 2014, doi: 10.1098/rsfs.2013.0075.

[105] C. Gérard and A. Goldbeter, “The balance between cell cycle arrest and cell proliferation: Control by the extracellular matrix and by contact inhibition,” *Interface Focus*, vol. 4, no. 3, 2014, doi: 10.1098/rsfs.2013.0075.

[106] “Chapter 12 - Cell Growth first-page-pdf”.

[107] J. J. Tyson and B. Novak, “Control of cell growth, division and death: Information processing in living cells,” *Interface Focus*, vol. 4, no. 3. Royal Society, 2014. doi: 10.1098/rsfs.2013.0070.

[108] J. Sun, A. R. Warden, and X. Ding, “Recent advances in microfluidics for drug screening,” *Biomicrofluidics*, vol. 13, no. 6. American Institute of Physics Inc., Nov. 01, 2019. doi: 10.1063/1.5121200.

[109] “RETRIEVAL OF ARTIFICIAL BLOOD CELLS (PERFLUOROCHEMICAL) FROM WHOLE BLOOD RETRIEVAL_OF_ARTIFICIAL_BLOOD_CELLS.89”.

[110] H. W. Hou *et al.*, “Isolation and retrieval of circulating tumor cells using centrifugal forces,” *Sci Rep*, vol. 3, 2013, doi: 10.1038/srep01259.

[111] P. Paterlini-Brechot and N. L. Benali, “Circulating tumor cells (CTC) detection: Clinical impact and future directions,” *Cancer Letters*, vol. 253, no. 2. Elsevier Ireland Ltd, pp. 180–204, Aug. 18, 2007. doi: 10.1016/j.canlet.2006.12.014.

[112] M. C. Miller, G. V. Doyle, and L. W. M. M. Terstappen, “Significance of Circulating Tumor Cells Detected by the CellSearch System in Patients with Metastatic Breast Colorectal and Prostate Cancer,” *J Oncol*, vol. 2010, pp. 1–8, 2010, doi: 10.1155/2010/617421.

[113] Z. Shen, A. Wu, and X. Chen, “Current detection technologies for circulating tumor cells,” *Chemical Society Reviews*, vol. 46, no. 8. Royal Society of Chemistry, pp. 2038–2056, Apr. 21, 2017. doi: 10.1039/c6cs00803h.

[114] S. Ju *et al.*, “Detection of circulating tumor cells: opportunities and challenges,” *Biomarker Research*, vol. 10, no. 1. BioMed Central Ltd, Dec. 01, 2022. doi: 10.1186/s40364-022-00403-2.

[115] C. V. Pecot *et al.*, “A novel platform for detection of CK + and CK - CTCs,” *Cancer Discov*, vol. 1, no. 7, pp. 580–586, Dec. 2011, doi: 10.1158/2159-8290.CD-11-0215.

[116] N. Norouzi, H. C. Bhakta, and W. H. Grover, “Sorting cells by their density,” *PLoS One*, vol. 12, no. 7, Jul. 2017, doi: 10.1371/journal.pone.0180520.

[117] “Patent uspto 16830617 microfluidic device patent tumortrap ”.

[118] Y. Y. Yan *et al.*, “Cell-Free DNA: Hope and Potential Application in Cancer,” *Frontiers in Cell and Developmental Biology*, vol. 9. Frontiers Media S.A., Feb. 22, 2021. doi: 10.3389/fcell.2021.639233.

[119] Q. Gao *et al.*, “Circulating cell-free DNA for cancer early detection,” *Innovation*, vol. 3, no. 4. Cell Press, Jul. 12, 2022. doi: 10.1016/j.xinn.2022.100259.

[120] M. Cisneros-Villanueva *et al.*, “Cell-free DNA analysis in current cancer clinical trials: a review,” *British Journal of Cancer*. Springer Nature, 2022. doi: 10.1038/s41416-021-01696-0.

[121] J. Dai *et al.*, “Exosomes: key players in cancer and potential therapeutic strategy,” *Signal Transduction and Targeted Therapy*, vol. 5, no. 1. Springer Nature, Dec. 01, 2020. doi: 10.1038/s41392-020-00261-0.

[122] Y. L. Tai, K. C. Chen, J. T. Hsieh, and T. L. Shen, “Exosomes in cancer development and clinical applications,” *Cancer Science*, vol. 109, no. 8. Blackwell Publishing Ltd, pp. 2364–2374, Aug. 01, 2018. doi: 10.1111/cas.13697.

[123] M. D. A. Paskeh *et al.*, “Emerging role of exosomes in cancer progression and tumor microenvironment remodeling,” *Journal of Hematology and Oncology*, vol. 15, no. 1. BioMed Central Ltd, Dec. 01, 2022. doi: 10.1186/s13045-022-01305-4.

[124] X. Zhang *et al.*, “The Biology and Function of Extracellular Vesicles in Cancer Development,” *Frontiers in Cell and Developmental Biology*, vol. 9. Frontiers Media S.A., Nov. 05, 2021. doi: 10.3389/fcell.2021.777441.

[125] N. Tominaga, “Anti-cancer role and therapeutic potential of extracellular vesicles,” *Cancers*, vol. 13, no. 24. MDPI, Dec. 01, 2021. doi: 10.3390/cancers13246303.

[126] S. Lucotti, C. M. Kenific, H. Zhang, and D. Lyden, “Extracellular vesicles and particles impact the systemic landscape of cancer,” *EMBO J*, vol. 41, no. 18, Sep. 2022, doi: 10.15252/embj.2021109288.

[127] R. Xu, A. Rai, M. Chen, W. Suwakulsiri, D. W. Greening, and R. J. Simpson, “Extracellular vesicles in cancer — implications for future improvements in cancer care,” *Nature Reviews Clinical Oncology*, vol. 15, no. 10. Nature Publishing Group, pp. 617–638, Oct. 01, 2018. doi: 10.1038/s41571-018-0036-9.

[128] K. Qian, W. Fu, T. Li, J. Zhao, C. Lei, and S. Hu, “The roles of small extracellular vesicles in cancer and immune regulation and translational potential in cancer therapy,” *Journal of Experimental and Clinical Cancer Research*, vol. 41, no. 1. BioMed Central Ltd, Dec. 01, 2022. doi: 10.1186/s13046-022-02492-1.

[129] “Assessment of Nucleic Acid Purity.” [Online]. Available: www.nanodrop.com

[130] W. Zhang, D. S. Choi, Y. H. Nguyen, J. Chang, and L. Qin, “Studying cancer stem cell dynamics on PDMS surfaces for microfluidics device design,” *Sci Rep*, vol. 3, 2013, doi: 10.1038/srep02332.

[131] M. A. Giese, L. E. Hind, and A. Huttenlocher, “Neutrophil plasticity in the tumor microenvironment,” 2019. [Online]. Available: https://ashpublications.org/blood/article-pdf/133/20/2159/1557207/blood844548.pdf

[132] D. Zink, A. H. Fischer, and J. A. Nickerson, “Nuclear structure in cancer cells,” *Nature Reviews Cancer*, vol. 4, no. 9. pp. 677–687, Sep. 2004. doi: 10.1038/nrc1430.

[133] S. Riethdorf *et al.*, “Detection of circulating tumor cells in peripheral blood of patients with metastatic breast cancer: A validation study of the cell search system,” *Clinical Cancer Research*, vol. 13, no. 3, pp. 920–928, Feb. 2007, doi: 10.1158/1078-0432.CCR-06-1695.

[134] Z. Miao, P. Moreno, N. Huang, I. Papatheodorou, A. Brazma, and S. A. Teichmann, “Putative cell type discovery from single-cell gene expression data,” *Nat Methods*, vol. 17, no. 6, pp. 621–628, Jun. 2020, doi: 10.1038/s41592-020-0825-9.

[135] C. L. Chen *et al.*, “Single-cell analysis of circulating tumor cells identifies cumulative expression patterns of EMT-related genes in metastatic prostate cancer,” *Prostate*, vol. 73, no. 8, pp. 813–826, Jun. 2013, doi: 10.1002/pros.22625.

[136] S. Il Seok and T. F. Guo, “Halide perovskite materials and devices,” *MRS Bull*, vol. 45, no. 6, pp. 427–430, Jun. 2020, doi: 10.1557/mrs.2020.140.

[137] Y. Dong, Y. Zou, J. Song, X. Song, and H. Zeng, “Recent progress of metal halide perovskite photodetectors,” *Journal of Materials Chemistry C*, vol. 5, no. 44. Royal Society of Chemistry, pp. 11369–11394, 2017. doi: 10.1039/c7tc03612d.

[138] H. Dong, C. Ran, W. Gao, M. Li, Y. Xia, and W. Huang, “Metal Halide Perovskite for next-generation optoelectronics: progresses and prospects,” *eLight*, vol. 3, no. 1, Jan. 2023, doi: 10.1186/s43593-022-00033-z.

[139] C. H. Liao, M. A. Mahmud, and A. W. Y. Ho-Baillie, “Recent progress in layered metal halide perovskites for solar cells, photodetectors, and field-effect transistors,” *Nanoscale*, vol. 15, no. 9. Royal Society of Chemistry, pp. 4219–4235, Feb. 06, 2023. doi: 10.1039/d2nr06496k.

[140] S. Vijaya, J. Subbiah, D. J. Jones, and S. Anandan, “LARP-assisted synthesis of $CsBi_3I_{10}$ perovskite for efficient lead-free solar cells,” *RSC Adv*, vol. 13, no. 15, pp. 9978–9982, 2023, doi: 10.1039/D3RA00365E.

[141] T. H. Han *et al.*, “Perovskite-polymer composite cross-linker approach for highly-stable and efficient perovskite solar cells,” *Nat Commun*, vol. 10, no. 1, Dec. 2019, doi: 10.1038/s41467-019-08455-z.

[142] T. Yokoyama *et al.*, “Overcoming Short-Circuit in Lead-Free CH3NH3SnI3 Perovskite Solar Cells via Kinetically Controlled Gas-Solid Reaction Film Fabrication Process,” *Journal of Physical Chemistry Letters*, vol. 7, no. 5, pp. 776–782, Mar. 2016, doi: 10.1021/acs.jpclett.6b00118.

[143] Y. Wang, M. L. Gao, J. L. Wu, and X. W. Zhang, “Metal halide perovskite photodetectors: Material features and device engineering,” *Chinese Physics B*, vol. 28, no. 1. Institute of Physics Publishing, 2019. doi: 10.1088/1674-1056/28/1/018502.

[144] I. Poli, G. W. Kim, E. L. Wong, A. Treglia, G. Folpini, and A. Petrozza, “High External Photoluminescence Quantum Yield in Tin Halide Perovskite Thin Films,”

ACS Energy Lett, vol. 6, no. 2, pp. 609–611, Feb. 2021, doi: 10.1021/acsenergylett.0c02612.

[145] S. Jung *et al.*, "Enhancement of Photoluminescence Quantum Yield and Stability in CsPbBr3 Perovskite Quantum Dots by Trivalent Doping," *Nanomaterials*, vol. 10, no. 4, Apr. 2020, doi: 10.3390/nano10040710.

[146] M. G. La-Placa, G. Longo, A. Babaei, L. Martínez-Sarti, M. Sessolo, and H. J. Bolink, "Photoluminescence quantum yield exceeding 80% in low dimensional perovskite thin-films: Via passivation control," *Chemical Communications*, vol. 53, no. 62, pp. 8707–8710, 2017, doi: 10.1039/c7cc04149g.

[147] M. Kafetzi, S. Pispas, and G. Mousdis, "Hybrid perovskite/polymer materials: Preparation and physicochemical properties," *Journal of Composites Science*, vol. 5, no. 11, Nov. 2021, doi: 10.3390/jcs5110304.

[148] C.-F. Lai, C.-C. Chang, M.-J. Wang, and M.-K. Wu, "CCT- and CRI-tuning of white light-emitting diodes using three-dimensional non-close-packed colloidal photonic crystals with photonic stop-bands," *Opt Express*, vol. 21, no. S4, p. A687, Jul. 2013, doi: 10.1364/oe.21.00a687.

[149] S. Vijaya, J. Subbiah, D. J. Jones, and S. Anandan, "LARP-assisted synthesis of $CsBi_3I_{10}$ perovskite for efficient lead-free solar cells," *RSC Adv*, vol. 13, no. 15, pp. 9978–9982, 2023, doi: 10.1039/D3RA00365E.

[150] G. C. Adhikari, P. A. Vargas, H. Zhu, and P. Zhu, "Saponification Precipitation Method for CsPbBr 3 Nanocrystals with Blue-Green Tunable Emission," *Journal of Physical Chemistry C*, vol. 123, no. 2, pp. 1406–1412, Jan. 2019, doi: 10.1021/acs.jpcc.8b10636.

[151] S. Thapa, G. C. Adhikari, H. Zhu, and P. Zhu, “Blue-red color-tunable all-inorganic bromide–iodide mixed-halide perovskite nanocrystals using the saponification technique for white-light-emitting diodes,” *Journal of the Optical Society of America B*, vol. 36, no. 6, p. 1616, Jun. 2019, doi: 10.1364/josab.36.001616.

[152] D. Liu *et al.*, “Direct optical patterning of perovskite nanocrystals with ligand cross-linkers,” 2022. [Online]. Available: https://www.science.org

[153] D. Liu *et al.*, “Direct optical patterning of perovskite nanocrystals with ligand cross-linkers,” 2022. [Online]. Available: https://www.science.org

[154] A. H. Proppe, M. Wei, B. Chen, R. Quintero-Bermudez, S. O. Kelley, and E. H. Sargent, “Photochemically Cross-Linked Quantum Well Ligands for 2D/3D Perovskite Photovoltaics with Improved Photovoltage and Stability,” *J Am Chem Soc*, vol. 141, no. 36, pp. 14180–14189, Sep. 2019, doi: 10.1021/jacs.9b05083.

[155] H. Xiao *et al.*, “Polymer ligands induced remarkable spectral shifts in all-inorganic lead halide perovskite nanocrystals,” *J Mater Chem C Mater*, vol. 8, no. 29, pp. 9968–9974, Aug. 2020, doi: 10.1039/d0tc01822h.

[156] W. Peng and B. Riedl, “Thermosetting Resins,” UTC, 1995. [Online]. Available: https://pubs.acs.org/sharingguidelines

[157] D. Ahn, L. M. Stevens, K. Zhou, and Z. A. Page, “Rapid High-Resolution Visible Light 3D Printing,” *ACS Cent Sci*, vol. 6, no. 9, pp. 1555–1563, Sep. 2020, doi: 10.1021/acscentsci.0c00929.

[158] H. Quan, T. Zhang, H. Xu, S. Luo, J. Nie, and X. Zhu, “Photo-curing 3D printing technique and its challenges,” *Bioactive Materials*, vol. 5, no. 1. KeAi

Communications Co., pp. 110–115, Mar. 01, 2020. doi: 10.1016/j.bioactmat.2019.12.003.

[159] J. Jargus, J. Vitasek, J. Nedoma, V. Vasinek, and R. Martinek, “Effect of selected luminescent layers on CCT, CRI, and response times,” *Materials*, vol. 12, no. 13, Jul. 2019, doi: 10.3390/ma12132095.

[160] Y. Ohno, “Calculation of CCT and Duv and Practical Conversion Formulae.”

[161] T. S. Kao, Y. H. Hong, K. Bin Hong, and T. C. Lu, “Perovskite random lasers: A tunable coherent light source for emerging applications,” *Nanotechnology*, vol. 32, no. 28. IOP Publishing Ltd, Jul. 09, 2021. doi: 10.1088/1361-6528/abe907.

[162] J. Yao, L. Xu, S. Wang, and J. Song, “Metal halide perovskites-based white light-emitting diodes,” *JPhys Photonics*, vol. 4, no. 4. Institute of Physics, Oct. 01, 2022. doi: 10.1088/2515-7647/ac91b7.

[163] W. Sun *et al.*, “Lead halide perovskite vortex microlasers,” *Nat Commun*, vol. 11, no. 1, Dec. 2020, doi: 10.1038/s41467-020-18669-1.

[164] D. A. Barcelos, D. C. Leitao, L. C. J. Pereira, and M. C. Gonçalves, “What is driving the growth of inorganic glass in smart materials and opto-electronic devices?,” *Materials*, vol. 14, no. 11. MDPI AG, Jun. 01, 2021. doi: 10.3390/ma14112926.

VITA

Dilip Venugopal was born and raised in Bangalore, India. Before attending University of Missouri Columbia, he attended Bangalore Institute of Technology, India, where he earned his Bachelor of Engineering degree with First Class with Distinction in 2014. He also received his Master of Science from the University of Missouri Columbia (Mizzou).

While at Mizzou, Dilip was awarded the TA Choice award for best Teaching Assistant of 2018-2019 in the Electrical Engineering Department.